A SEARCH FOR LARGE EXTRA SPATIAL DIMENSIONS AND Z' BOSONS IN THE DIMUON FINAL STATE IN $\sqrt{s} = 1.96$ TeV $p\overline{p}$ COLLISIONS AT DØ

A Dissertation

Submitted to the Graduate School

of the University of Notre Dame

in Partial Fulfillment of the Requirements

for the Degree of

Doctor of Philosophy

by

Ryan James Hooper, B.S., M.S.

Mitchell Wayne, Director

Graduate Program in Physics

Notre Dame, Indiana

April 2004

© Copyright by

RYAN J. HOOPER

2004

All rights reserved

A SEARCH FOR LARGE EXTRA SPATIAL DIMENSIONS AND Z' BOSONS IN THE DIMUON FINAL STATE IN $\sqrt{s} = 1.96$ TeV $p\overline{p}$ COLLISIONS AT DØ

Abstract

by

Ryan James Hooper

Searches for large extra spatial dimensions (LED) and extra neutral gauge bosons (Z') in the dimuon channel are presented. Both of these searches are performed on 170 ± 11 pb^{-1} of data collected at Fermilab's upgraded DØ detector which studies $p\overline{p}$ interactions at a center-of-mass energy of 1.96 TeV. Although no LED or Z' signals are seen, 95% confidence level limits are found in both cases. In the search for LED agreement between Standard Model backgrounds and data is shown in the dimuon mass versus $\cos(\theta^*)$ spectrums. For the LED analysis a lower 95% confidence level limit of $M_S > 1.0$ TeV (GRW) is obtained. In the search for Z' the measured high p_T dimuon mass distribution agrees with the the predictions from the Standard Model. This Z' analysis finds and sets a lower 95% confidence level mass limit of $M_{Z'} >$ 690 GeV (SSM).

To my beloved wife Stephanie and my parents Larry and Margo for their tireless support and encouragement.

'Knowledge is power', but to a degree only. It's possession per se will raise a man to mediocrity, but not to distinction.

G. S. Patton, Jr., Major

The Secret of Victory

March 26, 1926

CONTENTS

FIGURES vii

TABLES xii

ACKNOWLEDGMENTS xiv

CHAPTER 1: INTRODUCTION 1
1.1 The Standard Model 1
1.2 Motivation for This Research 5
1.3 Thesis Overview 6

CHAPTER 2: THEORIES AND PHENOMENOLOGY 7
2.1 Motivation for New Physics 7
2.2 Extra Neutral Gauge Bosons 8
2.2.1 Grand Unified Theory 9
2.2.2 Left-Right Symmetric Model 10
2.2.3 Superstring Theory 10
2.2.4 Sequential Standard Model 11
2.2.5 Previous Z' Searches 12
2.3 Large Extra Dimensions 13
2.4 Phenomenology of Large Extra Spatial Dimensions at the Tevatron . 15
2.5 Dilepton Production at the Tevatron 16

CHAPTER 3: THE EXPERIMENTAL APPARATUS 19
3.1 Luminosities and Cross Sections 19
3.2 The Fermilab Accelerator 20
3.2.1 The Preaccelerator 20
3.2.2 The Linac 22
3.2.3 The Booster Synchrotron 23
3.2.4 Main Injector 23
3.2.5 The Anti-proton Source 24
3.2.6 The Debuncher and Accumulator 25
3.2.7 The Tevatron 26

3.3 Coordinate Systems and Other Conventions at DØ 26
3.4 The Run II DØ Detector 29
3.4.1 Tracking System 31
3.4.2 The Silicon Microstrip Tracker 32
3.4.3 The Central Fiber Tracker 34
3.4.4 The Central and Forward Preshower Detectors 38
3.4.5 The Calorimeter 40
3.4.6 Intercryostat and Massless Gap Detectors 45
3.4.7 The Muon System 46
3.4.8 Trigger and Data Acquisition Systems 51

CHAPTER 4: THE LARGE EXTRA SPATIAL DIMENSIONS ANALYSIS . 57
4.1 Data Sets and Selections 57
4.1.1 Overview of Muon Identification 58
4.1.2 Collider Runs and Common Sample Skims 60
4.1.3 Bad Runs, Duplicate Events and Triggers 61
4.1.4 Selection Cuts 62
4.1.5 Final Data Sample 71
4.2 The Fast Monte Carlo 73
4.2.1 Acceptances 75
4.2.2 Momentum Smearing 78
4.2.3 Dimuon p_T 80
4.2.4 K-Factor 85
4.3 Other Backgrounds 87
4.4 Data and Simulation Comparisons 88
4.4.1 Normalizing MC to Data: The Effective Luminosity 88
4.4.2 Data and Background Comparisons 89
4.4.3 Comparisons in the Presence of a LED Signal 91
4.5 Extracting the Parameter η_G from Data 96
4.5.1 Finding the Best η_G from Data 96
4.5.2 Overview of the Bayesian Technique Used and 95% Confidence Level Limits for η_G 97
4.5.3 Application in the LED analysis 98
4.5.4 Tests of Sensitivity 100
4.6 Results 101
4.6.1 From η_G to M_S 101

CHAPTER 5: THE Z' ANALYSIS 107
5.1 Data Sets and Selections 107
5.2 Backgrounds 108
5.2.1 Background Uncertainties 108
5.3 Monte Carlo 110
5.4 Optimum Cut Window 112
5.5 Acceptance 114
5.5.1 Systematic Errors on the Acceptance 115
5.6 Results and Limits 115
5.6.1 Z' Mass Limit 119

CHAPTER 6: CONCLUSIONS 123

APPENDIX A: INTERESTING CANDIDATE EVENTS 124

BIBLIOGRAPHY 128

FIGURES

2.1 Feynman diagrams for dilepton production in the presence of large extra dimensions. In this figure G_n^* represents the graviton. Reproduced from Gupta *et al.* [13]. 16

3.1 Schematic of the Run II Fermilab accelerator complex. Adapted from [18]. 21

3.2 Illustration of the Linac. Adapted from [17]. 22

3.3 Illustration of $\overline{p}$ production. Adapted from [19]. 25

3.4 View of the DØ coordinates and p_T. 28

3.5 Distribution of the interaction point's z-axis position. 29

3.6 An $r - z$ view of the Run II DØ detector. Adapted from [18]. 30

3.7 View of the DØ tracking system. Adapted from [23]. 31

3.8 Three dimensional view of the SMT. Adapted from [18]. 33

3.9 Drawing of a displaced vertex originating from a b or c quark decay. Adapted from [18]. 34

3.10 a) A quarter $r - z$ view of the CFT detector showing the nested eight barrel design. b) A magnified $r - \phi$ end view of the two ribbon doublet layer configuration for two different barrels. Adapted from [18]. . . . 35

3.11 a) The position resolution distribution measured in the CFT cosmic ray test stand. b) An end view of the interlocking doublet ribbon configuration used by the CFT. Adapted from [18]. 36

3.12 a) Shows a $r - z$ semi-quarter view of the CPS detector. b) A cross-sectional $r - \phi$ end view of the CFT and CPS detectors. The inset shows a magnified view of the nested triangular strips and layer configurations for the CPS. Adapted from [18]. 39

3.13 One quarter $r - z$ view of the FPS detector. The inset shows details of the $u - v$ scintillator layers. Adapted from [18]. 40

3.14 Three dimensional cut away view of the DØ calorimeter. Adapted from [18]. 42

3.15 A one quarter $r - z$ view of the calorimeter. Lines extending from the center of the detector shows the η coverage of cells and projected towers. Adapted from [18]. 44

3.16 Schematic view of a calorimeter cell. Adapted from [18]. 46

3.17 A $r - z$ half-view of the Muon System. Components of both the Forward and Wide Angle systems are shown. Adapted from [18]. . . 48

3.18 Seen here is a $r - \phi$ view of one plane of the muon mini-drift tube. The insert shows the cross section of a single Iarocci tube. Adapted from [18]. 50

3.19 An $r - \phi$ view of the segmentation of the FAMUS scintillator pixel counters is shown. Adapted from [18]. 51

3.20 The DØ trigger layout and typical trigger rates. Adapted from [18]. 53

3.21 Level 1 and Level 2 trigger data flow paths. Adapted from [18]. . . . 54

3.22 The L3 and DAQ system layout. Adapted from [3]. 55

4.1 The plot shows the run numbers used for this analysis. 61

4.2 The top two plots are of the SMT and CFT hit distributions for tracks from muons in the data set. The arrows indicate where the selection cuts are placed. The bottom plot shows the dimuon invariant mass distribution of those events cut by this selection. 64

4.3 The top plot is of the A and BC layer scintillation time distributions for this data set. The arrows indicate where the selection cut is placed. The bottom plot shows the dimuon invariant mass distribution of those events cut by this selection. 66

4.4 The plot is of the $\eta_1 + \eta_2$ distribution for out-of-time dimuon events. . 67

4.5 The top plot is of the muon's $\eta_1 + \eta_2$ distribution for the data set. The arrows indicate where the selection cuts are placed. The bottom plot shows the dimuon invariant mass distribution of those events cut by this selection. 68

4.6 The top plot is of the calorimeter halo distribution for the data set. The arrow indicates where the selection cut is placed. The bottom plot shows the dimuon invariant mass distribution of those events cut by this selection. 69

4.7 The top plot is of the track halo distribution for the data set. The arrow indicates where the selection cut is placed. The bottom plot shows the dimuon invariant mass distribution of those events cut by this selection. 70

4.8 The matched central track χ^2/dof (top), calorimeter halo isolation (middle) and track halo isolation (bottom) distributions as a function of muon p_T from full p14 Monte Carlo. 72

4.9 Invariant mass distribution for the final data set. Shown in both linear and semi-log scales. 74

4.10 Plots of $\Delta\phi$, $\Delta\eta$, and ΔR between reconstructed and generated muons from the full p14 Drell-Yan MC sample. The horizontal axis for these plots is zoomed in near zero to accentuate the peak there. 76

4.11 The two-dimensional acceptance plot used to create the acceptance map file. 77

4.12 Comparisons of the muon's η, ϕ using the original acceptance map, the corrected map, and data. The top plots are for the muon with the highest p_T and the bottom plots are for the other muon. 78

4.13 Plots of the comparisons between SM MC (histogram) and data (points) around the Z-peak for the different smearing parameters and scaling factors. Each MC distribution is area normalized to the data for this comparison. The top five plots show the mass comparisons for SF factors of 1.1 to 1.4 with $Scale = 1.0$. The bottom five plots show similar comparisons with the same ranges of SF, but with $Scale = 0.99$. 81

4.14 Plots of the comparisons between SM MC (histogram) and data (points) around the Z-peak for the different smearing parameters and scaling factors. Each MC distribution is area normalized to the data for this comparison. The top five plots show the mass comparisons for SF factors of 1.1 to 1.4 with $Scale = 0.985$. The bottom five plots show similar comparisons with the same ranges of SF, but with $Scale = 0.98$ 82

4.15 Summary of the Kolmogorov tests done to find the best smearing parameters around the Z-peak. The plot shows the Kolmogorov test results (KS) versus the different test runs. All the different runs are in this plot, but some results are too small to be seen in the figure. For instance Run 1 has a KS value of 1.5×10^{-15}. 83

4.16 A) Shows the definition of θ^* at the parton level. B) Shows the definition of θ^* in the presence of NLO effects. Here GJ refers to the Gottfied-Jackson frame which is equivalent to the helicity frame at LO, but not with NLO effects. In this figure ISR stands for initial state radiation. Adapted from [10]. 84

4.17 The SM dimuon p_T distributions based on the Run I parameterization, the new parameterizations, and for data. 86

4.18 Comparison of dimuon invariant mass distributions near the Z-peak for the data (points) and background (histogram). 89

4.19 Comparison of several kinematic variable distributions for the data (points) and background (histogram). The top plots are for the highest p_T muon, while the bottom plots are for the other muon in the event. 90

4.20 Comparison of the p_T distribution of the dimuon system for the data (points) and background (histogram). 91

4.21 Comparison between data (points) and background (histogram) for $|\cos(\theta^*)|$ and $M_{\mu\mu}$ distributions. 92

4.22 Comparison between data (points) and backgrounds (histogram) for $M_{\mu\mu}$ distributions. This plot also shows the contributions that would be expected at high $M_{\mu\mu}$ with the presence of large extra dimensions. 93

4.23 Distributions in $M_{\mu\mu}$ vs. $|\cos(\theta^*)|$ space for MC and Data. MC is scaled by the effective luminosity. The lower left plot shows SM plus contributions from the G_{KK} terms with η_G=3 TeV^{-4}. 94

4.24 Distributions in $M_{\mu\mu}$ vs. $|\cos(\theta^*)|$ space for MC and data. MC is scaled by the effective luminosity. The top left plot shows the data sample. While the rest of the plots show MC SM plus contributions from the G_{KK} terms with η_G=1 TeV^{-4}, 3 TeV^{-4} and 5 TeV^{-4}. 95

4.25 The distribution of 95% CL limits for 100 MC trials on η_G are shown here. The shaded histogram represents the Likelihood distribution, while the outlined histogram is the Bayesian distribution. Arrows with labels indicate Bayesian and Likelihood limits, found from the data. 102

4.26 The distribution of the best fit values on η_G for 100 MC trials are shown as well as the value found from the data. The plot on the right is the same as the plot on the left but the x-axis is zoomed in to better show the values near zero. An arrow with a label indicates the best fit value found from the data. 103

4.27 The distribution of 95% CL limits for 100 MC trials on η_G are shown here. These distributions are for background plus a LED signal of η_G=0.99 TeV^{-4}. The shaded histogram represents the Likelihood distribution, while the outlined histogram is the Bayesian distribution. The arrow with the label indicates the limit found from the data. 104

5.1 Invariant mass distribution for the final data set. Shown in both linear and semi-log scales. 109

5.2 Invariant mass distributions for different mass Z' decaying into two muons. 111

5.3 Fit to the falling Drell-Yan MC distribution. 113

5.4 Signal over square root background for a Gaussian signal on the falling background. The different traces show the $S/\sqrt{B}$ for different resonance masses. 114

5.5 Acceptance fits using a 2nd order polynomial. 116

5.6 This plot shows the Gaussian plus Landau with a exponential background fit to the data Z-peak. Parameter 2 in this plot is σ_Z, along with its error which is used in the acceptance section of this analysis. 117

5.7 Invariant mass distributions for data (points) and background (histogram). 119

5.8 The 95% CL limits on $\sigma \times BR(Z' \to \mu\mu)$. 121

A.1 The top figure shows the central tracking system XY view for our highest mass candidate. Reconstructed tracks are shown as well as muon system hits displayed as polygons. The bottom figure shows the $r - z$ view for our highest mass candidate. Reconstructed tracks are shown as well as muon system hits displayed as rectangles. 126

A.2 The top figure shows the central tracking system XY view for our highest mass with the lowest $\cos(\theta^*)$ event. Reconstructed tracks are shown as well as muon system hits displayed as polygons. The bottom figure shows the $r - z$ view for our highest mass with the lowest $\cos(\theta^*)$ candidate. Reconstructed tracks are shown as well as muon system hits displayed as rectangles. 127

TABLES

1.1 THE STANDARD MODEL FERMIONS 2

1.2 THE STANDARD MODEL GAUGE BOSONS 4

2.1 SUMMARY OF CURRENT Z' MASS LIMITS 13

3.1 DEPTH OF THE DIFFERENT CALORIMETER LAYERS 43

4.1 DEFINITIONS OF NSEG 58

4.2 MUON QUALITY DEFINITIONS 59

4.3 TRIGGER DESCRIPTIONS AT LEVEL 1 62

4.4 TRIGGER DESCRIPTIONS AT LEVEL 2 AND 3 63

4.5 EVENT SELECTION 73

4.6 COMPARISON OF DATA AND EXPECTED BACKGROUND . . . 92

4.7 UNCERTAINTY ON THE CALCULATED CROSS SECTION . . . 97

4.8 LIMITS FOUND FOR THE FUNDAMENTAL PLANCK SCALE M_S 105

4.9 LIMITS ON M_S FOR SEVERAL DIFFERENT EXPERIMENTS INCLUDING THE RESULT FROM THIS ANALYSIS 106

5.1 EVENT SELECTION 108

5.2 SUMMARY OF ACCEPTANCE, DATA, AND BACKGROUNDS IN THIS ANALYSIS 118

5.3 SUMMARY OF THE LIMIT SETTING INPUTS AND ERRORS . . 120

5.4 THEORETICAL AND MEASURED $\sigma \times BR(Z' \to \mu\mu)$ 120

5.5 SUMMARY OF CURRENT HADRON COLLIDER Z' MASS LIMITS AND THE LIMIT OBTAINED FROM THIS ANALYSIS 122

A.1 PARAMETERS OF THE HIGHEST MASS DIMUON CANDIDATE EVENT 125

A.2 PARAMETERS OF THE HIGHEST MASS WITH LOWEST COS(Θ^*) DIMUON CANDIDATE EVENT 125

ACKNOWLEDGMENTS

It seems to be an impossible task to adequately acknowledge all the people who have helped make this thesis come to fruition. There are literally thousands of people that spent countless hours developing the tools needed to accomplish this study. To all of those individuals who I have never met or never will meet, thank you!

This dissertation is the end of a path on which I have traveled most of my life. It started in 6th grade at Beaverton Middle School. My English teacher that year let us write a book report on any book in the library. The book I found was a on nuclear power. I was hooked on sub-atomic particles from that point forward. I cannot thank that teacher enough for allowing us the freedom to find what interested us and running with it. I would also like to thank Jim Faber, my 7th grade science teacher, for putting up with all of my questions and stubbornness. He was a great teacher.

At Michigan State University, I had the pleasure to have Prof. Jerry Cowen for my first physics class. He had such a sense of delight just being a physicist. Thank you for your enthusiasm and encouragement. You will be missed. I would also like to thank all the people in the High Energy Physics (HEP) department at MSU for allowing me the opportunity to work on the CDF Run II upgrade. Specifically, I would like to thank Prof. Joey Huston for that great introduction into the field of HEP. I would be remiss if I did not thank the wonderful people that I met while working in HEP at MSU. Mike Nila, Dean Shooltz and Ron Richards, thanks for

being such good friends and picking up the bar tab at the Peanut Barrel on more than one occasion.

To those I started graduate school with at The University of Notre Dame, I could not have picked a better group of people. I would like to thank them all for helping in innumerable ways during some difficult years, I could not have done it without them. Specifically, I want to thank Joe Snyder, he has become one of my best friends in the whole world and helped me keep my head on straight on more than one occasion. I would also like to thank my advisor, Prof. Mitch Wayne for helping me get seriously involved in the CFT at DØ. He would always take the time to listen to whatever I needed to discuss and allowed me a lot of freedom in the research I wanted to do.

In general the comments and direction I received from the New Phenomena group at DØ has been of great help. To all of the people in the DØ NP group, thank you. Furthermore, I would like to thank Prof. Greg Landsberg for taking me under his wing and helping me with many aspects of this analysis.

Now I would like to thank several individuals for helping me in a multitude of ways while I was at DØ. Avto Kharchilava, Sean Mattingly, Yuri Gershtein, Joe Kozminski, Drew Alton, Don Lincoln, and Jadwiga Warchol I can't thank you all enough for all your help and encouraging comments.

CHAPTER 1

INTRODUCTION

To understand the context in which this dissertation is written, it is important to have some understanding of human nature. Human beings are a part of this place called the universe along with many other living things. One of the biggest aspects separating humans from other creatures is the desire to fundamentally understand the world we live in. In other words, while other creatures simply exist in the universe, human beings have a need to grasp the universe. This may be best illustrated by the question "why" that tends to come out of a child's mouth.

The questions, "What makes this work?" or "Why is that the way it is?", have been asked by the human race for thousands of years. In ancient Greece, a paradigm was born suggesting that to understand the world, one must understand its basic building blocks. Throughout the intervening centuries we have attempted to further understand the universe by examining its fundamental constituents. The current culmination of this philosophy can be best described in what is called the Standard Model of high-energy (particle) physics.

1.1 The Standard Model

The Standard Model of high-energy physics (HEP) is a local gauge invariant relativistic quantum field theory based on the principle of least action [1]. Particles in this model are described as field excitations above the vacuum ground state.

The particles can be categorized into two groups based on their spin, the spin 1/2 fermions and spin 1 gauge bosons.

The fermion group contains the the matter particles, although some fermions may be massless. Furthermore, the fermion sector of the model can be decomposed into the leptons (ℓ) and quarks (q). The leptons and quarks can also be further categorized into one of three families (or generations) based on their properties. Table 1.1 shows the Standard Model fermions consisting of six leptons and six quarks. Each particle in Table 1.1 also has an associated anti-particle. For example, the positron (e^+) and anti-neutrino ($\overline{\nu_e}$) are the anti-particles of the electron (e) and the electron neutrino (ν_e), respectively.

Table 1.1

THE STANDARD MODEL FERMIONS

Generation	Particle	Name	Mass (MeV/c^2)	Charge (e)
		Leptons (spin 1/2)		
1	e	Electron	0.511	-1
1	ν_e	Electron neutrino	< 15 eV	0
2	μ	Muon	105	-1
2	ν_μ	Muon neutrino	< 0.17	0
3	τ	Tau	1,777	-1
3	ν_τ	Tau neutrino	< 24	0
		Quarks (spin 1/2)		
1	d	Down	~ 7.5	-1/3
1	u	Up	~ 4.2	2/3
2	s	Strange	~ 150	-1/3
2	c	Charm	$\sim 1{,}100$	2/3
3	b	Bottom	$\sim 4{,}200$	-1/3
3	t	Top	$\sim 174{,}000$	2/3

Combinations of these fundamental particles make up the visible matter in the universe. For instance combinations of quarks can form bound states called mesons

and baryons. A meson is a quark anti-quark pair bound state, whereas a baryon is a bound state of three quarks. The π^+ meson is an example of a meson which consists of a $u\bar{d}$ bound state. An example of a baryon is the proton which is made of a uud bound state. Furthermore, a bound state of an electron with the proton forms the hydrogen atom, which constitutes much of the universe.

As mentioned in Table 1.1 each fermion has a corresponding anti-particle which brings the number to twenty-four particles. This number does not reflect that the quarks have an additional degree of freedom called color charge. Each quark or anti-quark can have one of three different color charges, red (r), green (g) or blue (b). Once quark color is included the total number of matter particles within the Standard Model comes to forty-eight.

Now that the Standard Model components which make up matter have been introduced the various interactions which govern their dynamics will be discussed. Within the Standard Model three forces allow the matter particles to interact. There are the electromagnetic, strong, and weak forces. The gauge transformations, which are responsible for these interactions, follow the group structure: $SU(3)_C \otimes SU(2)_L \otimes U(1)_Y$. Here C stands for color charge, L designates left-handed interactions, and Y is weak hypercharge defined as $Y = 2(Q - I_3)$, where I_3 is the third component of weak isospin and Q is electric charge.

The $SU(3)_C$ component of the group structure describes the strong interactions which bind quarks together. Strong interactions within the Standard Model are mediated by massless particles called gluons. Typically strong interactions are described in a theoretical framework called Quantum Chromodynamics (QCD) [1].

Just as the $SU(3)_C$ part of the group describes how the strong interactions are governed in the Standard Model, the $SU(2)_L \otimes U(1)_Y$ sector describes how the electromagnetic and weak forces are incorporated. The mediating particles for the

weak force are the W and Z bosons, while the electromagnetic force is mediated by the photon. Electromagnetic interactions are responsible for how particles with charge interact with each other. The quantum theory which deals with this is called Quantum Electrodynamics (QED) [1]. Table 1.2 gives some information on the Standard Model gauge bosons which are the mediators of the three fundamental forces described above.

Table 1.2

THE STANDARD MODEL GAUGE BOSONS

Particle	Name	Force	Mass (GeV/c^2)	Charge (e)
γ	Photon	Electromagnetic	0	0
g	Gluon	Strong	0	0
$W^{\pm}$	W Boson	Weak	80.2	± 1
Z	Z Boson	Weak	91.2	0

The Standard Model is a very successful theory. One striking example of this is the prediction of the W and Z bosons as well as their masses, which were later experimentally verified. Another example of the success of the Standard Model is the prediction of the existence of the top quark, which was experimentally verified in the mid-1990s by the CDF and DØ collaborations [2]. Yet, there are issues the Standard Model does not address. One issue is that there are around twenty-five arbitrary free parameters within the Standard Model. To agree with observations some of these parameters must be related to other parameters to a very high precision [2]. Another issue is the Higgs mechanism giving masses to the various particles. While the Higgs mechanism is an important piece to the Standard Model, many aspects of it still remain a mystery. For instance, the Higgs mechanism predicts the existence of a new spin 0 particle called the Higgs boson, but this particle has not been observed

experimentally.

Perhaps the most obvious flaw with the Standard Model is it does not incorporate gravity in a consistent quantum mechanical way. This point cannot be overstated. The force holding the Earth in orbit around the sun, and ruling our everyday life is not fully addressed within the model which is supposed to explain everything. In the past there were many theoretical models attempting to address the issue of gravity, but most give no way to test them with current or foreseeable experimental facilities.

Because of these (and other) problems, physicists today believe that the Standard Model is not the final solution to the question of how the universe works. The Standard Model as we know it today is more likely just an approximation of the truth. The next step to true understanding will probably take the form of an extension to the Standard Model, which in a consistent manner addresses some or all the flaws in the current model. Or perhaps the truth will be revealed by changing, at a basic level, how we look at the fundamental particles themselves. Only time and effort will tell.

1.2 Motivation for This Research

Simply put, this research is done to probe for the existence of new physics. The Standard Model is a magnificent achievement, but it does not address some fundamental questions. For instance, where is the inclusion of the fourth (and some might say the most important) fundamental force, gravity? Also, why do calculations for the Higgs mass have divergences that would have to be fixed to precisions of 10^{-33}? There are still other problems with the Standard Model, but the two mentioned above are of primary concern in the context of this work. The research presented in this thesis constitutes a direct attempt to help answer the two

fundamental questions stated above.

1.3 Thesis Overview

The work described in this dissertation is part of a ongoing contribution to the search for large extra dimensions and extra heavy gauge bosons at the Tevatron's DØ detector. This thesis describes in detail the many aspects of the two searches. Chapter 2 gives an overview of the theory and phenomenology behind extra heavy gauge bosons and large extra dimensions. Chapter 3 outlines the experimental apparatus used to perform the searches. Chapter 4 describes the search for large extra dimensions in the dimuon channel, while Chapter 5 goes over the extra heavy gauge boson search in the same dimuon channel. Conclusions and a summary of results is given in Chapter 6. The Appendix shows event displays and information pertaining to two interesting candidate events. From this point forth it is assumed that $\hbar = c = 1$, thus all mass, momentum, and energy variables will be expressed in units of GeV.

CHAPTER 2

THEORIES AND PHENOMENOLOGY

The Standard Model (SM) does not appear to be a complete theory. Discussed are details about two possible extensions to the Standard Model. Ideas of large extra dimensions are examined as well as possible signatures at the Tevatron accelerator. In addition, some theoretical models predicting the existence of extra heavy gauge bosons are reviewed.

2.1 Motivation for New Physics

As mentioned in Chapter 1 the SM has proven to be a very successful theory. It allows the calculation of many observables and successfully predicted the existence of several new particles. Examples include the top quark and the W and Z bosons. While the SM has been experimentally verified to great precision, there are indications that the SM is only a low-energy approximation to a more general theory.

One indication that the SM is not a complete description of the physical world appears in the calculation of radiative corrections to the Higgs mass. At the one loop level there exist quartic self-interactions of the Higgs boson which are quadratically divergent. For these divergences to be canceled an additional mass counterterm (δM_h^2) term must be introduced. Also if unitarity is to be preserved in the scattering of longitudinal gauge bosons, the Higgs mass must be less than $\sim$ 800 GeV [3]. For the SM to be the ultimate theory, the cutoff to the divergence (Λ) must be of

the same order as the Planck scale, $M_{Pl} \approx 10^{19}$ GeV. With these limits and the following Higgs mass relation,

$$M_h^2 \sim M_{h0}^2 + \frac{\lambda}{4\pi^2}\Lambda^2 + \delta M_h^2, \tag{2.1}$$

we see that a counterterm must cancel the divergence to a precision of 10^{-33}, with $\lambda \sim \frac{M_H^2}{v^2}$ and $v = 246$ GeV [3]. While precisions of 10^{-33} are possible, this represents a large amount of fine tuning of parameters. This is known as the fine tuning problem.

Another problem with the SM is referred to as the hierarchy problem [4]. The hierarchy problem stems from the fact that the weak scale ($M_{weak} \sim 1000$ GeV) and the Planck scale differ by 10^{16} orders of magnitude. Another interpretation of this problem is to ask why the couplings for the strong, weak and electromagnetic forces differ so greatly from that of gravity?

The hierarchy issue and the fine tuning problem are considered to be major problems that the SM does not address. In addition, the SM contains many arbitrary parameters (especially quark masses), it does not explain CP-violation, the CKM matrix elements, or neutrino masses [1, 3]. Furthermore, the SM also does not explain the running of the strong, weak, and electromagnetic coupling constants as a function of energy scale [1]. In the next sections of this chapter we discuss a few possible extensions of the SM that may help address these important issues.

2.2 Extra Neutral Gauge Bosons

One way of resolving the inherent problems of the SM is by extending the gauge sectors of the theory. By doing this new particles are often predicted. In some cases these extra particles can be used to cancel the fine tuning problems with the SM. In the following section I discuss some of the ramifications of extending the $U(1)$

group sector of the SM.

As with the $U(1)$ group in the SM, extended $U(1)$ theories predict the existence of other neutral gauge bosons, collectively called Z's [5]. In most extended gauge theories the symmetry breaking scale is at sufficiently high energies that the associated extra bosons are beyond the reach of any current or planned experiment. However, there exist several models allowing the mass of a Z' to be relatively light, on the order of TeV scales [5]. Masses in this range could be detected by current experiments. The following sections examine a few of these models and review results from previous Z' searches.

2.2.1 Grand Unified Theory

Grand Unified Theories (GUTs) constitute the largest set of extended gauge theories. In general GUTs hope to solve the question of why the SM coupling constants vary as a function of energy. The postulated solution within a GUT is that the coupling constants will merge at some unification scale. GUTs propose that at some unification scale ($M_{GUT} \sim 10^{16}$ GeV), there exists an interaction with a single coupling constant describing the weak, strong, and electromagnetic interactions. Within the general scope of GUTs, the simplest symmetry group constructed still containing the Standard Model's $SU(3)$, $SU(2)$ and $U(1)$ is based on $SU(5)$. While this new group showed promise, it has been ruled out because it predicts a proton decay time experimentally excluded [1].

Other symmetry groups considered are $SO(10)$ and E_6. Contained within the $SO(10)$ GUT is an extra $U(1)$ sub-group. This can be seen from its maximal subgroup decomposition, $SO(10) \rightarrow SU(5) \times U(1)_\chi$ [5]. Likewise, the GUT based on the E_6 group decomposes into the following subgroup, $E_6 \rightarrow SO(10) \times U(1)_\psi$ [5]. The Z' corresponding to these possible GUTs are Z_χ and Z_ψ.

2.2.2 Left-Right Symmetric Model

One $SO(10)$ GUT extension to the SM postulates the existence of a right-handed version of the weak interaction giving $SU(2)_R \times SU(2)_L \times U(1)_{B-L}$ as well as an additional Z boson. This type of model is called the Left-Right Symmetric Model (LRM) [5]. One interesting feature of the LRM is that once $SU(2)_R$ is introduced it contains right-handed neutrinos. This has the effect of causing the generator of $U(1)$ to become baryon minus lepton number $(B - L)$, which is a physical observable. The LRM also accommodates small masses for left-handed neutrinos. In the LRM model the Z' is denoted as Z_{LRM}.

2.2.3 Superstring Theory

Another set of attractive extensions to the SM are supersymmetry and string theory. Within the past 20 years both of these theories have become very popular with experimentalists and theorists. Both supersymmetry and string theory predict a rich population of new particles that should be accessible near TeV scales.

One of the most widely accepted extensions to the SM is supersymmetry (SUSY). Basically SUSY is a concept that invokes a new symmetry between bosons and fermions [1]. This is accomplished by a supersymmetric operator, Q, which changes fermionic ($|f>$) and bosonic ($|b>$) fields in the following manner: $Q|f>=|b>$ and $Q|b>=|f>$. Essentially, this introduces new bosonic and fermionic fields which manifest themselves as new particles, collectively called sparticles. The inclusion of sparticles into mass loop corrections results in an exact cancellation of the problematic quadratic divergences inherent in the SM. This is a specific instance were an extension to the SM solves the fine tuning problem discussed above.

While many other theories do a reasonable job of fixing problematic aspects of the SM, string theory is currently the only theory able to incorporate gravity [1].

String theory postulates that the fundamental components of the universe are one dimensional strings, as opposed to the zero dimensional points used in field theories. Various configurations of these strings manifest the different observables seen in experiments. For example, a certain configuration of said strings causes an electron to have negative charge, while another causes the Z to have a mass of 91.19 GeV. As mentioned before, string theories naturally include gravity into their framework. The most interesting aspect of string theories is their prediction of the existence of extra dimensions beyond the known four. String theories conclude that these extra dimensions are not observed because they are compactified, or rolled up upon themselves, with a radius of compactification of $R \sim M_{Pl}^{-1}$ [6].

Both SUSY and string theory are of interest in their own right, but it is combination of SUSY with string theory to form superstring theory that is of interest here. The gauge group E_6 emerges in superstring theory when some of the higher dimensions are compactified [1]. From the previous section it was shown that the group E_6 contains a $U(1)_\chi$ and $U(1)_\psi$ component. In some superstring theories it is a linear combination of these components, $\sqrt{3/8}Z_\chi - \sqrt{5/8}Z_\psi$, which correspond to extra gauge bosons [5]. The Z' in such superstring theories are denoted Z_η.

2.2.4 Sequential Standard Model

The Sequential Standard Model (SSM) is a model where its Z' (Z'_{SSM}) is assumed to couple to quarks and leptons in the same way that the Z boson does in the SM. This implies that the Z'_{SSM} may only decay into the three known families of fermions. The SSM is not in the strictest sense a real theory, due to its lack of gauge invariance [5]. Although the SSM is not gauge invariant it is a useful standard. It is a common standard so that most experiments can make straightforward comparisons of their results. And it is because of this that the SSM is used in the

Z' analysis section of this thesis.

2.2.5 Previous Z' Searches

Experimentally there are two ways of searching for the existence of a Z'. First, the presence of a Z' can be probed indirectly from fits to high precision electroweak data. Second, one can look for the direct production of Z' and their subsequent decays at various collider facilities.

Due to the presence of possible extra gauge groups, a mixing between the SM Z and the Z' can occur. Changes in some of the measured values of SM parameters and observables results from this $Z - Z'$ mixing. Therefore, precise measurements of observables such as the Z-pole parameters, W mass, and weak neutral-current parameters can set bounds on the amount of $Z - Z'$ mixing allowed. From these constraints on $Z - Z'$ mixing, experiments can be done to constrain the Z' mass [5].

While indirect Z' searches rely on quantum mechanical state mixing, direct searches rely on explicit production of the Z'. Direct searches are typically categorized in terms of the initial state where a Z' is produced and the final state it decays into. For instance, at the Tevatron the initial state is a proton anti-proton collision ($p\overline{p}$), while at CERN the LEP collider used an electron positron collision (e^+e^-). Here the most common final states examined are those involving two oppositely charged leptons (*e.g.* dielectrons or dimuons).

While direct searches from e^+e^- colliders rule out Z' with masses less than a few hundred GeV, now the best limits come from $p\overline{p}$ colliders, where the Z' is produced via the Drell-Yan process and subsequently decays into two leptons. The CDF collaboration quotes limits on $\sigma(p\overline{p} \rightarrow Z' + X) \times BR(Z' \rightarrow l^+l^-) < 0.04$ pb at 95% C.L. for combined dielectron and dimuon final states [7]. Table 2.1 shows a summary of present Z' mass limits for the different models discussed above [5]. In Table 2.1 the

Exp/Author column refers to ether the experiment that published the stated result or the author of the specific paper that the result was calculated in.

Table 2.1

SUMMARY OF CURRENT Z' MASS LIMITS

Z' Models	Mass (95% CL)	Exp/Author	Comments
Z_{SSM} Sequential SM	> 1500 GeV	K. Cheung	precise electroweak
	> 690 GeV	CDF	ee, $\mu\mu$ combined
	> 670 GeV	DØ	ee channel
Z_{LRM} Left-Right Sym. Model	> 860 GeV	K. Cheung	precise electroweak
	> 630 GeV	CDF	ee, $\mu\mu$ combined
Z_χ $SO(10) \rightarrow SU(5) \times U(1)_\chi$	> 680 GeV	K. Cheung	precise electroweak
	> 595 GeV	CDF	ee, $\mu\mu$ combined
Z_ψ $E_6 \rightarrow SO(10) \times U(1)_\psi$	> 350 GeV	DELPHI	$Z - Z'$ mixing
	> 590 GeV	CDF	ee, $\mu\mu$ combined
Z_η E_6 models	> 619 GeV	G. Cho	precise electroweak
	> 620 GeV	CDF	ee, $\mu\mu$ combined

2.3 Large Extra Dimensions

Recent advances in the phenomenology of string theory suggest the previously unreachable Planck, string, and grand unification scales ($M_{\rm Pl}$, $M_{\rm st}$, and $M_{\rm GUT}$, respectively) may be sensed at the TeV range [8]. If this conjecture is correct, the phenomenology can be tested at current and future collider experiments. A possible realization of this idea was recently proposed by Arkani-Hamed, Dimopoulos, and Dvali (ADD) [6]. In their formulation, the SM particles are confined to a three dimensional wall or 3-brane, and the corresponding SM gauge interactions are therefore restricted to this brane as well. While the SM particles and fields are confined to the 3-brane, gravity is allowed to propagate in the n extra dimensions. In order to bring the apparent Planck scale (10^{19} GeV) to the TeV range, the size of these

n compactified dimensions has to be very large compared to $(M_{\rm weak})^{-1}$. Therefore, because gravity propagates in these large extra spatial dimensions (LED) it appears weak as seen by us on the 3-brane. In the following section I show how gravitational strength can be effected by the presence of LED.

The following reasoning produces the effective Newton constant in 4+n-dimensional space-time [6]. For a (3+n)-dimensional space, with n extra dimensions compactified on an n-torus with radii R, two test masses, m_1 and m_2, placed at the distance $r \ll R$ from each other, will feel a 3+n-dimensional gravitational potential, given by a (3+n)-dimensional Gauss's law:

$$V = \frac{m_1 m_2}{(M_{\rm Pl}^{[3+n]})^{n+2} r^{n+1}} \tag{2.2}$$

where $M_{\rm Pl}^{[3+n]}$ is the Planck mass in the 3+n-dimensional space. For $n = 0$, this becomes the familiar: $V = \frac{1}{M_{\rm Pl}^2}\frac{m_1 m_2}{r} \equiv G_N \frac{m_1 m_2}{r}$. However, if the masses are placed at the distance $r \gg R$ from each other, the gravitational flux can not penetrate the extra dimensions, and the potential is given by:

$$V = \frac{m_1 m_2}{(M_{\rm Pl}^{[3+n]})^{n+2} R^n\, r}, \tag{2.3}$$

and hence the effective 4-dimensional gravitational constant (as measured in the Cavendish experiment) is given by:

$$M_{\rm Pl}^2 = (M_{\rm Pl}^{[3+n]})^{n+2} R^n \equiv M_S^{n+2}\, R^n, \tag{2.4}$$

where M_S is the fundamental Planck scale. As with the $r \ll R$ case, Equation 2.3 becomes $V = \frac{1}{M_{\rm Pl}^2}\frac{m_1 m_2}{r} \equiv G_N \frac{m_1 m_2}{r}$ for $n = 0$. The previous equations result in an approximation for R of

$$R \sim \frac{1}{M_S}(M_{\rm Pl}/M_S)^{2/n}. \tag{2.5}$$

The assumption that the fundamental Planck scale, M_S is in the TeV range suggests that R for $n = 1$ is on the order of 10^8 km, comparable to the size of our

solar system. Therefore TeV range M_S with $n = 1$ can be ruled out by the known $1/r^2$ dependence of gravitational force at large distances. However, for $n \geq 2$ the expected R is less than 1 mm, and hence does not contradict existing gravitational experiments. For n larger than 2, the compactification radius drops as a power law (*e.g.*, $\sim$ 3 nm for $n = 3$). Thus $n = 2$ is the minimum allowed number of LED. Tabletop gravity experiments and astrophysical constraints produce tight limits on the fundamental Planck scale for the case of 2 extra dimensions. However, for $n \geq 3$ they are not helpful, leaving high-energy colliders as the only sensitive probe [9]. Current best lower limits on the fundamental Planck scale for $n \geq 3$ come from LEP and the Tevatron and are $\approx$ 1 TeV [10].

2.4 Phenomenology of Large Extra Spatial Dimensions at the Tevatron

Colliders use two primary methods to probe LED. The first is to look for the production of a real graviton recoiling against a gauge boson or a quark in the high-energy interaction (resulting in a monojet, or monophoton signature with large amounts of $\not\!\!E_T$ due to the graviton escaping detection). The second is to probe the effects of virtual gravitons in fermion or boson pair production. Both types of studies were performed at LEP and at the Tevatron. The Tevatron, specifically DØ, pioneered the search for LED at hadron colliders by analyzing dielectron and diphoton final states and the complementary, monojet channel [11, 12]. This dissertation focuses on probing for LED by way of virtual graviton effects. Specifically, this study looks for LED by analyzing the two muon (dimuon) final state at DØ . While LEP has done such a study in the past, this analysis is the first time LED has been probed using the dimuon channel at a hadron collider [10].

In this dissertation the experimental double differential cross section $\frac{d^2\sigma}{dM\,d\cos\theta^*}$ is used to probe the effects of LED. In this cross section, M is defined as the invariant

mass of the dilepton pair. The angle θ^* is defined as the angle in the dilepton center-of-mass frame between the positively charged lepton and the direction of the parton from the proton beam (Gottfried-Jackson frame) [10]. This choice of variables is useful because all the relevant information is contained in M and $\cos(\theta^*)$. This is because M and $\cos(\theta^*)$ span the entire phase space of the 2→2 scattering process. Therefore, there is no need to choose optimal variables (*e.g.*, forward-backward asymmetry, charge forward-backward asymmetry and so forth) or to optimize any kinematic criteria [10]. Using M and $\cos(\theta^*)$ to contrast SM and LED increases the sensitivity of this analysis over similar studies using just the invariant mass.

2.5 Dilepton Production at the Tevatron

At the Tevatron and specifically for this analysis we look for the effects of LED by studying virtual graviton exchange. Here the graviton is produced by quark anti-quark annihilation or by gluon fusion. For this analysis we look for the exchanged graviton to decay into a dimuon final state. Figure 2.1 shows the Feynman diagrams for the graviton exchange process as well as the dominant Drell-Yan background diagram.

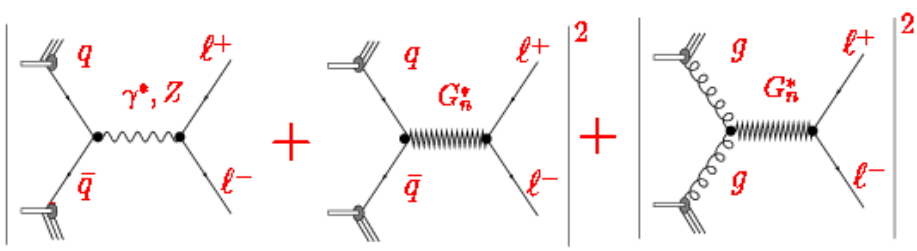

Figure 2.1. Feynman diagrams for dilepton production in the presence of large extra dimensions. In this figure G_n^* represents the graviton. Reproduced from Gupta *et al.* [13].

The graviton in this context is equivalent to an infinite tower of Kaluza-Klein

states with masses $M_{KK} = 2\pi k/R$ where $(k = 0, 1, 2, ..., \infty)$ [10]. Each of these Kaluza-Klein modes are weakly coupled as M_{Pl}^{-1}, but it is the very high multiplicity of states that greatly enhances the overall coupling to M_{weak}^{-1} scales. It should be noted the physical meaning of the scale M_S is an ultraviolet cutoff on the divergent sum of the modes of a $G_{\rm KK}$ in extra dimensions. While M_S is not exactly the fundamental Planck scale in this effective theory, it is expected to be closely related to the fundamental Planck scale and to differ from the fundamental Planck scale only by a factor of order unity [10].

The effects of LED are parameterized in this analysis via a single variable $\eta_G = \mathcal{F}/M_S^4$, where $\mathcal{F}$ is a dimensionless parameter of order unity and reflecting the dependence of virtual $G_{\rm KK}$ exchange on the number of extra dimensions. Different formalisms use different definitions for $\mathcal{F}$:

$$\mathcal{F} = 1, \text{ (GRW [14])}; \tag{2.6}$$

$$\mathcal{F} = \begin{cases} \log\left(\frac{M_S^2}{M^2}\right), & n = 2 \\ \frac{2}{n-2}, & n > 2 \end{cases}, \text{ (HLZ [15])}; \tag{2.7}$$

$$\mathcal{F} = \frac{2\lambda}{\pi} = \pm\frac{2}{\pi}, \text{ (Hewett [16])}. \tag{2.8}$$

It should be noted that only within the HLZ formalism does $\mathcal{F}$ depend explicitly on n. The parameter η_G has dimensions of TeV^{-4} with M_S in units of TeV and it describes the strength of gravity in the presence of LED.

Equation 2.9 gives the cross section for dilepton production, including the contributions from the SM, LED gravitons, and interference terms [10].

$$\begin{aligned} \frac{d^3\sigma}{dM_{ll}dydz} &= K\left\{\sum_q \frac{M_{ll}^3}{192\pi s} f_q(x_1) f_{\bar{q}}(x_2)\Big[(1+z)^2(|M_{LL}|^2 + |M_{RR}|^2)\right. \\ &\quad +(1-z)^2(|M_{LR}|^2 + |M_{RL}|^2) + \pi^2\eta_G^2 M_{ll}^4(1 - 3z^2 + 4z^4) \end{aligned}$$

$$
\begin{aligned}
&-8\pi e^2 Q_l Q_q \eta_G z^3 \\
&+\frac{8\pi e^2 \eta_G}{\sin^2\theta_W \cos^2\theta_W} \frac{M_{ll}^2}{M_{ll}^2 - M_Z^2} \left(g_a^l g_a^q \frac{1-3z^2}{2} - g_v^l g_v^q z^3 \right) \Bigg] \\
&+\frac{\pi M_{ll}^7}{128 s} f_g(x_1) f_g(x_2) \eta_G^2 (1-z^4) \Bigg\},
\end{aligned} \tag{2.9}
$$

where

$$
M_{\alpha\beta} = \frac{e^2 Q_l Q_q}{\hat{s}} + \frac{e^2}{\sin^2\theta_W \cos^2\theta_W} \frac{g_\alpha^l g_\beta^q}{\hat{s} - M_Z^2}, \qquad \alpha, \beta = L, R \tag{2.10}
$$

With $\sqrt{s}$ defined as the center-of-mass energy of the $p\overline{p}$ collision, $z \equiv \cos\theta^*$, y is the rapidity of the lepton pair, and $f_{q/g}(x)$ is the parton distribution function. Here it is assumed that $M_S^2 \gg \hat{s}, |\hat{t}|, |\hat{u}|$ where $\hat{s}, \hat{t}, \hat{u}$ are the Mandelstam variables corresponding to the partonic process. In the equations above, $\hat{s} = M_{ll}^2$, $x_{1,2} = \frac{M_{ll}}{\sqrt{s}} e^{\pm y}$, $g_L^f = T_{3f} - Q_f \sin^2\theta W$, $g_R^f = -Q_f \sin^2\theta W$, $g_v^f = (g_L^f + g_R^f)/2$, and $g_a^f = (g_L^f - g_R^f)/2$. The sum in Equation 2.9 is over all possible $q\overline{q}$ initial states. To account for NLO QCD corrections, a constant K-factor is included in the cross section. The K-factor used in this analysis is 1.3 [10]. Further details concerning the K-factor will be discussed in Chapter 4 of this thesis. Obtaining the double differential cross section $\frac{d^2\sigma}{dM d\cos\theta^*}$ requires integrating the triple differential cross section in Equation 2.9. Integration is done over the rapidity y and the parton distribution functions by using a variable transformation of $x_{1,2} = \frac{M}{\sqrt{s}} e^{\pm y}$ with a Jacobian factor of $\hat{s}/2M$ [10].

CHAPTER 3

THE EXPERIMENTAL APPARATUS

Two primary instruments at the Fermi National Accelerator Laboratory (FNAL) produce the data used for this analysis: the Tevatron accelerator and the upgraded DØ detector. The Tevatron accelerator creates proton anti-proton ($\overline{p}p$) colliding beams with 1.96 TeV center of mass energy. The DØ detector measures the final state particles coming from the colliding beams.

3.1 Luminosities and Cross Sections

In high energy physics, many measurements are expressed in terms of a cross section, σ. This is the interaction probability per unit flux. For collider experiments, particle flux comes from the colliding beams and is called the luminosity, $\mathcal{L}$. Luminosity is proportional to the square of the number of particles passing through a unit area per unit time. Most often luminosity is expressed in units of $\mathrm{cm}^{-2}\mathrm{s}^{-1}$. Cross sections in high energy physics are given in barns, where 1 barn = $10^{-24}\mathrm{cm}^2$. Therefore, the rate for a given process to occur, R, is then

$$R = \sigma\mathcal{L} \tag{3.1}$$

where R is in Hertz (Hz). While the rate is interesting, the total number of expected events, N, of a specific type is what is normally measured in high energy physics.

The following relationship defines the number of expected events

$$N = \sigma \int \mathcal{L} dt, \tag{3.2}$$

where the quantity $\int \mathcal{L} dt$ is the luminosity integrated over time and is referred to as the integrated luminosity. Because time is integrated out and cross sections are given in barns, integrated luminosity has units of inverse barns. For the first part of Run II at the Tevatron, called Run IIa, the goal is to collect 2 fb^{-1} worth of collisions. For this thesis approximately 170 pb^{-1} of integrated luminosity was collected and used. Therefore, if the process we are looking for has a σ of 1 pb we would expect to produce 170 such events.

3.2 The Fermilab Accelerator

The Fermilab accelerator complex is the world's most powerful high energy particle physics laboratory. It delivers proton and anti-proton beams each with energies of 0.98 TeV. When running in collider mode, these beams collide with a center-of-mass energy of 1.96 TeV. The collider consists of many different types of accelerators. Figure 3.1 shows a schematic view of the entire Tevatron complex. These accelerators have been integrated with great care and precision to produce energies that push the frontier of knowledge forward. A overview of the different accelerators and how they tie together to produce the collisions that are studied is given here. Further details are given in the following additional references [17].

3.2.1 The Preaccelerator

At the front end of the proton acceleration process is the preaccelerator. The process begins with hydrogen gas released into a magnetron surface-plasma source. An electric field produced between the magnetron's anode and cathode strip off the electron from the hydrogen atom. The free protons are then attracted to the

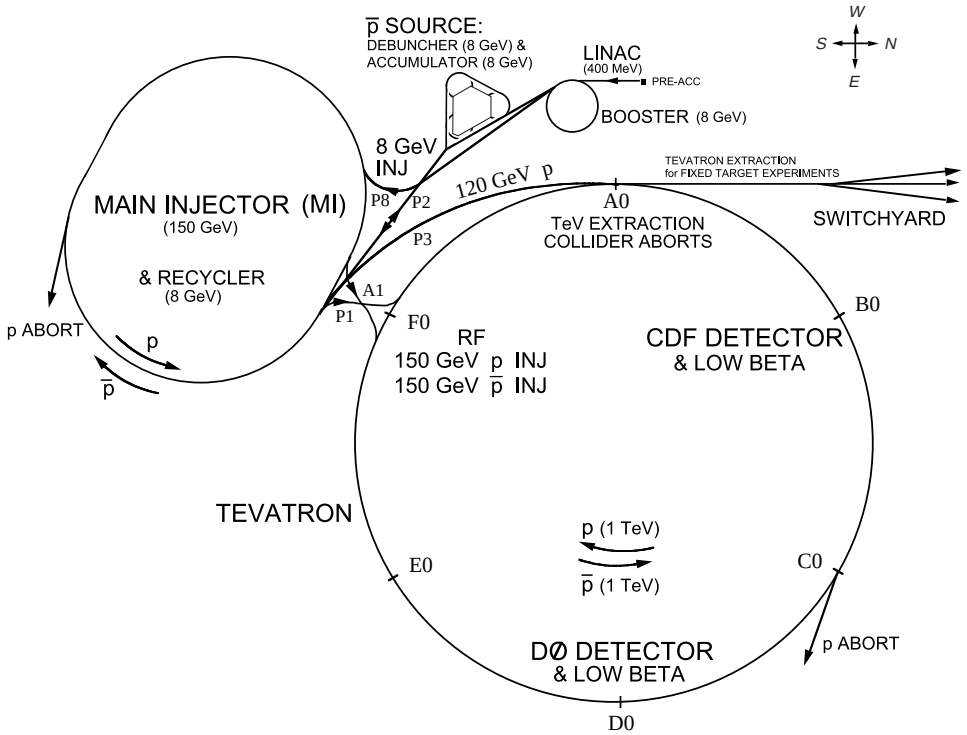

Figure 3.1. Schematic of the Run II Fermilab accelerator complex. Adapted from [18].

cathode's surface, where they collect electrons and are subsequently disengaged by the stream of bombarding atoms. If the released protons happen to capture two electrons, they become H^- ions and a magnetic field causes them to spiral out the opposite side of the magnetron source. An extractor plate accelerates the ions to a kinetic energy of 18 keV. Further acceleration of the H^- ions is done by using a electrostatic Cockroft-Walton accelerator, which propels them to an energy of 750 keV.

3.2.2 The Linac

The Linac, a linear accelerator, is the next stage of the acceleration. The Linac accelerates using two stages illustrated in Figure 3.2. An electric field pulls the H^- ions through the start of the Linac's beam tube. These ions then enter a shielded region, and meanwhile the polarity of the electric field is reversed. This prevents more ions from entering, thus creating a localized bunch of ions, rather than a steady stream from the preaccelerator. Upon exiting the shielded region the electric field is reversed again giving the ions another boost of acceleration. This is done several times over a 130 meter long distance. At the end of the Linac the ions emerge with a kinetic energy of 400 MeV.

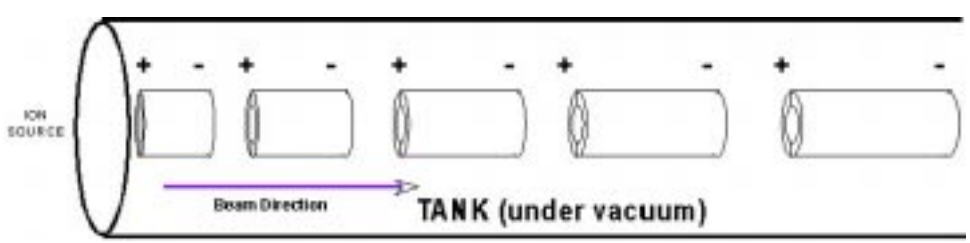

Figure 3.2. Illustration of the Linac. Adapted from [17].

3.2.3 The Booster Synchrotron

The Booster is a 1570 feet in circumference synchrotron ring, this is the first synchrotron accelerator that the beam encounters. Just before injection into the Booster a debuncher is used to reduce momentum spread of the beam. This removes the 805 MHz structure due to the Linac. After debunching the H^- ion beam is passed through a thin carbon foil. The carbon foil strips the two electrons off of the ion, leaving only the proton. The subsequent protons are constrained to a circular orbit by the use of bending magnets. Quadrupole focusing fields from the magnets help to keep the beam from diverging. A set of radio frequency (RF) cavities steadily increases the momentum of the proton beam as it revolves around the ring. To maintain the same circular orbit with increasing beam momentums, both the RF frequency and magnetic field strength are increased in a synchronous manner. This is the basic idea behind all synchrotron accelerators. After about 20,000 revolutions around the Booster ring the proton beam attains an energy of 8 GeV. In the Booster the proton beam is again bunched into a pulse train of about five to seven bunches. Each bunch contains 5-6$\times 10^{10}$ protons.

3.2.4 Main Injector

The primary upgrade to the accelerator for Run II is the Main Injector synchrotron. Two miles in circumference, this ring replaces the Main Ring that was used in Run I of the Tevatron. With the Main Injector there is a factor of three increase in the number of protons that can be delivered to the Tevatron over what was possible from Run I. Also, the Main Ring was located in the same enclosure as the Tevatron, leading to significant beam halos and backgrounds in the colliding detectors. This is no longer an issue since the Main Injector is located outside the Tevatron. The Main Injector receives the 8 GeV proton beam from the Booster and

proceeds to coalesce the bunches into a single high intensity bunch of approximately 5×10^{12} protons. The job of the Main Injector is two fold. Deliver the proton beam to the Tevatron with energy of 150 GeV while simultaneously delivering a 120 GeV proton beam to the anti-proton facility. Once anti-protons are produced the Main Injector accelerates them to 150 GeV as well and then injects that beam into the Tevatron.

3.2.5 The Anti-proton Source

As mentioned earlier in this chapter the Tevatron collider is a proton anti-proton ($p\overline{p}$) collider. While protons are relatively easy to produce, anti-protons are much more difficult to produce in large quantities. The intensity of the $\overline{p}$ beam is the primary limiting factor for the Tevatron. Anti-protons are produced by using the 120 GeV proton beam from the Main Injector. This proton beam is directed to strike a 10 cm diameter, 2 cm thick disk made of nickel [19]. There are many secondary particles from the proton-Ni collision, including anti-protons. Immediately downstream from the nickel target is a cylindrical collection lens made of lithium. Lithium is used because it is a conductor and has very low density. The low density minimizes absorption and scattering of the anti-protons. A large current (peaked at 670 kA) is applied to the lens, thus setting up a solenoidal magnetic field. This field tends to bend the secondaries such that they travel parallel to each other. A illustration of the setup used is shown in Figure 3.3. Following the collection lens is a pulsed dipole magnet that selects 8 GeV negatively charged particles out of the secondaries. Not by accident the peak energy for anti-protons from a 120 GeV proton on Ni collision is near 8 GeV.

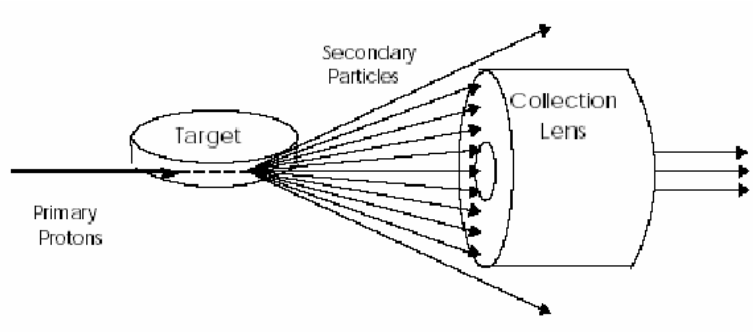

Figure 3.3. Illustration of $\overline{p}$ production. Adapted from [19].

3.2.6 The Debuncher and Accumulator

The 8 GeV anti-protons from the source are sent to two anti-proton storage rings, the Debuncher and the Accumulator, contained in the same tunnel. The tunnel housing these storage rings has rounded triangle type geometry with a circumference of roughly 1700 ft. Both the Debuncher and Accumulator contain several magnetic devices and RF cavities. One purpose of the Debuncher is to reduce the momentum spread of the anti-protons arriving from the source. Applying stochastic cooling to the anti-protons restricts their transverse oscillations and helps keep the anti-protons on an ideal orbit around the ring. The cooling and momentum manipulation allows the Debuncher to achieve greater efficiency transferring anti-protons to the Accumulator [19]. The purpose of the Accumulator is to muster large quantities of anti-protons and to arrange them into bunches having the same time structure as the protons already in the Main Injector. This is accomplished by further RF and cooling techniques. Accumulating stacks of 10^{12} anti-protons, which is a typical amount used in Run IIa, usually takes several hours. Once the stack reaches the amount desired the anti-proton beam is transferred to the Main Injector where it is accelerated to 150 GeV.

3.2.7 The Tevatron

The Tevatron is a 4-mile circumference synchrotron ring where the final stage of acceleration occurs. It utilizes superconducting magnets that produce magnetic fields of 4 Tesla. Using the high magnetic fields and large circumference, the 150 GeV beams delivered from the Main Injector are accelerated up to a energy of 0.96 TeV. Once this high energy is achieved, low-beta quadrupole magnets squeeze the beams to small transverse dimensions. There are two different locations where this happens. One is designated BØ and the other is DØ. These two regions of the smallest transverse beam dimension are where the $p\overline{p}$ collisions are initiated. The Collider Detector Facility (CDF) is located at the BØ interaction region while the DØ detector is located at the DØ region.

As discussed above the final Tevatron beams are not continuous. The Tevatron beams are in reality just groups (bunches) of protons and anti-protons with a certain time structure. The Tevatron operated with 36×36 $p\overline{p}$ bunches with a 396 ns bunch crossing during Run IIa.

3.3 Coordinate Systems and Other Conventions at DØ

Before discussing the DØ detector, it is useful to define the DØ coordinate system and some basic concepts. DØ uses a standard right-handed coordinate system. This system defines the $+x$ axis to be a vector pointing radially outward (east) from the center of the Tevatron ring. Pointing vertically upward is the $+y$ axis. The $+z$ axis is orthogonal to the x and y axis such that it creates a right-handed system. Protons in the Tevatron travel in the $+z$ direction, which corresponds to south. The anti-protons in the Tevatron travel in the $-z$ direction. At DØ it is convenient to use a combination of cylindrical and spherical coordinates (z, ϕ, θ). The polar angle θ is defined from the $+z$ axis, while the azimuthal angle ϕ is the angle around the $+z$ axis

with ϕ=0 being the $+x$ direction and ϕ=$\pi/2$ is the $+y$ direction. For an illustration of this choice of coordinates see Figure 3.4. DØ utilizes several kinematic quantities, including transverse energy (E_T) and transverse momentum (p_T), where E_T=$Esin\theta$ and p_T=$psin\theta$. The motivation for using these quantities is because in $p\overline{p}$ collisions the center-of-mass energy ($\sqrt{s}$) is not fixed [20]. This is due to the parton (quark and gluon) structure of the nucleon being collided, because partons carry only a fraction of the total nucleon energy. Therefore, scattering of these partons, which may have different energies, results in a center-of-mass frame different than the lab frame. In addition the total energy released from the collision is only a fraction of the total beam energy. This is due to nucleon remnants called spectators carrying away energy down the uninstrumented beam pipe. A total energy balance cannot be used to analyze the collision because a significant portion of the beam energy escapes detection. Instead the transverse energy balance is used because the total transverse energy before the collision is zero and the detectors are specifically built to measure nearly all of the transverse energy from the collision.

At DØ another kinematic variable used is rapidity, y. This is used in place of the polar angle θ. The rapidity is defined as

$$y = \frac{1}{2} ln \left[\frac{E + p_z}{E - p_z} \right]. \tag{3.3}$$

The rapidity is a more logical quantity to use than θ due to the rapidity's Lorentz invariant nature. Although y is useful, the quantity most often utilized is the pseudo-rapidity, η, which is the the ultra-relativistic limit of y when $m/E \rightarrow 0$. The pseudo-rapidity is defined as

$$\eta \equiv -ln\left[tan(\theta/2)\right] = \tanh^{-1}(\cos\theta). \tag{3.4}$$

In a $p\overline{p}$ collider experiment such as DØ the x and y dimensions of the colliding

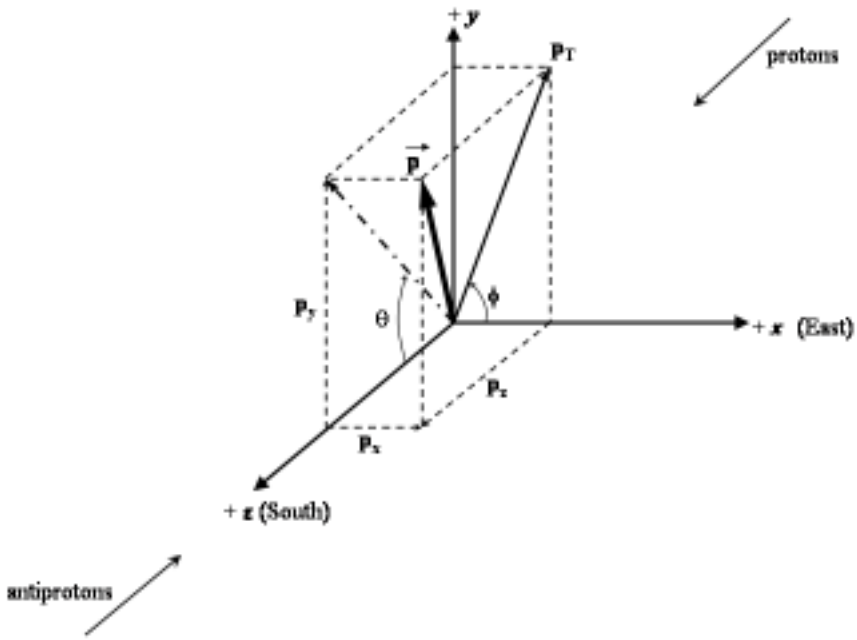

Figure 3.4. View of the DØ coordinates and p_T.

beams tend to be very small, but where the actual collisions take place in the z dimension is not as constrained. Due to this structure the primary interaction point has a Gaussian distribution in the z coordinate with mean at z=0 and σ_z=28 cm. Because of the beam structure discussed above there is another pseudo-rapidity useful in a hadron collider experiment such as DØ, the detector pseudo-rapidity, η_d. It is the pseudo-rapidity computed with respect to an interaction point whose longitudinal position is at $z = 0$. Because the real interaction point's position is distributed around $z = 0$, see Figure 3.5, η and η_d may be different.

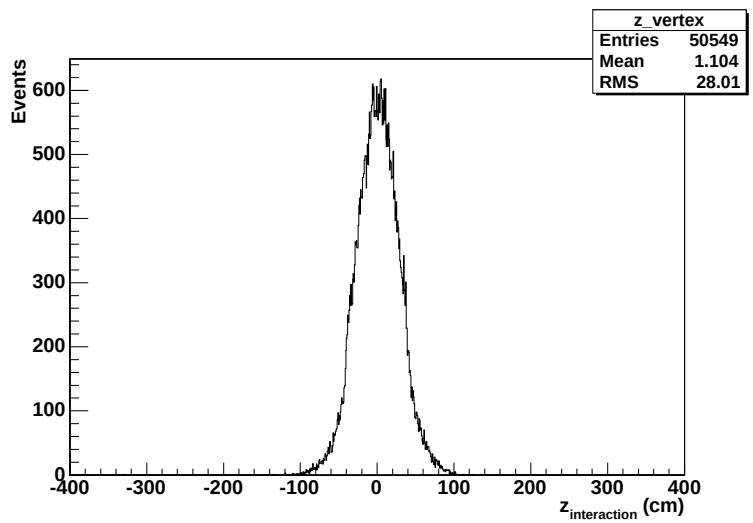

Figure 3.5. Distribution of the interaction point's z-axis position.

3.4 The Run II DØ Detector

The DØ detector is a nearly-hermetic multipurpose particle detector. Initial operation started in 1992 with Run I of the Tevatron accelerator. The primary physics focus for this detector in Run I was the study of high mass and large p_T phenomena. During its operation, the detector has been a key contributer to modern experimental high energy physics. One example of this was the discovery of the top quark in

1995 together with CDF [21]-[22].

The DØ detector has gone through a major upgrade for the start of Run II. Figure 3.6 shows an $r - z$ view of the upgraded DØ detector. A completely new tracking system was installed along with a new superconducting solenoid magnet. New readout electronics were installed for the calorimeter system. The muon systems have both new hardware and new electronics for readout. In addition, the data acquisition systems were completely upgraded. The rest of this chapter examines the details of the various systems of the Run II DØ Detector.

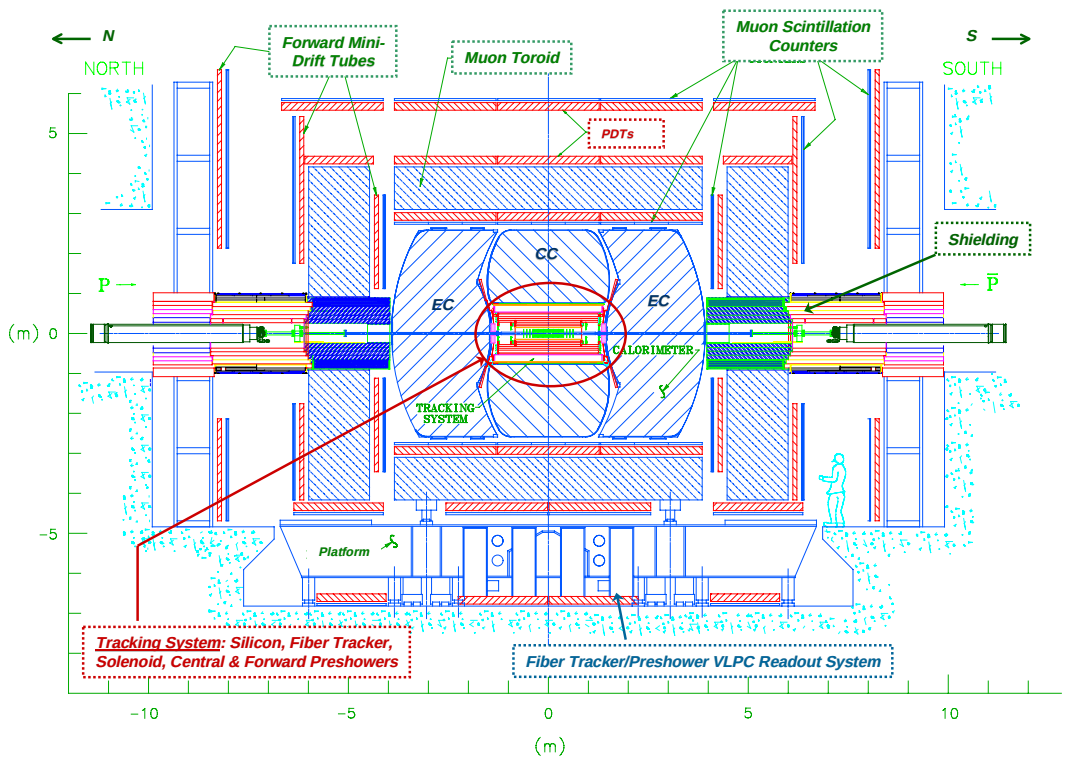

Figure 3.6. An $r - z$ view of the Run II DØ detector. Adapted from [18].

Because the detector went though a major upgrade, the physics goals for DØ have also been expanded to utilize the new technologies now included in the detector. The new tracking system opens up the potential for a vigorous B-physics program.

These upgrades will also help DØ continue to improve knowledge of the top quark, W and Z bosons, as well as perturbative and non-perturbative QCD. The upgrade also enhances the search for new particles, including searches for the Higgs boson, gravitons, and other manifestations of new phenomena beyond the Standard Model.

3.4.1 Tracking System

The upgraded detector uses an entirely new tracking system. This consists of two subsystems: the Silicon Microstrip Tracker (SMT) and the Central Fiber Tracker (CFT). Surrounding these subsystems is a superconducting solenoid magnet, which provides a field of 2 Tesla parallel to the beam direction. In combination with the magnetic field, the trackers are designed to perform charged particle detection and momentum measurements over a large range of pseudo-rapidity ($|\eta| \leq 3$). In addition to this, the tracking system gives secondary vertex measurements for the identification of heavy flavors. Figure 3.7 shows a view of the tracking system.

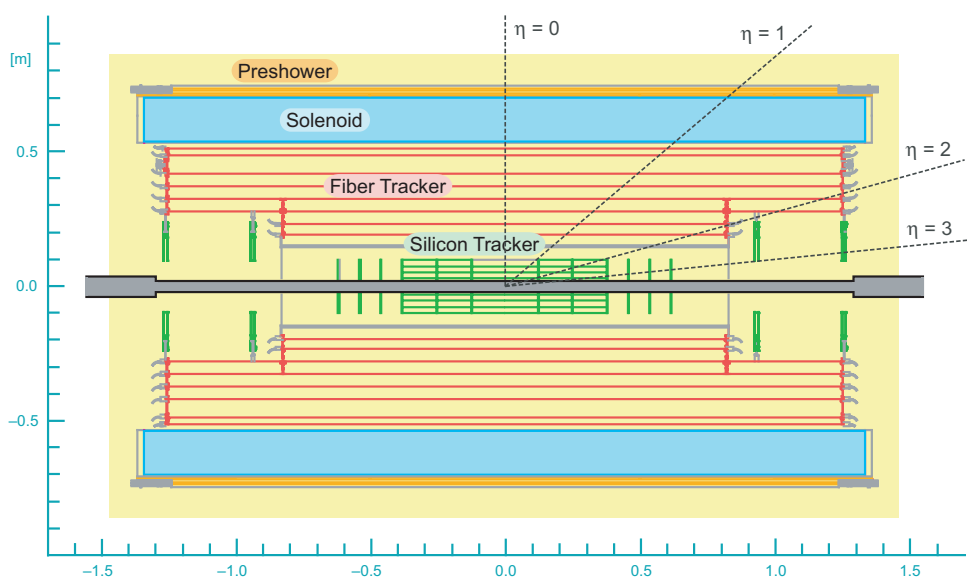

Figure 3.7. View of the DØ tracking system. Adapted from [23].

3.4.2 The Silicon Microstrip Tracker

The first part of the DØ detector encountered by the particles from the collisions is the SMT [24]. It is the highest resolution sub-detector of DØ as well as the one closest to the interaction region. The detector is a hybrid system using barrel and disk geometries made from silicon micro-strip detectors. This design geometry is motivated by the bunch structure of the colliding proton and anti-proton beams. Due to this structure the interaction point is Gaussian distributed in the z coordinate with mean at z=0 and σ_z=28 cm. Therefore it is important to design a detector so all tracks are predominantly perpendicular to the detector surfaces for all η. In this hybrid design, high η tracks are primarily reconstructed by the disks, while lower η tracks are found with the barrels.

The barrel part of the detector is formed by six sections each 12 cm long in z, consisting of four concentric layers. Silicon ladders make up the layers. A ladder is made from two 300 μm-thick wafers positioned end-to-end with electrical micro-wire bonded contacts for each layer. Layers two and four of all barrel modules are double-sided small-angle (2 degree) stereo detectors with a 62.5 μm pitch. Layers one and three of the central four barrels have double-sided large-angle (90 degree) stereo detectors with a pitch of 153.5 μm. Layers one (closest to the beam pipe) and three of the outer two barrels consist of single-sided axial detectors which have a 50 μm pitch.

Interspersed within the barrels are twelve 8 mm-thick disks, called F-disks. Each disk consists of twelve overlapping double-sided detector wedges. The readout strips on the two sides are laid out with angles of $\pm$15 degrees with respect to the symmetry axis of the wedge, thus giving it a effective 30 degree stereo angle. These detectors have a pitch of 50 μm for the p-doped side of the silicon and a pitch of 62.5 μm for the n-doped side. Another set of disks called H-disks are placed fur-

ther out from z=0 on both sides of the detector. These disks consist of single-sided silicon wedges with a pitch of 81 μm. The H-disks extend tracking coverage out to $|\eta|$=3.

Beryllium bulkheads provide structural support for the detector. These bulkheads not only serve as support, but also provide cooling water to the detector through channels machined into them. The beryllium bulkheads are mounted on carbon fiber half-cylinders for further support. Figure 3.8 shows a three dimensional rendering of the SMT detector

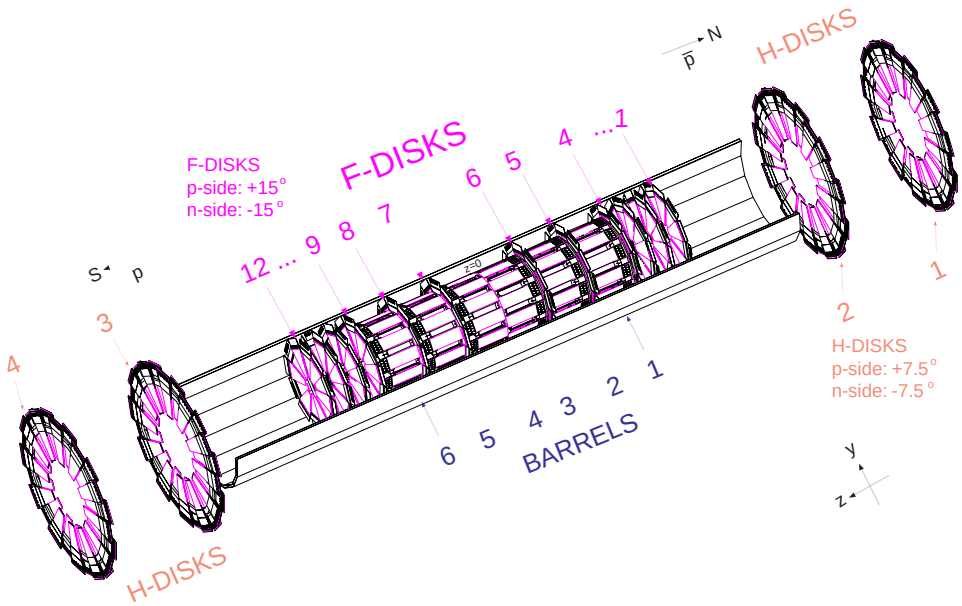

Figure 3.8. Three dimensional view of the SMT. Adapted from [18].

The SMT detector has approximately 793,000 readout channels with a $r\phi$ hit resolution of approximately 10 μm. Hit resolution of this scale helps achieve two goals for the experiment. First, it allows the identification and reconstruction of vertices displaced from the primary vertex. Figure 3.9 shows an illustration of displaced vertex finding. Second, the hit resolution helps the momentum resolution

for very high p_T tracks. Secondary vertex finding is very important for any physics involving b or c quark decays, while good resolution at high momentum is important for physics searches involving high mass particles.

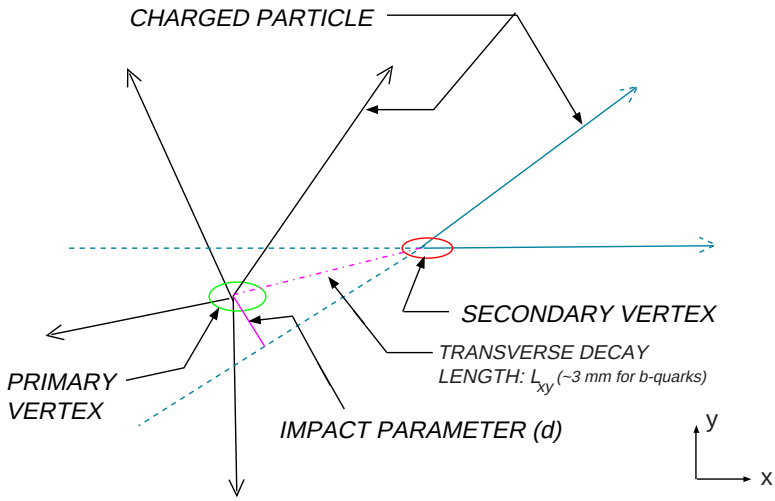

Figure 3.9. Drawing of a displaced vertex originating from a b or c quark decay. Adapted from [18].

3.4.3 The Central Fiber Tracker

Surrounding the SMT is the outer tracking system, the CFT [25]. The SMT and CFT do most of the charged particle tracking at DØ. An important function of the CFT is measuring the p_T of charged particles going through the detector. By measuring the curvature of tracks in the 2 Tesla solenoidal magnetic field, the CFT determines the p_T and the charge of the traversing particle tracks. In addition to these measurements, the CFT also provides fast Level 1 track triggering in the range $|\eta| < 1.6$.

The CFT consists of 76,800 scintillating fibers completely covering eight concentric support cylinders. These cylinders are made of carbon fiber and occupy the radial space from 20 to 51 cm. The inner two cylinders are 1.7 m long while

the outer six are 2.5 m long. Differences in length accommodate the silicon H-disk detectors located at high-η. Each cylinder is totally covered by two doublet layers of scintillating fibers. A doublet layer consists of two mono-layers of fibers placed together such that one mono-layer is offset by one half of the fiber spacing with respect to its partner. This configuration compensates for geometric gaps between adjacent fibers in a monolayer and provides a detection efficiency per doublet layer of nearly 100 percent. The innermost doublet layer on each cylinder is mounted along the axial direction (*i.e.* the fibers are parallel to the beam direction). On top of the axial layer another doublet is mounted at alternating u or v stereo angles of approximately 3 degrees. From the inner to outermost barrel the orientations for the layers follow the pattern xu-xv-xu-xv-xu-xv-xu-xv, where x is the axial doublet layer. Figure 3.10 shows a view of the CFT as well as an illustration of the doublet layer configuration.

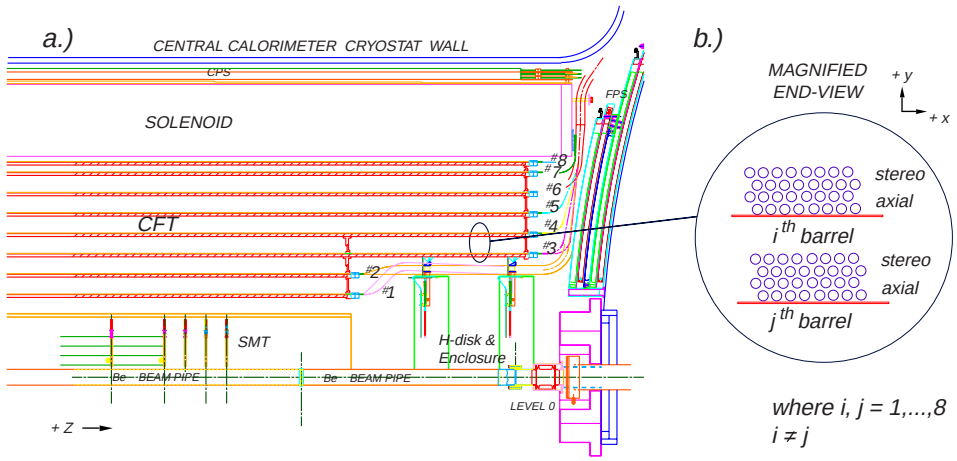

Figure 3.10. a) A quarter $r - z$ view of the CFT detector showing the nested eight barrel design. b) A magnified $r - \phi$ end view of the two ribbon doublet layer configuration for two different barrels. Adapted from [18].

During assembly, fibers are grouped into 256 channel ribbons which mount onto the carbon fiber cylinders with an accuracy better than 40 μm [26]. Studies using

representative CFT ribbons in a cosmic ray test stand have shown a doublet position resolution of $\approx 100\ \mu$m for single muons. (See Figure 3.11.)

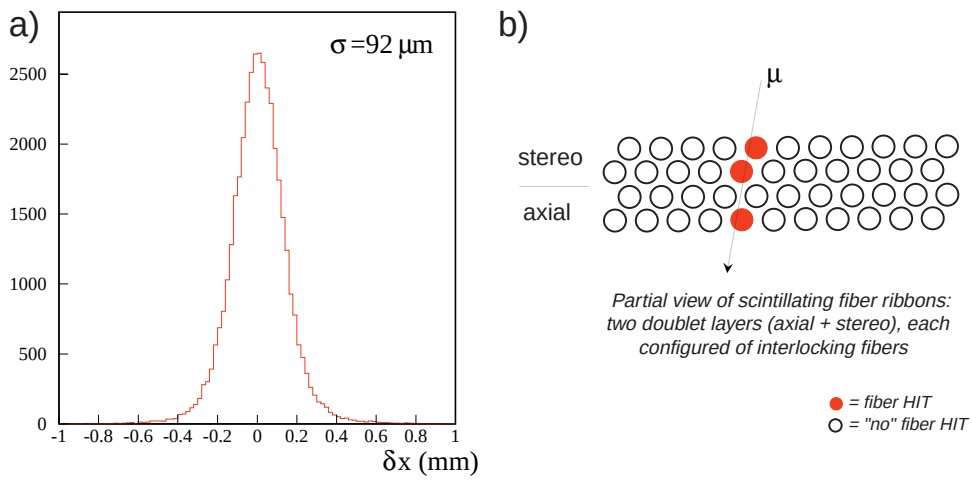

Figure 3.11. a) The position resolution distribution measured in the CFT cosmic ray test stand. b) An end view of the interlocking doublet ribbon configuration used by the CFT. Adapted from [18].

The scintillating fibers used in the CFT consist of a polystyrene core doped with 1 percent P-terphenyl and 1500 ppm 3-hydroxyflavone having peak scintillation at 530 nm [27]. Surrounding the 775 μm diameter core are two thin 15 μm claddings, the first made from acrylic and the second with a fluoro-acrylic material. These fibers vary in length from 166 to 252 cm. At one end of each scintillating fiber an aluminum mirror coating reflects light back into the fiber. At the other end the ribbon of 256 fibers inserts into a custom-machined optical connector. This end is diamond-finished giving optimal light transmission into the readout portion of the CFT. The readout end for the axial ribbons is at the south end of the CFT, while the stereo ribbon readout is on the north end. At the readout end of the ribbon, connectors are mated to a clear waveguide bundle of 256 fibers. This end of the bundle utilizes a matching optical connector and has also been diamond-finished.

The clear fibers making up this waveguide are structurally and chemically identical to the scintillating fibers, but they do not contain fluorescent dyes. The bundle of clear fibers are quickly grouped together and contained in a flexible plastic tube. The tube provides physical and light protection for the waveguides. Waveguides for the CFT range in length from 7-12 meters, which allows the light to be transported outside the central detector area, down into the readout platform.

After transporting the light from the CFT, the waveguides are connected to a set of rectangular modules called cassettes which are set into a liquid helium cryostat. The light is guided through the cassettes to a set of devices called Visible Light Photon Counters (VLPCs), a silicon-avalanche based photon detector [27]. Operating at temperatures near 9 K, these detectors have a quantum efficiency of over 80 percent, a gain of 20,000-50,000, a rate capability of at least 20 MHz, and a noise rate of less than 0.1 percent. Here the scintillation light from the CFT is converted into an electrical signal and sent to front-end electronics boards for digitization and readout [25].

On the readout boards the VLPC signal is sampled by a discriminator called the SIFi Trigger (SIFT) chip. The VLPC signal is also simultaneously sent to a Silicon VerteX (SVX) chip and to the CFT trigger system. This signal is stored in the SVX chip within a analog pipeline until a trigger decision is made or 32 beam crossings have occurred since the signal was produced. If the trigger system issues an accept, then the SVX digitizes the signal and reads it out. The SIFT discriminator pattern which caused the SVX to readout is also appended to the SVX information. If no trigger decision is made or 32 beam crossings have passed, the signal information is discarded.

The CFT trigger is implemented by using the SIFT output and hardware utilizing field programmable gate arrays (FPGA). Only axial layers are used as hits for

the trigger and the CFT trigger divides the detector into 80 azimuthal sectors for fast operation. Coincidences between hits on all eight layers form a track. These tracks can be combined with triggers from other parts of the detector, such as the muon system to form a muon trigger. When a good trigger is fired all the fiber layers will then be read out. Using a scintillation based tracker allows for the implementation of a fast Level 1 trigger, which is useful in rejecting background events that otherwise would be written out to tape. More on the DØ trigger system will be discussed later in this chapter.

3.4.4 The Central and Forward Preshower Detectors

Just beyond the tracking system are the preshower detectors, another set of detectors completely new to DØ. The preshower detectors aid in electron and photon identification and triggering. They provide early energy sampling for particles having just traveled through the solenoid. This is important because the solenoid contains large amounts of dense uninstrumented material. Thus, the preshower detectors help account for electromagnetic energy otherwise lost. Along with helping with calorimetry the preshower detectors are precise enough to help with tracking.

In the central region is the Central Preshower Detector (CPS) [28]. As stated above the CPS functions both a calorimeter and tracker. This detector is cylindrical in geometry with a radius of 72 cm and covers the region of -1.2 $< \eta <$ 1.2. It resides in the 51 mm gap between the solenoid coil and the central calorimeter cryostat. The CPS consists of three layers of scintillating strips. The innermost layer is an axially arranged layer, while the two outer layers are arranged at stereo angles. The stereo angles for the two outer layers are $\pm$23 degrees. The scintillating strips have a triangular cross section with a 7 mm base and a 1 mm diameter hole containing a wavelength shifting fiber embedded in it. Figure 3.12 shows the positioning of

the CPS and a view of the scintillating strips from which it is made. Similar to the CFT, clear fiber optics transmit scintillation light from the CPS to the VLPC system located on the platform below. The CPS has a total of 7680 channels of readout. Readout from the CPS axial layer is integrated with the CFT readout as a ninth layer and used in the Level 1 electron trigger.

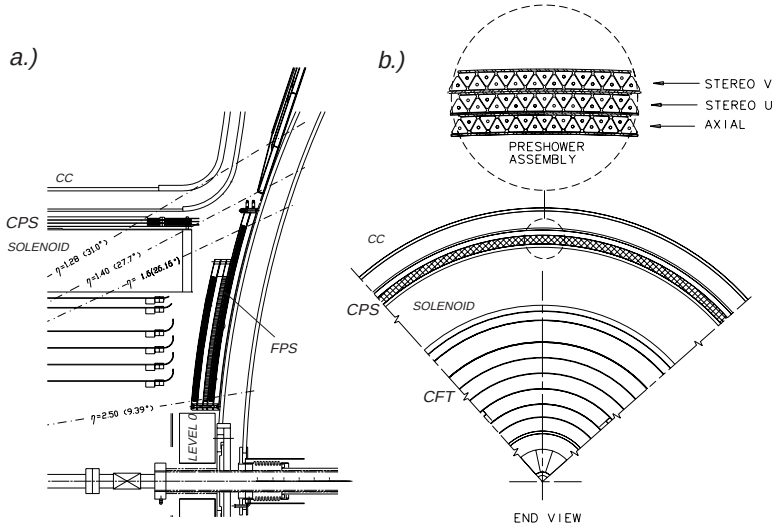

Figure 3.12. a) Shows a $r - z$ semi-quarter view of the CPS detector. b) A cross-sectional $r - \phi$ end view of the CFT and CPS detectors. The inset shows a magnified view of the nested triangular strips and layer configurations for the CPS. Adapted from [18].

In the forward regions ($1.4 < |\eta| < 2.5$) resides the counterpart to the CPS. This is the Forward Preshower Detector (FPS) [29]. The FPS mounts on the two inner faces of the end calorimeter cyrostats. It utilizes two scintillation planes, with each plane consisting of one u and one v sublayer, see Figure 3.13. The active scintillation layers of the FPS use the same triangular strips as those in the CPS. As with the CPS, clear fibers are connected to the FPS for routing scintillation light from the detector to the platform below to be readout. Readout is done using the same VLPC system as used by the CFT and CPS. In total the FPS contains 16,000

readout channels.

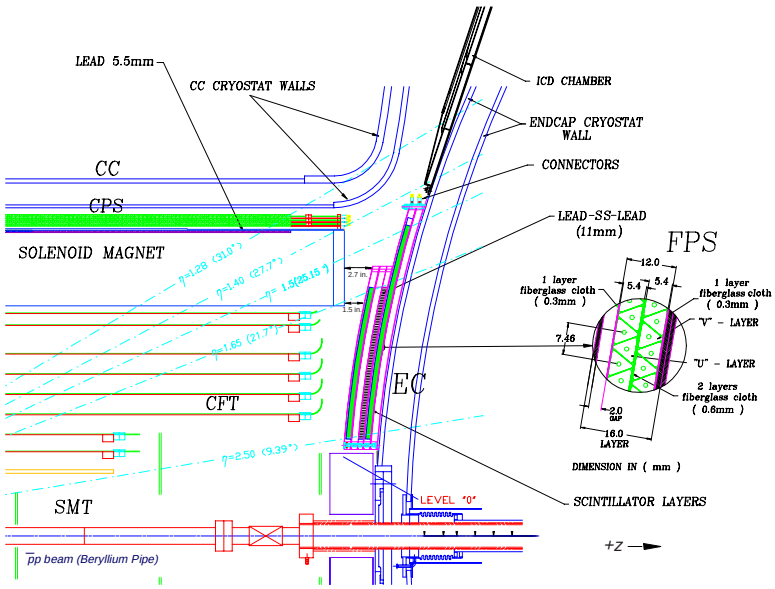

Figure 3.13. One quarter $r - z$ view of the FPS detector. The inset shows details of the $u - v$ scintillator layers. Adapted from [18].

3.4.5 The Calorimeter

The DØ Detector was originally designed with the calorimeter as its centerpiece. While some readout components of the calorimeter have been upgraded for Run II, the calorimeter itself is unchanged from Run I. This calorimeter measures energies of electromagnetic (electrons, photons) and hadronic objects (pions, jets) accurately. The identification of electromagnetic (EM) and hadronic (HD) objects utilizes the different types of showers that these objects create in the calorimeter. EM objects interact primarily with the uranium in the detector via the following two processes: pair production ($\gamma \rightarrow e^+e^-$) and bremsstrahlung ($e \rightarrow e\gamma$). For each successive interaction the number of secondary particles increases while the average energy per particle decreases. It is the collection and measurement of these secondary particles that gives us information on the original EM object's energy (E_0). Because of these

interactions the energy of the original particle is expected to drop exponentially:

$$E(x) = E_0 e^{-x/X_0} \tag{3.5}$$

where E_0 is the particle's original energy, x is the distance traveled, and X_0 is the radiation length of the material being passed through. For uranium X_0 is approximately 3.2 mm [5].

For hadrons the interaction with the detector occurs with the uranium nuclei via the strong nuclear force. These interactions produce secondary particles, about a third of which are neutral pions (π^0) . While the π^0s produce electrons and photons which interact electromagnetic ally, the rest of the secondaries interact strongly. This type of particle shower tends to develop over longer distances and is also larger. The analog of the radiation length for hadronic interactions is the nuclear interaction length (λ_0), which is 10.5 cm for uranium [5].

The DØ calorimeter is a compensating sampling calorimeter, using liquid argon as an active medium and depleted uranium as well as copper and steel as absorber material [30]. To allow access to the central detector regions the calorimeter is contained in three vessels or cryostats. The three modules are the Central Calorimeter (CC) and a pair of end calorimeters, EC North and EC South. The CC covers a region of about $|\eta| \leq 1.2$, while the EC extends detector coverage out to $|\eta| \approx 4.5$. Figure 3.16 shows a schematic cut away view of the DØ Calorimeter and some of its components.

Within the CC and ECs there are three sections. In order of increasing distance from the collision point, these are the electromagnetic section (EM), the fine hadronic section (FH), and the coarse hadronic section (CH). The EM sections consist of four separate layers EM1, EM2, EM3, and EM4. For the CC these EM subsections are layered radially, while for the ECs they are layered in increasing z. Each layer uses 3 mm or 4 mm thick nearly pure depleted uranium plates as an

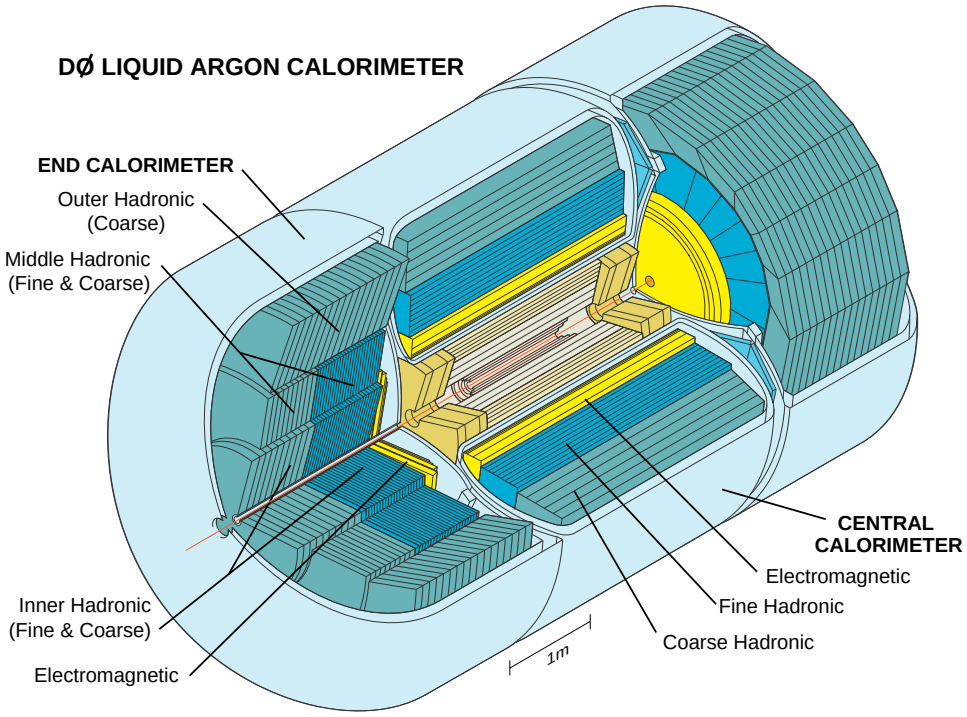

Figure 3.14. Three dimensional cut away view of the DØ calorimeter. Adapted from [18].

absorber. For the FH, each section consists of three or four layers having 6 mm thick uranium-niobium (2 percent) alloy absorber plates. The outer CH section has one layer made of relatively thick (46.5 mm) plates of either copper for the CC or stainless steel for the EC. Table 3.1 shows the depth of each layer for the three calorimeter layers in units of radiation lengths (X_0) and absorption length (λ) [3].

Table 3.1

DEPTH OF THE DIFFERENT CALORIMETER LAYERS

	EM	FH	CH
CC Depth	2, 2, 7, 10 X_0	1.3, 1.0, 0.9 λ	3.2 λ
EC Depth	0.3, 2.6, 7.9, 9.3 X_0	1.2, 1.2, 1.2 λ	3.6 λ

From the readout point of view, each layer represents a discrete set of readout cells. Typically the transverse sizes of a cell are $\Delta\eta = 0.1$ and $\Delta\phi = 2\pi/64 \approx 0.1$. However, the EM3 layer is segmented twice as finely in both η and ϕ to allow for a more precise location of the EM shower centroid. A set of cells, one cell from each layer, aligned along an outward direction constitute a tower. This readout tower geometry is shown in Figure 3.15.

Each readout cell is a combination of several adjacent unit cells. Figure 3.16 shows a schematic view of a typical unit cell. As seen from Figure 3.16, these unit cells have a gap between the adjacent absorber plates that is filled with liquid argon. Charged particles from a shower ionize the liquid argon creating electron-ion pairs. The liberated electrons move and are collected by electrodes due to the strong electric field present in the unit cell. Metal absorbers are used as ground cathodes, while the resistive coat on the readout board serve as the anodes and are held at a voltage of +2.0 to 2.5 kV [3]. The readout board sandwiches a copper pad between

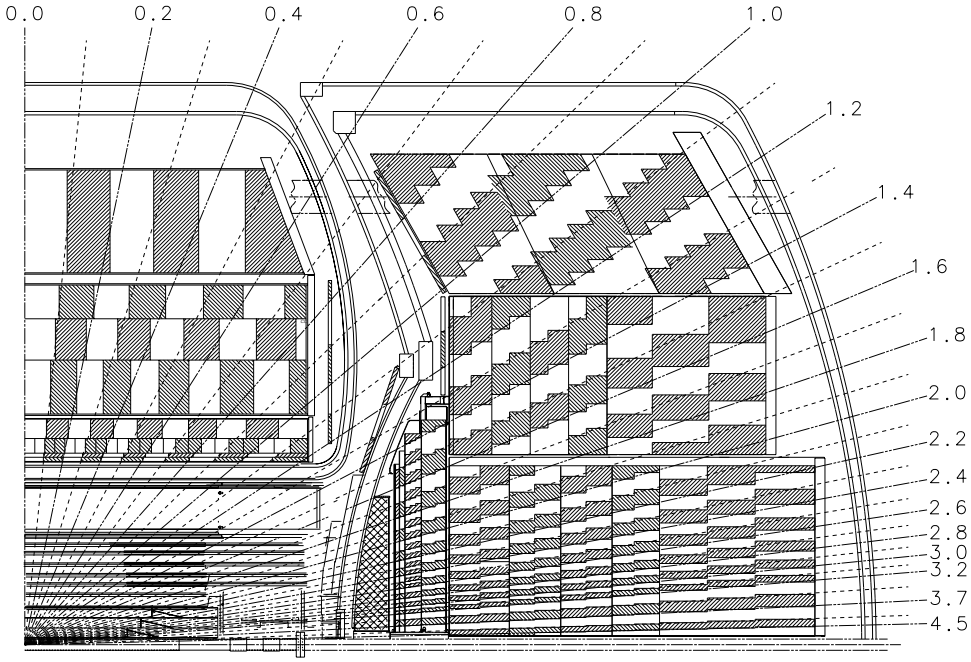

Figure 3.15. A one quarter $r - z$ view of the calorimeter. Lines extending from the center of the detector shows the η coverage of cells and projected towers. Adapted from [18].

two 0.5 mm plates of G10 plastic covered with the resistive epoxy coating. The charge from the electrons deposited on the anode induces a charge on the copper readout pads via capacitive coupling. Electronics receive the analog signal from the readout pad proportional to the energy deposited by the shower in the liquid argon active media. The signals are carried out of the detector via coaxial cables to several electronics boards that reorganize the outputs from the module structure to a physics scheme. This scheme rearranges the readout channels into a pseudo-projective η-ϕ tower arrangement. After this, the signal is sent to preamplifiers and signal shaper electronics and then split and sent down two different paths. One path goes the Level 1 calorimeter trigger. The other path leads to the baseline subtraction system (BLS). The BLS function is to clean and remove noise from the signal before it is sent to be digitized. This is done by using a previous signal that was taken from the previous interaction as a baseline. Subtracting the baseline from the current signal reduces noise caused by long time constants intrinsic in some of the electronics used within the calorimeter. Following a trigger decision, output from the BLS is read out and digitized by Analog-to-Digital Converters (ADC). This digital signal is merged with signals from other detector systems and used to form an event.

3.4.6 Intercryostat and Massless Gap Detectors

Between the CC and EC of the calorimeters, in the region of $1.1 < |\eta| < 1.4$, there is a large amount of uninstrumented material as can be seen in Figure 3.15. Cryostat walls, calorimeter support, and cabling for the detector readout constitute the majority of this material [3]. Scintillation detectors have been mounted on each face of the EC cyrostat walls to help instrument this region. Each intercryostat detector (ICD) is made of 384 scintillating tiles each of size $\Delta\eta = \Delta\phi = 0.1$,

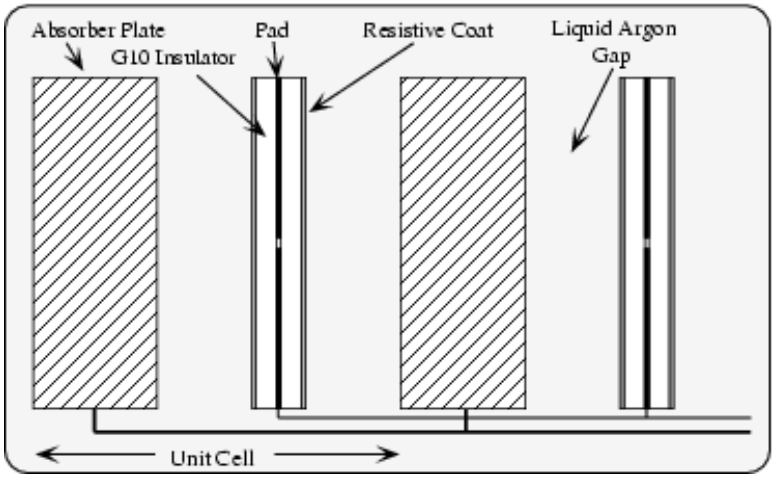

Figure 3.16. Schematic view of a calorimeter cell. Adapted from [18].

which exactly matches the calorimeter cells. Additionally, there are separate single calorimeter-like readout cell structures, called massless gaps, installed in both the EC and CC calorimeters. In combination, the ICD and massless gap detectors provide a good approximation to the standard calorimeter readout, within this special region.

3.4.7 The Muon System

Surrounding the DØ Calorimeter, constituting the outermost and physically largest sub-detector is the DØ Muon System. Muons are about 200 times heavier than electrons and therefore they do not lose as much energy via bremsstrahlung as electrons do. Muon energy loss occurs due to ionization of the detector media, which is a low energy loss absorption process. Therefore, muons above a certain energy threshold ($\sim$3GeV) pass through the entire DØ detector. Because of this property muon systems are typically the outermost sub-detectors in high energy physics experiments. Furthermore, due to its location outside the calorimeter the muon system is well shielded from unwanted debris originating from hadronic or

electromagnetic showers.

The muon system is designed to identify muons and perform an independent measurement of their momenta. There are three major components making up the DØ Muon system [3]. Shown in Figure 3.17 is an illustration of the muon system's three major components. First, there is the Wide Angle MUon Spectrometer (WAMUS) covering a range of $|\eta| < 1$. Second, there is the Forward Angle MUon Spectrometer (FAMUS) covering a range of $1 < |\eta| < 2$. Measuring the muons' momenta is accomplished by the third major component to the muon system. This is a solid iron toroid magnet producing a 1.8 Tesla field. In Run I there was no magnetic field in the central tracking region, subsequently the muon momentum measurement was done using the toroid. Now the muon momentum is predominantly found using the upgraded central tracking system, but the muon system toroid stills allows for an independent measurement. In the future, combining momentum information from the toroid with that from the central tracking systems may further improve the overall momentum measurement for muons at DØ.

The WAMUS consists of three detection layers, increasing radially outward and labeled with the convention: A, B and C [18]. Layer A resides between the calorimeter and the toroid magnet, while the B and C layers are positioned outside the toroid. A combination of proportional drift tube (PDT) chambers and scintillators make up each layer within the WAMUS. The PDT chambers are constructed of extruded aluminum tubes of varying size, with the largest being around 250×575 cm^2. Each chamber consists of three to four decks of tubes, four decks for the A-layer and three decks for the B-layer and C-layer. Tubes are 10.1 cm across and 5.5 cm high, with around twenty-four tubes making up a chamber. Inside each tube is an anode wire at its center which runs the length of the tube. These anode wires are oriented along the magnetic field lines in order to provide a position measurement for momentum

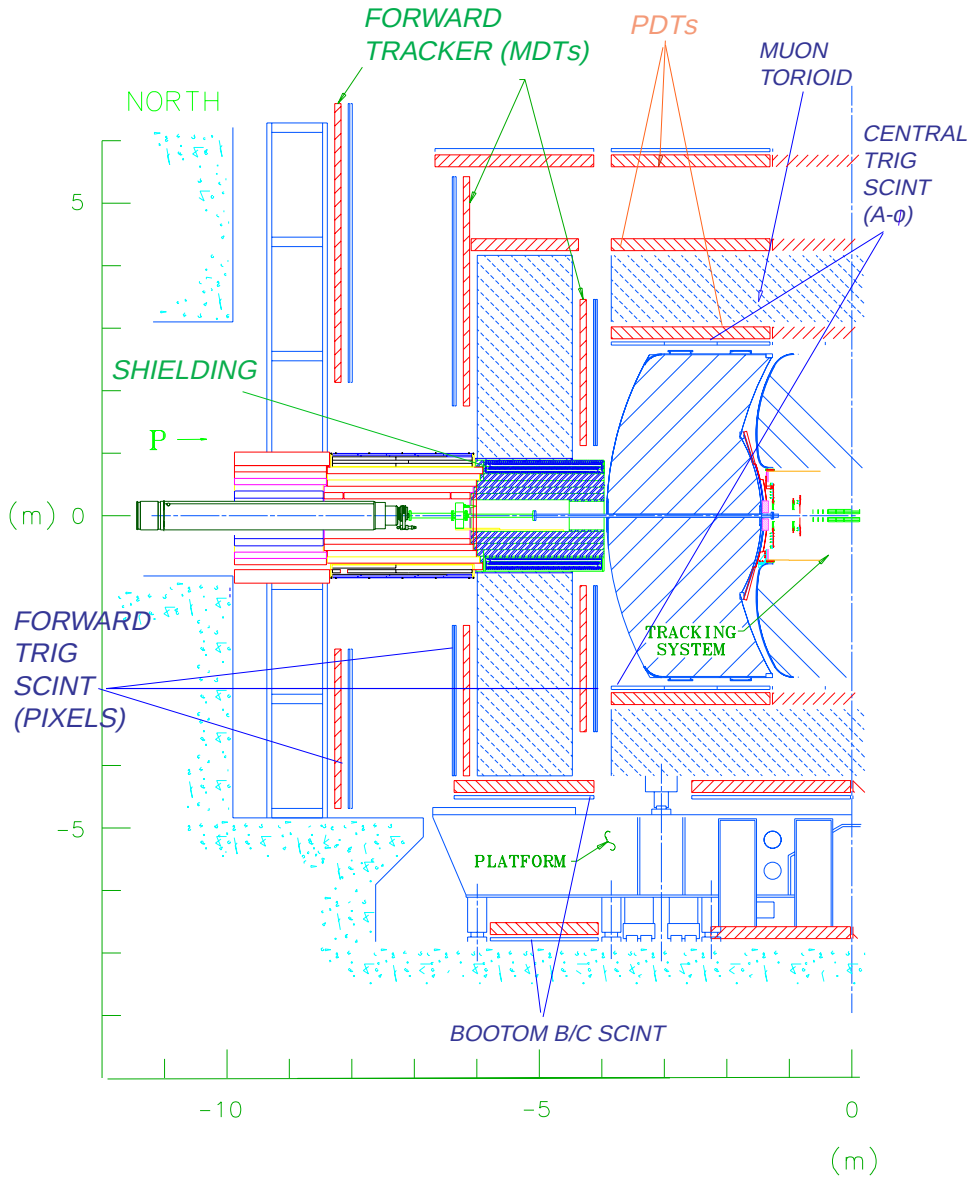

Figure 3.17. A $r - z$ half-view of the Muon System. Components of both the Forward and Wide Angle systems are shown. Adapted from [18].

determination. Besides the wire, two vernier pads, along the top and the bottom of the tube, are used as cathodes. Each tube is filled with a non-flammable gas mixture of 80 percent argon, 10 percent CH_4 and 10 percent CF_4. At the operational voltage of 2.5 kV for the pads and 5.0 kV for the wire, the drift velocity in this gas is about 10 cm/μs, with a maximum drift time of 500 ns [31]. Hit position uncertainty due to diffusion in this gas is around 375 microns.

Scintillators for the WAMUS are broken up into two categories, the A-ϕ counters and the Cosmic Caps. The A-ϕ counters cover the A-layer PDTs. They are segmented in ϕ slices of 4.5 degrees having a length of around 85 cm along the z direction. Each scintillator slice is embedded a wavelength shifting (WLS) fiber coupled to a photo-multiplier tube (PMT), which is used for readout. These scintillators have a timing resolution of $\sim$4 ns [31]. This fast signal is used for triggering and rejecting out-of-time muons from cosmic rays and backscattered particles from the forward regions.

The Cosmic Cap scintillators are located outside the B-layer and C-layer PDTs. This covers the top, sides, and part of the bottom of the muon system. As with the A-ϕ scintillators, the Cosmic Cap scintillators are read out with a WLS and PMT system. Cosmic Cap scintillators' time resolution is $\sim$5 ns, which can be improved by offline corrections to 2.5 ns [31]. This provides a fast signal used to identify cosmic ray muons. Together with the A-ϕ counters, this signal gives a timestamp determining which beam crossing the muon is associated with.

The FAMUS consists of three layers, again called A, B and C. Each layer is made up of a combination of Iarocci mini-drift tube (MDT) sections and scintillation pixel counters. The MDT sections are made up of three to four planes of tubes, four planes for the A-layer and three planes for the B-layer and C-layer. Each plane is divided into eight octants and consist of tubes, each having eight cells. The indi-

vidual cells have an internal cross-sectional area of 9.4×9.4 mm^2 and each contain a 50 μm tungsten-gold anode wire [31]. A gas mixture of 90 percent CF_4 and 10 percent CH_4 is used in the MDT cell. With this mixture of gas and a cathode voltage of 3.1 kV a maximum drift time of near 60 ns is achieved. The position resolution in the drift plane for this configuration is around 0.7 mm. Figure 3.18 shows an $r - \phi$ view of one of the MDT planes.

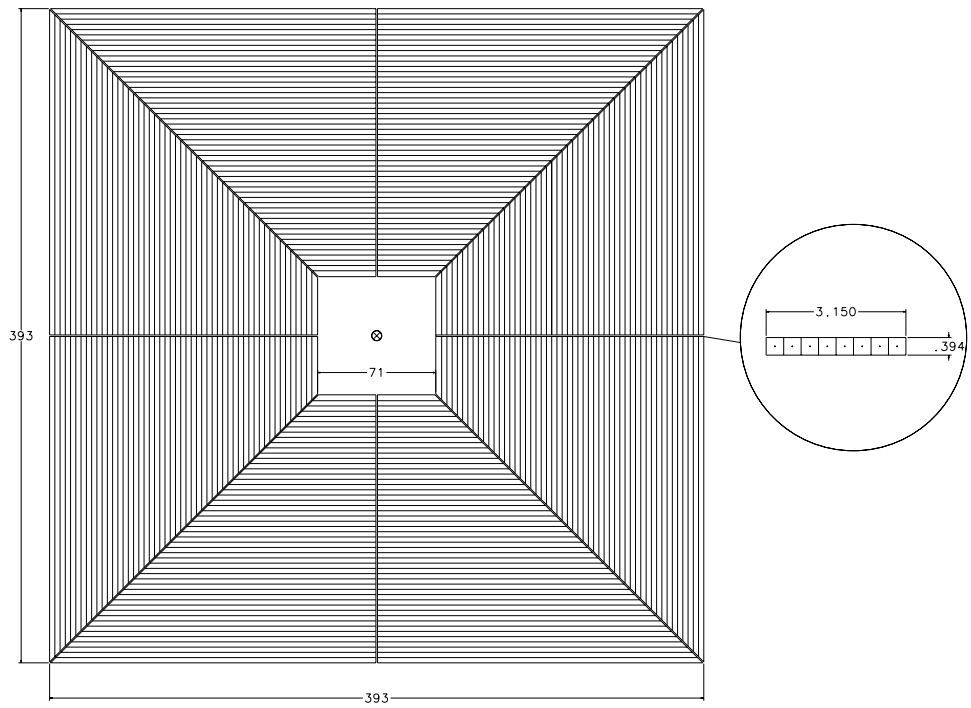

Figure 3.18. Seen here is a $r - \phi$ view of one plane of the muon mini-drift tube. The insert shows the cross section of a single Iarocci tube. Adapted from [18].

Mounted on the face of each of the MDT layers are single planes of scintillator, called the pixel counters. Each plane is divided into eight octants with each octant consisting of ninety-six tiles of scintillator [31]. The pixel counters have a ϕ segmentation of 4.5 degrees with a η segmentation of 0.12 for the outer nine rows and 0.07 for the inner three rows. Figure 3.19 shows an $r - \phi$ view of one of the FAMUS pixel counters. Just as with the WAMUS scintillators, the FAMUS pixel counters

are readout with a WLS and PMT system.

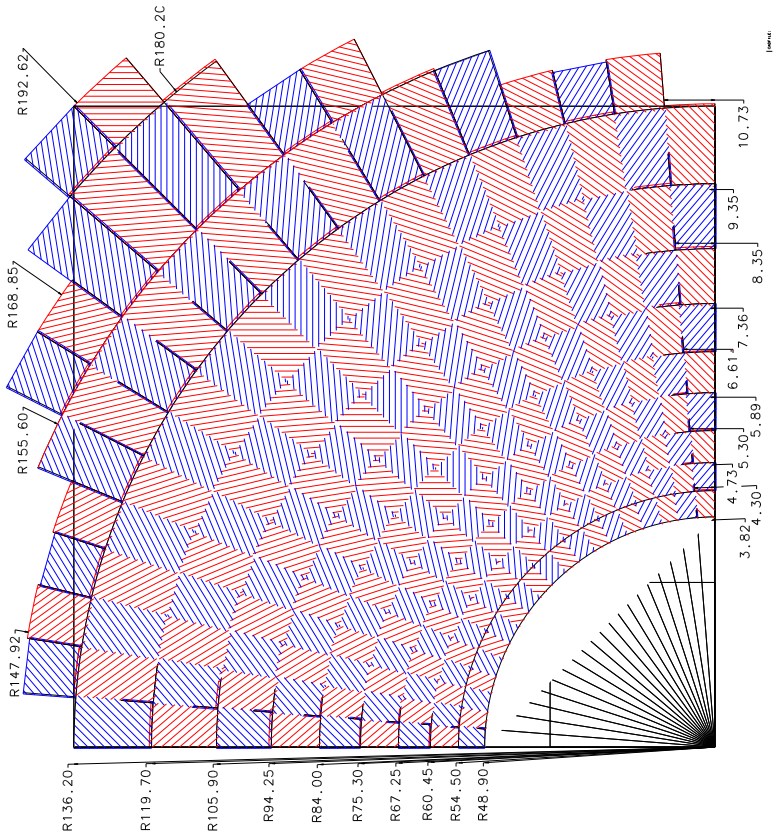

Figure 3.19. An $r - \phi$ view of the segmentation of the FAMUS scintillator pixel counters is shown. Adapted from [18].

The muon system also contains a series of 50 cm thick iron and 15 cm thick polyethylene shielding with 5 cm thick lead skins. This shielding surrounds the accelerator beam pipe in the forward region ($2.5 < |\eta| < 3.6$) behind the EC cryostat wall. The shielding was designed to reduce backgrounds from interactions of the beam with the quadrupole magnets and beam pipe by a factor of two to four [18].

3.4.8 Trigger and Data Acquisition Systems

At a $p\overline{p}$ experiment such as DØ, roughly a few collisions in a million are of physics interest. These are events that might produce a W or Z boson or even top

quark pairs. Furthermore, in searches for some new type of phenomena, the fraction of these events is expected to be even smaller. The bulk of events coming from a $p\overline{p}$ collision at the Tevatron are due to low-p_T non-diffractive $p\overline{p}$ scattering and parton scattering [3]. These processes have been studied in detail in the past and thus make them of little interest at DØ. Along with this, the total collision rates at the Tevatron are far higher than can be processed and recorded. A solution is necessary to pick only the interesting events and discard the rest. The DØ trigger system is a combination of hardware and software elements designed to select the relatively few interesting collisions from a very high-rate background. The trigger decision must be made quickly and according to a specific pattern corresponding to a particular type of event. Typically the characteristics that a trigger uses are based off of some well known physics process. A trigger nonetheless needs to be flexible enough to recognize and accept events that may contain new physics with a high efficiency.

At DØ the trigger is organized into three main levels (L1, L2, and L3). With each progressive trigger level, event selection is done in a increasingly sophisticated manner and has a corresponding decreased output rate. The trigger scheme used by DØ and typical event rates at each stage can be seen in Figure 3.20.

The L1 trigger system is a hardware system based on simple algorithms implemented in Field Programmable Gate Arrays (FPGAs). Raw information from the various detector systems is utilized at this stage. Processing of the detector or group of detector's information is done in parallel at L1, as shown in Figure 3.21.
Also shown in Figure 3.21 is a diagram of the L2 trigger system scheme. The L2 trigger correlates the information from the different sub-detectors and creates physics object candidates such as muons or electrons. In conjunction with creating candidate objects the L2 trigger sends a decision to the L3 trigger system. The L2 system physically consists of 500 MHz Alpha processors residing in VME crates on a

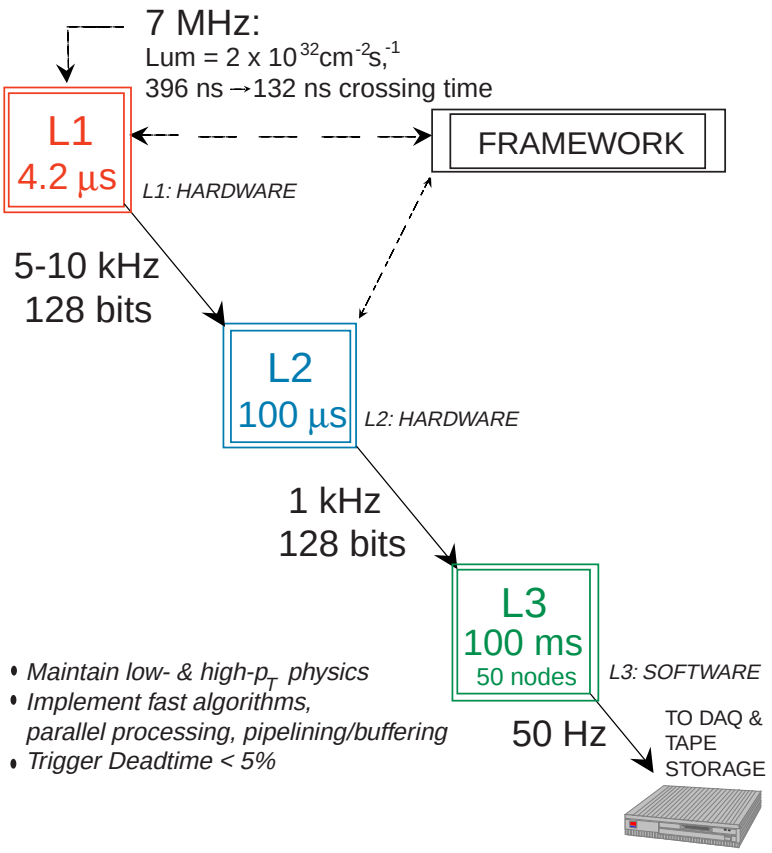

Figure 3.20. The DØ trigger layout and typical trigger rates. Adapted from [18].

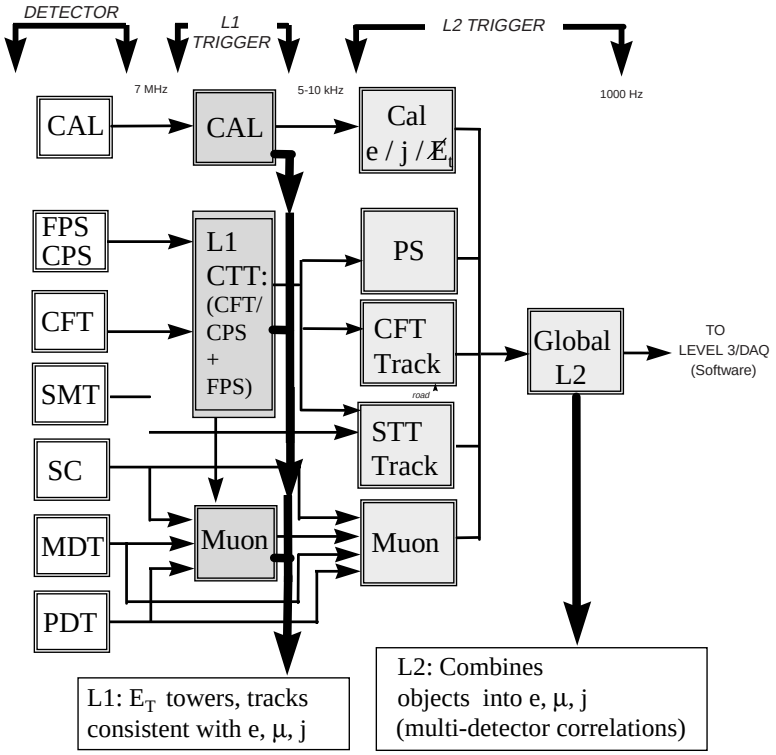

Figure 3.21. Level 1 and Level 2 trigger data flow paths. Adapted from [18].

VME bus, running Linux and using custom built Magic Bus interfaces for 320Mb/s data handling [3].

When the L2 trigger system issues an accept the L3/Data Acquisition System (DAQ) goes into action. At this point information from the various sub-detector readout crates (ROCs) is collected by L3. The L3 system combines and partially reconstructs the data for each event [3]. Software for the L3 system runs on a farm of Linux PC's. An independent copy of the L3 filtering software runs on each PC and separately analyzes each event. A schematic diagram of the L3/DAQ system can be seen in Figure 3.22, here the L2 decision is contained in the the trigger framework (TFW) information.

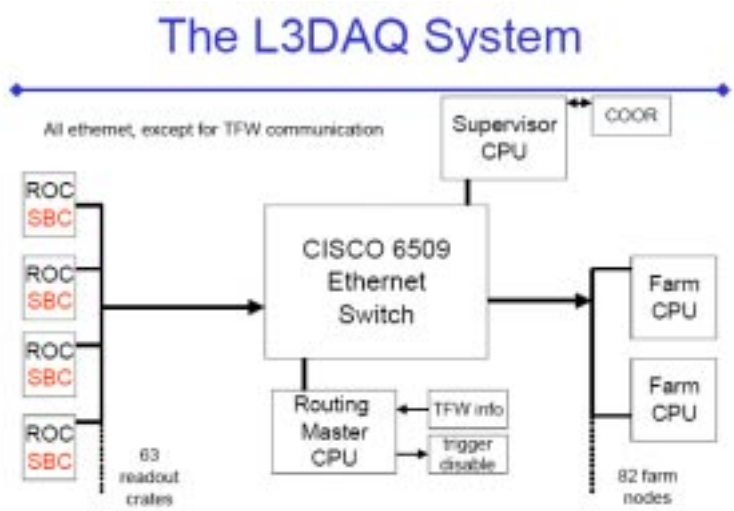

Figure 3.22. The L3 and DAQ system layout. Adapted from [3].

The ROCs in the Figure 3.22 are a set of about 70 VME crates, each of which corresponds to a section of a sub-detector or the trigger framework. Each ROC is read out by a Single Board Computer (SBC), which are powered by 933 Pentium-III processors with 128 MB of RAM. Typical event data sizes are 1-10 kB per

crate. Total event sizes are about 250 kB [3]. Data moves from the SBCs to one of the L3 processors via Ethernet connections. The L3 processors build complete events, reconstruct them, and perform some physics selections, utilizing a series of software filter tools. Each tool has a specific function related to the identification of a certain physics object or event characteristic [5]. There are tools for jets, muons, EM objects, tracks, scalar E_T, $\not\!\!E_T$, as well as other physics objects. If events pass the physics criteria, they are sent through the network to a collection machine and are written to tape for offline analysis.

CHAPTER 4

THE LARGE EXTRA SPATIAL DIMENSIONS ANALYSIS

This chapter details the search for large extra spatial dimensions (LED) in the dimuon channel at DØ using approximately 170 pb^{-1} of Run II data. The collider runs used in this analysis are described as well as the selections made to create a clean, high p_T dimuon data set. Also provided is a description of the Monte Carlo simulation of the LED signal and the dominate Drell-Yan (Z/γ^*) background. No evidence for the existence of LED is found in this analysis. Although the effects of LED are not found, this analysis sets a limit on the fundamental Planck scale M_S which is the best limit to date for the dimuon final state.

4.1 Data Sets and Selections

In the framework of LED, the virtual graviton can couple strongly to fermion pairs. In Run I, DØ pioneered the search for such a LED graviton decaying into the dielectron or diphoton final state. This analysis extends this search by looking at the dimuon final state. The muons from the decaying graviton tends to have high p_T due to the virtual mass of the graviton, and will also be isolated from other particles. With this in mind the following sections describe the steps used to collect a high p_T isolated dimuon data set for this search.

4.1.1 Overview of Muon Identification

This section defines the muon identification criteria for this analysis. Generally the different muon detector systems reconstruct muons from various hits. These hits are grouped together into different numbered segments (*nseg*). The number of the *nseg* comes from that muon system layer the corresponding hits originated from. The sign of *nseg* may either be positive or negative. A positive or zero *nseg* value indicates the muon segments have been matched to a charged particle track reconstructed from the central tracking systems, while a negative *nseg* value indicates there is no central track match. For the remainder of this dissertation the discussion will be restricted to positive *nseg* values. Table 4.1 shows a list of the different possible values of *nseg* and corresponding detector layers.

Table 4.1

DEFINITIONS OF NSEG

nseg	Corresponding Muon System Segments
3	A and BC-layer
2	BC-layer
1	A-layer
0	Any muon system hit

Furthermore, there are three muon quality types currently used at DØ which depend on *nseg* as well as the raw muon system hits. The three muon qualities are *loose*, *medium* and *tight*. Table 4.2 gives a breakdown of the definitions of the different muon qualities [32]. Because *tight* muons are not used in this analysis, details on the *tight* muon criteria are left to the reader [32].

As mentioned above, a positive *nseg* values indicates that a track from the central tracking systems had been matched to the muon segments. This is particularly

Table 4.2

MUON QUALITY DEFINITIONS

	nseg=3
medium	At least two A-layer wire hits A-layer scintillator hit At least two BC-layer wire hits At least one BC-layer scintillator hit
loose	*medium* but allow one of the criteria to fail
	nseg=2
medium	*loose* + located in the bottom part of the detector with $\lvert\eta_d\rvert < 1.6$
loose	At least one BC-layer scintillator hit At least two BC-layer wire hits
	nseg=1
medium	*loose* + located in the bottom part of the detector with $\lvert\eta_d\rvert < 1.6$
loose	At least one A-layer scintillator hit At least two A-layer wire hits

important for this analysis. Because of the high p_T nature of this analysis, all kinematic variables are taken from the muon's matched central track.

4.1.2 Collider Runs and Common Sample Skims

This analysis, based on the Run II collider data, corresponds to runs 151810 through 180957. These runs were taken over the course of the year 2002 and the majority of 2003. Several different versions of the DØ reconstruction (DØ RECO) software was used to reconstruct this data. Specifically, versions p13, p14.03.00, p14.03.01, p14.03.02, p14.05.00, p14.05.02, and p14.06.00 of DØ RECO reconstructed this data. So many different DØ RECO versions present a problem of consistency for any analysis wishing to use data from all of them. This was solved by the DØ Common Sample Group (CSG) which applies fixes to the older versions of the reconstructed data so it is compatible with versions p14.05.02 and p14.06.00 [33].

Once the data sets are fixed, the CSG runs to form smaller topologically specific data sets called skims. The skim used for this thesis is the *2MUhighpt* CSG skim. The requirements for this skim are as follows:

- At least two reconstructed muons of the *loose* quality.
- Both of these *loose* muons must have $p_T > 15$ GeV, as measured from the matched central track.

These skims are stored in the standard DØ format called a *thumbnail*. Using version 00-00-06-a of a package called *d0correct* the *thumbnail* skims create certified physics objects [33]. These objects are stored in a object-oriented container class called a $TMBTree$. The $TMBTrees$ are accessed using standard ROOT libraries and methods [41]. The number of events in the starting $TMBTree$ sample is 70,450. Figure 4.1 shows the run numbers used in this sample.

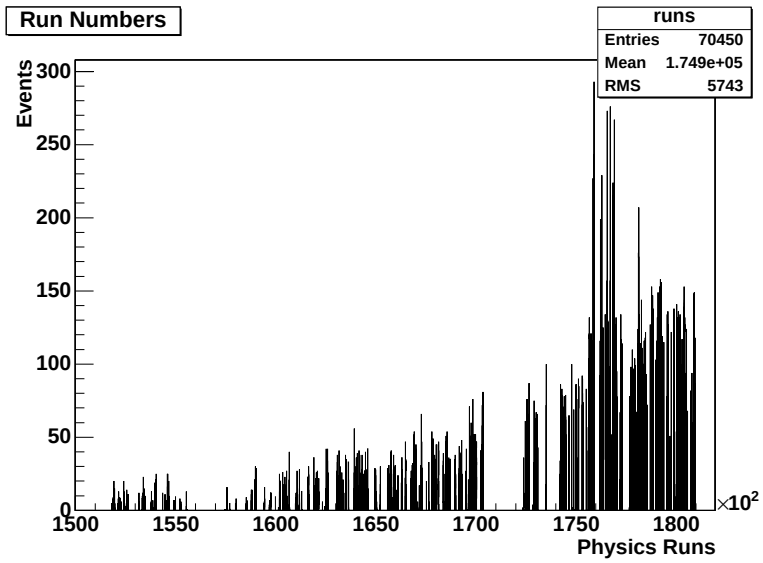

Figure 4.1. The plot shows the run numbers used for this analysis.

4.1.3 Bad Runs, Duplicate Events and Triggers

Bad runs are removed from this sample based on the various sub-detectors used, which include runs marked as bad from the muon system, SMT and CFT. These runs are found by using a bad run list generated by the Offline Run Quality Database. Runs 168618 through 169290 were not used in the analysis due to PDT problems in the muon system. Also, runs in the ranges of 172359-173101 and 174207-174217 are not used due to problems with the dimuon triggers. After bad run removal 64,288 events remain.

A substantial number of duplicate events exist in this sample. These duplicate events were removed and only the instance of the event that was reconstructed with the latest version of DØRECO was kept. For example, if the same event occurred twice in the sample, once reconstructed with p14.03.00 and once reconstructed with p14.05.02, the p14.05.02 instance of the event is kept in the sample. The sample has 61,577 events after duplicate event removal.

For consistency and as a double check of the sample luminosity, the data was required to fire one of the dimuon or single muon triggers described in Tables 4.3-4.4. In the analysis a logical OR was used to allow events to pass if any one of the trigger requirements was met. For this sample the luminosity found for these triggers is 170 ± 11 pb^{-1} [34]. All 61,577 events in the sample fired at least one of the triggers required.

Table 4.3

TRIGGER DESCRIPTIONS AT LEVEL 1

Trigger Name	L1 Region	L1
$2MU_A_L2M0$	$\|\eta_d\| \leq 2$	2 muon scintillators
$2MU_A_L2M0_TRK10$	$\|\eta_d\| \leq 2$	2 muon scintillators
$2MU_A_L2ETAPHI$	$\|\eta_d\| \leq 2$	2 muon scintillators
$2MU_A_L2M0_L3L15$	$\|\eta_d\| \leq 2$	2 muon scintillators
$MUW_W_L2M3_TRK10$	$\|\eta_d\| \leq 1.6$	1 muon scintillator and 1 muon wire
$MUW_W_L2M5_TRK10$	$\|\eta_d\| \leq 1.6$	1 muon scintillator and 1 muon wire

4.1.4 Selection Cuts

Muons originating from a LED graviton signal tend to have high p_T, therefore it is important to make a reliable momentum measurement. Using quality cuts on the muon's matched central track provides an improved measurement. The improvement is achieved because the track quality selections require a minimum number of tracking hits as well as one hit in the SMT system, which has very good hit resolution.

The quality cuts used for the muon's matched track in this analysis are at least one hit in the SMT and at least nine hits in the CFT. Figure 4.2 shows the distribution of tracking hits for all muon tracks in this sample along with the quality cuts

Table 4.4

TRIGGER DESCRIPTIONS AT LEVEL 2 AND 3

Trigger Name	L2
$2MU_A_L2M0$	At least one *medium* muon
$2MU_A_L2M0_TRK10$	At least one *medium* muon
$2MU_A_L2ETAPHI$	2 muons at least one must be *medium* and the muons must be separated by $\Delta\phi > 6$ and $\Delta\eta > 3$
$2MU_A_L2M0_L3L15$	At least one *medium* muon
$MUW_W_L2M3_TRK10$	*medium* with $p_T > 3$ GeV
$MUW_W_L2M5_TRK10$	*medium* with $p_T > 5$ GeV
	L3
$2MU_A_L2M0$	none
$2MU_A_L2M0_TRK10$	Event must have a central track with $p_T > 10$ GeV
$2MU_A_L2ETAPHI$	None
$2MU_A_L2M0_L3L15$	At least one *loose* muon with $p_T > 15$ GeV
$MUW_W_L2M3_TRK10$	Event must have a central track of $p_T > 10$ GeV
$MUW_W_L2M5_TRK10$	Event must have a central track of $p_T > 10$ GeV

used. The invariant mass distribution for events eliminated by the track quality cuts is also shown in Figure 4.2. There are 38,246 events passing this quality selection. Furthermore, at this stage only events reconstructing with a dimuon invariant mass greater than 50 GeV are kept in the sample. This leaves 23,503 events.

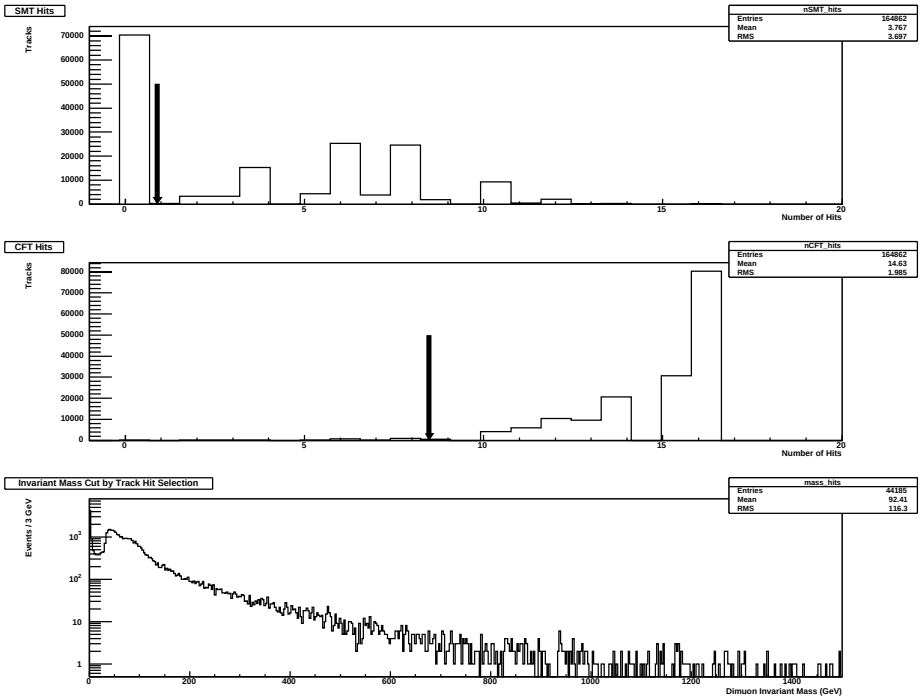

Figure 4.2. The top two plots are of the SMT and CFT hit distributions for tracks from muons in the data set. The arrows indicate where the selection cuts are placed. The bottom plot shows the dimuon invariant mass distribution of those events cut by this selection.

Because the final state for this analysis is two high p_T muons, a major issue to be addressed is the presence of muons from cosmic rays. Cosmic rays interacting with the Earth's atmosphere produce large amounts of high energy pions which subsequently decay into muons. Because of the muon's relatively long lifetime, they tend to reach the Earth's surface before decaying themselves. A cosmic ray muon can pass through the DØ detector, and if it passes close enough to the interaction region

and is within trigger timing gates it can be reconstructed as a dimuon event. While this region is relatively small, the cosmic ray muon production process is continual. Therefore, it is expected some cosmic ray muons will be in the dimuon sample.

The scintillator counters in the muon system allow for a very precise time measurement of interacting muons. These counters are calibrated such that muons originating from $p\overline{p}$ collisions will arrive with time $t = 0$. The top and bottom A-layer muon scintillators are separated by 6m, therefore a muon from a cosmic ray will take 20 ns to travel this distance. Because of this, looking for scintillator times that are significantly different from zero is a useful tool to eliminate cosmic ray muons.

At this point a selection on the muon scintillator times is made. This selection uses the standard cosmic timing cut based off of the muon system's A and BC-layers scintillators as prescribed by the DØ Muon ID group [32]. This cut rejects any event that has a muon with A or BC scintillator times of $|t| > 10$ ns. Figure 4.3 shows the A plus BC scintillator times for this samples as well as the invariant mass distribution for the events rejected by this selection. The number of events passing this selection is 15,885.

As discussed above, timing cuts on the scintillator layers of the muon system are used to remove muons coming from cosmic ray showers. While this timing requirement is effective it does not cut all muons from cosmic rays. This is due to the fact that *loose* muons can miss one or more scintillator hits and thus the timing information is lost. Specifically, the time for such a missed hit is defaulted to zero. Of course this is within the timing window that should cut muons from cosmic rays. To keep *loose* muons, but eliminate the cosmic ray backgrounds a *tight cosmic* cut was placed around zero in the $\eta_1 + \eta_2$ distribution of the two muons.

Dimuon events that originate from cosmic rays tend to back-to-back in η. This

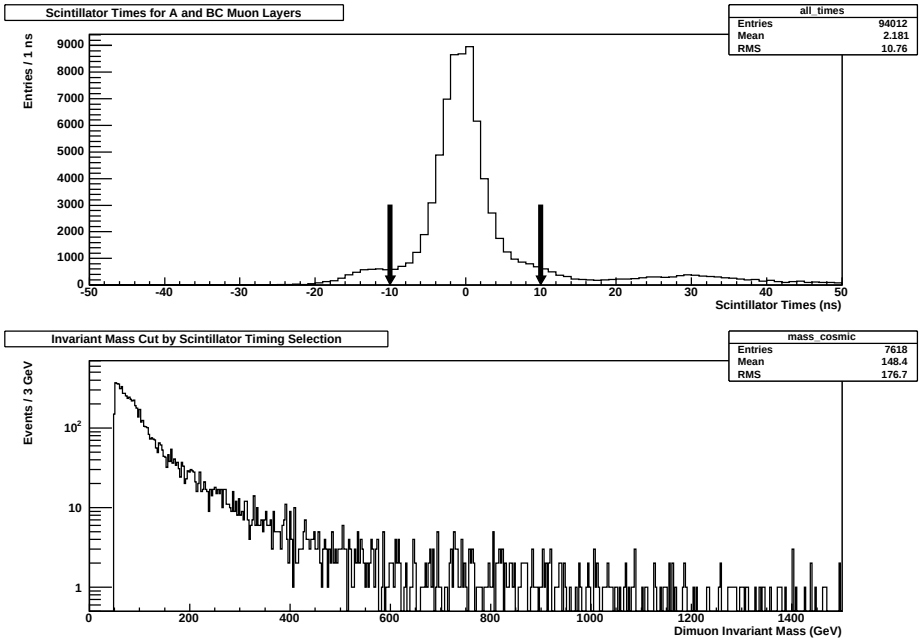

Figure 4.3. The top plot is of the A and BC layer scintillation time distributions for this data set. The arrows indicate where the selection cut is placed. The bottom plot shows the dimuon invariant mass distribution of those events cut by this selection.

is because it is the same cosmic ray muon which is reconstructed twice in the event, once while entering the detector region and again when it leaves. Therefore, it is expected that dimuon events from cosmic ray muons should have $\eta_1 + \eta_2 = 0$. Figure 4.4 shows the $\eta_1 + \eta_2$ distribution for the dimuon events that fail the cosmic timing cuts and as expected they tend to peak at zero. In real dimuon events originating from $p\overline{p}$ collisions the two muons usually do not have this back-to-back η property due to boosts in the z direction as discussed in Chapter 3.

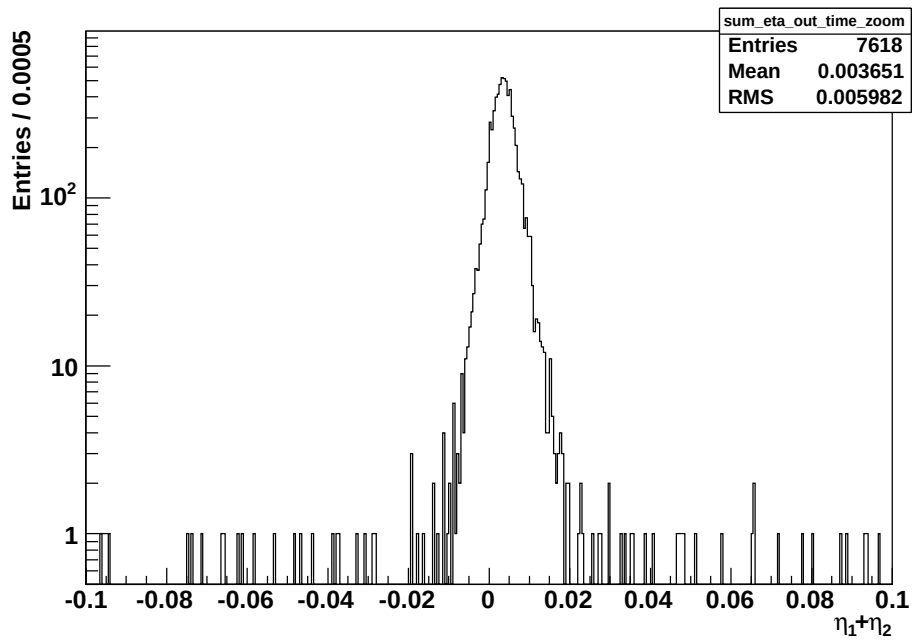

Figure 4.4. The plot is of the $\eta_1 + \eta_2$ distribution for out-of-time dimuon events.

The *tight cosmic* cut is determined by fitting the peak in the sum of the two muon's η distribution shown in Figure 4.5 to a Gaussian plus flat background and calculating a 5σ cut around the mean of the peak. The 5σ window was chosen to ensure virtually all cosmic ray muons are eliminated and can be safely ignored. This selection corresponds to cutting out the region $\eta_1 + \eta_2 < 0.0175$ and $\eta_1 + \eta_2 >$ -0.0102. As illustrated in Figures 4.4 and 4.5 this selection is effective in rejection

of the remaining muons from cosmic rays [35]. After the *tight muon* selection the sample contains 15,383 events.

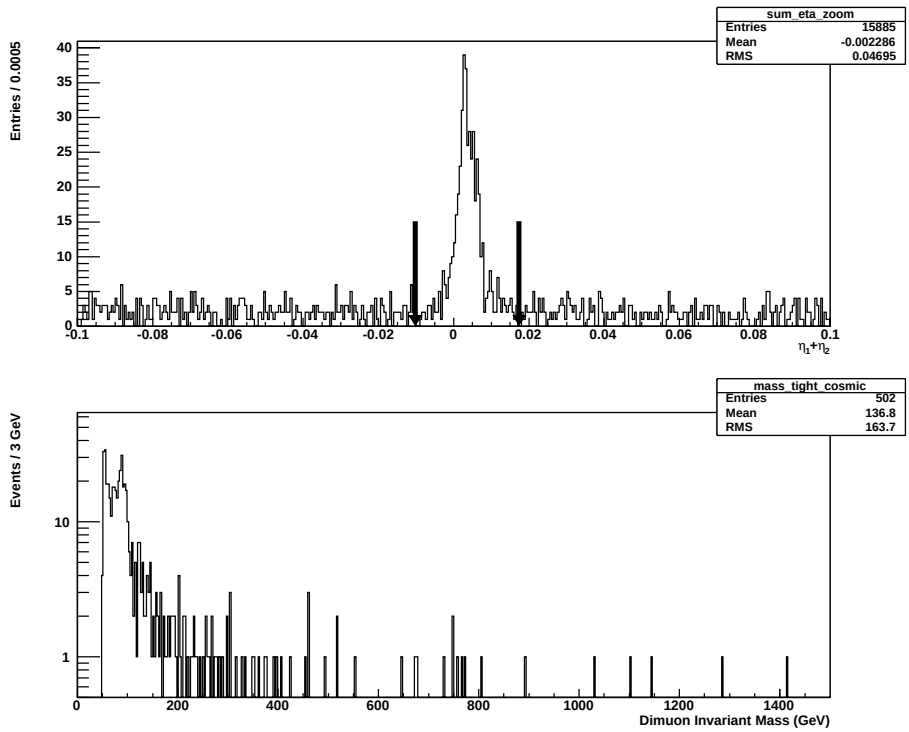

Figure 4.5. The top plot is of the muon's $\eta_1 + \eta_2$ distribution for the data set. The arrows indicate where the selection cuts are placed. The bottom plot shows the dimuon invariant mass distribution of those events cut by this selection.

It is expected that muons from the decay of a LED graviton will be isolated. This means that there will not be any other particles around the muon, such as jets or other objects. Furthermore, decays of heavy quarks can produce relatively high p_T muons which are less likely to be isolated. To help eliminate this background, the muons in this sample are required to be isolated. To be isolated a muon in this sample must pass both of the following criteria:

- Must have $\sum_{cone0.5}(p_T) < 2.5$ GeV, where $\sum_{cone0.5}(p_T)$ is the sum of the p_T of tracks contained within a cone around the muon of radius $R = 0.5$. This will be referred to as the track halo.

- Also must have $\sum_{calhalo}(E_T) = \sum_{cone0.4}(E_T) - \sum_{cone0.1}(E_T) < 2.5$ GeV, where $\sum_{cone0.4}(E_T)$ and $\sum_{cone0.1}(E_T)$ are the sums of the E_T in calorimeter clusters within cones around the muon of radii $R = 0.4$ and $R = 0.1$, respectively. This part of the isolation selection will be referred to as the calorimeter halo.

A cone of radius R is defined in $\eta \times \phi$ space by $R = \sqrt{\eta^2 + \phi^2}$. Both muons are required to pass the isolation selections. Figures 4.6-4.7 show the calorimeter halo and track halo distributions and where the selection cut is placed. Also in the figures are the invariant mass distributions for the events cut by the isolation requirements. After both of the isolation cuts the sample contains 10,532 events. Further details of the isolation strategy can be found in the following reference and are left to the reader [36].

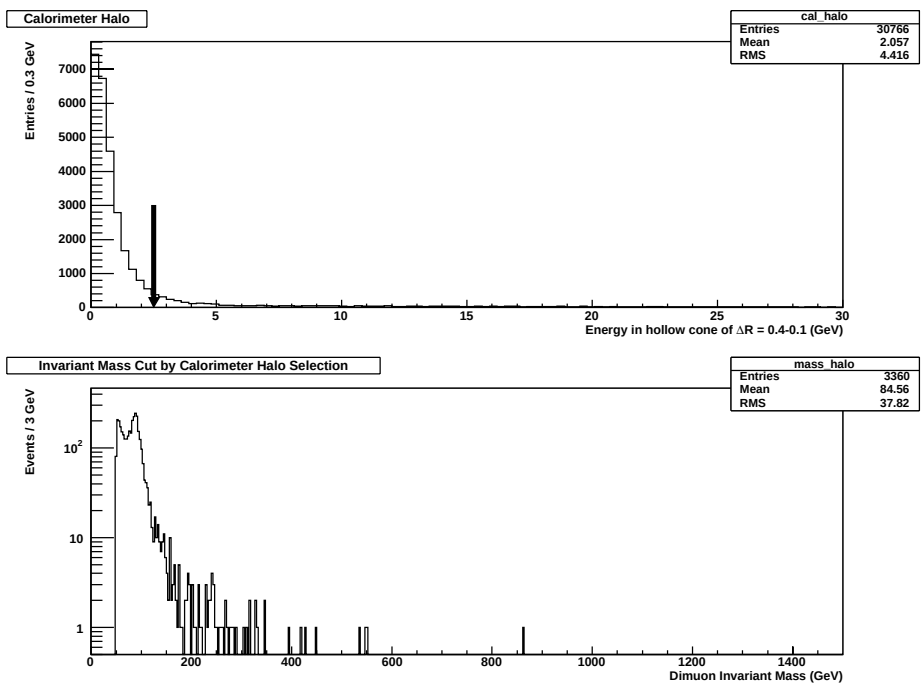

Figure 4.6. The top plot is of the calorimeter halo distribution for the data set. The arrow indicates where the selection cut is placed. The bottom plot shows the dimuon invariant mass distribution of those events cut by this selection.

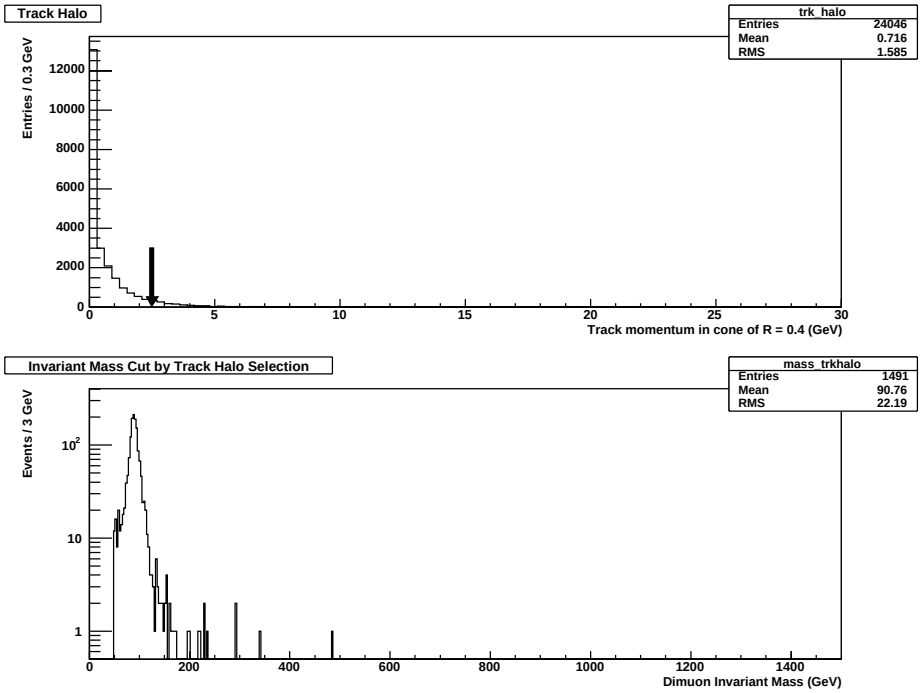

Figure 4.7. The top plot is of the track halo distribution for the data set. The arrow indicates where the selection cut is placed. The bottom plot shows the dimuon invariant mass distribution of those events cut by this selection.

To check if the tracking or isolation selections depend on the p_T of the reconstructed muon, full p14 DØRECO Monte Carlo using Z/γ^* events is studied. Figure 4.8 shows the distributions of muon central track χ^2/dof, calorimeter halo energy and track halo energy versus the p_T of the muon. The central track χ^2/dof is an indication of the quality of the reconstructed tracks. The track χ^2/dof is shown to indicate any variation on the tracking efficiency versus p_T. As can be seen from the plots there is not any pronounced correlation with the p_T of the muon. Although no p_T dependence is seen, a 5% systematic error is assigned to account for any residual p_T dependence due to differences between data and the Monte Carlo used. This error is consistent with studies done by the Muon ID group and is included in the calculation of limits for this analysis [32].

As will be discussed in the MC section of this thesis, events with unphysical energies are cut from this analysis. This constitutes eight events from the data sample. No further cuts, such as on jets or $\not\!\!E_T$, are used in this analysis. Efficiencies for reconstructing *loose*, track matched muons are incorporated into the MC as acceptance maps and will be discussed in the MC section of this text. The *tight cosmic* cut is also incorporated in the MC. Other efficiencies are assumed to not have any geometric or kinematic dependencies and are thus taken care of by the normalization of the MC to the data Z-peak. More on how the MC is normalized to the data will be discussed in subsequent sections. After all the selections the final data sample contains 10,524 events.

4.1.5 Final Data Sample

The final dimuon data sample used in this analysis contains 10,524 events. Since the exchanged graviton from a LED signal is neutral, the decay muons should have opposite signs. While this is true, for this analysis no selection on the charge of

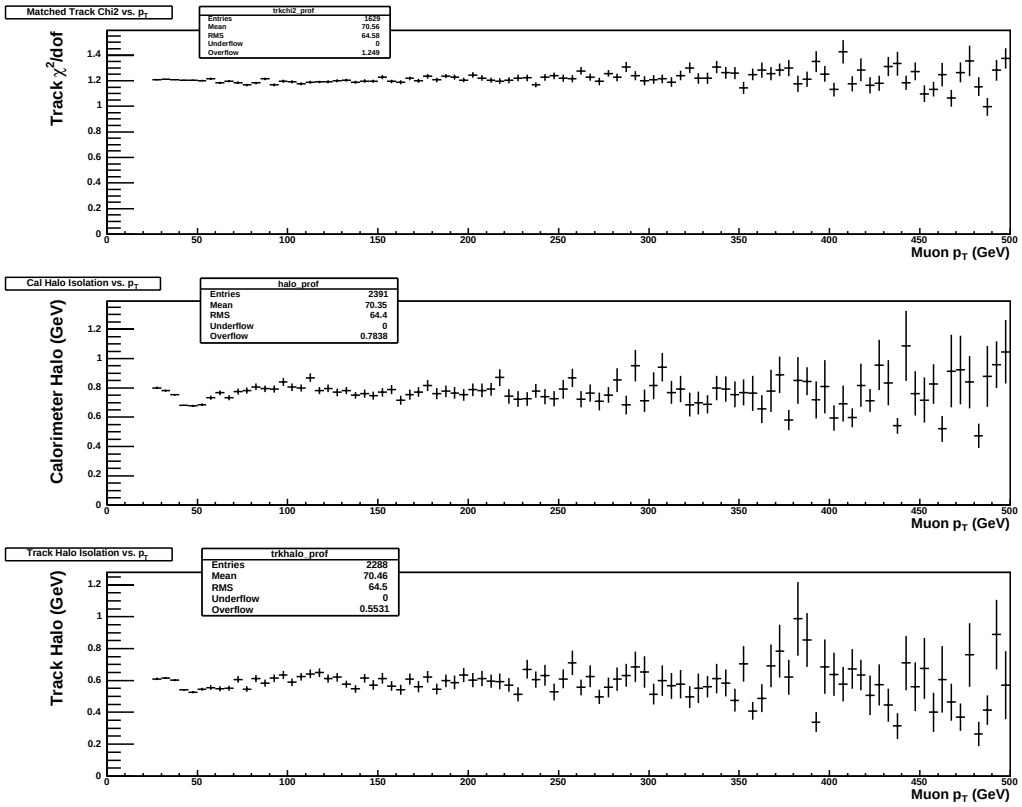

Figure 4.8. The matched central track χ^2/dof (top), calorimeter halo isolation (middle) and track halo isolation (bottom) distributions as a function of muon p_T from full p14 Monte Carlo.

the muons is made. As long as the number of same sign dimuon events is relatively small this should give a more conservative sample. If the number of same sign events is high this would indicate a background or other issue not adequately addressed. For completeness, there are only 17 like sign dimuon events in our final sample of 10,524. Table 4.5 gives an overview of the number of events passing each selection cut used in this analysis. Figure 4.9 shows the invariant mass distribution for the final data set corresponding to an integrated luminosity of 170 ± 11 pb^{-1}.

Table 4.5

EVENT SELECTION

Selection	Number of events passing cut
Starting $TMBTree$ sample	70,450
Bad run removal	64,288
Duplicate events removed	61,577
Dimuon or single muon triggers fired	61,577
SMT hits > 0 and CFT hits > 8 per track	38,246
Dimuon invariant mass > 50 GeV	23,503
Standard timing cosmic veto	15,885
Tight cosmic cut	15,383
Calorimeter Halo < 2.5 GeV	12,023
Track Halo < 2.5 GeV	10,532
Unphysical energy cut	10,524

4.2 The Fast Monte Carlo

The effects of LED via a parton-level leading-order (LO) Monte Carlo (MC) generator augmented with a parametric simulation of the DØ detector is used in this analysis [37]. The MC includes SM contributions (Z/γ^*), Kaluza-Klein graviton exchange diagrams, and their interference in dimuon production. The simulation takes into account detector acceptance, efficiencies, and resolution for the muons,

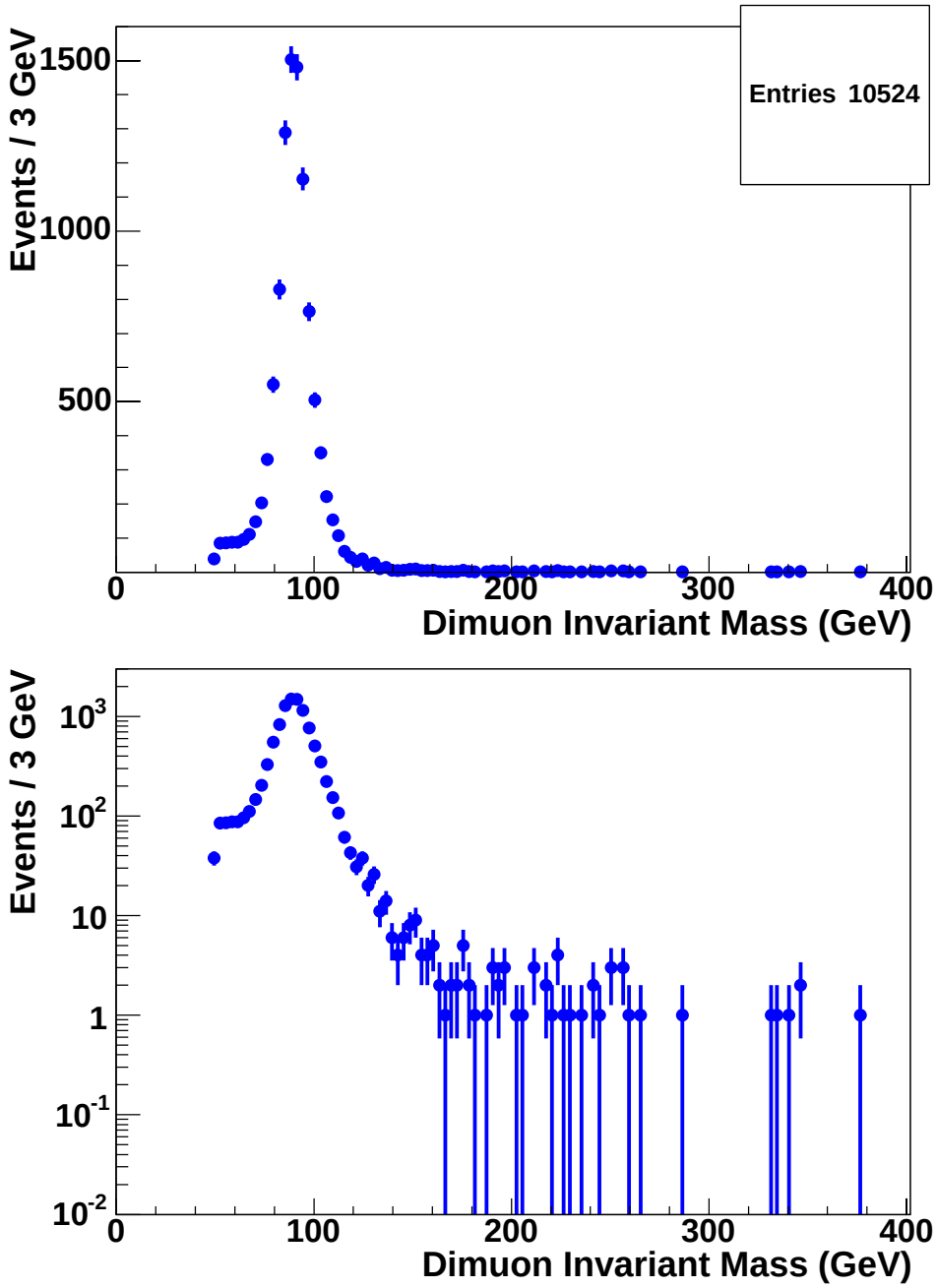

Figure 4.9. Invariant mass distribution for the final data set. Shown in both linear and semi-log scales.

initial state radiation, and the effect of different parton distributions. The parton distribution function (p.d.f.) set currently used is leading order CTEQ4L, which is used for the nominal prediction [38]. The parameters of the detector simulation are tuned using Z events with masses less than 120 GeV. This is to ensure the tuning is done on well understood backgrounds and not on potential signal.

When this analysis was first started, the MC did not contain parameterizations for using muons. Therefore many additions and changes were made to include a simulation of muons in the DØ detector. The following sections describe the changes made to the MC for this dimuon analysis.

4.2.1 Acceptances

The MC utilizes muon identification acceptance maps when generating the background and signal samples. Acceptances used in the MC are externally generated using full p14 DØ MC simulation and reconstruction. The full p14 MC sample used is a sample of Z/γ^* events with invariant masses greater than 60 GeV. To get the efficiency, the $\Delta R = \sqrt{(\Delta\phi)^2 + (\Delta\eta)^2}$ between the reconstructed muon and generator level muon is examined. Figure 4.10 shows the $\Delta\phi$, $\Delta\eta$, and ΔR distributions for the full MC sample. The reconstructed muon is declared matched to the generated muon for $\Delta R < 0.05$. A two-dimensional histogram is filled with the η, ϕ for the generated muons as well as for the matched reconstructed muons. Therefore, the acceptance is found by dividing the reconstructed histogram by the generator level. The results are then output to a acceptance map text file, which contains the efficiency for reconstructing a muon for any given η, ϕ. Figure 4.11 shows the two-dimensional distribution of the acceptance versus η and ϕ. Note the hole in acceptance in Figure 4.11. This is due to uninstrumented sections at the bottom of the muon system. The reconstructed muons used to find the acceptance are required

to be *loose*, central track matched, and the tracks have the same SMT and CFT hit selections as the data sample used for this analysis.

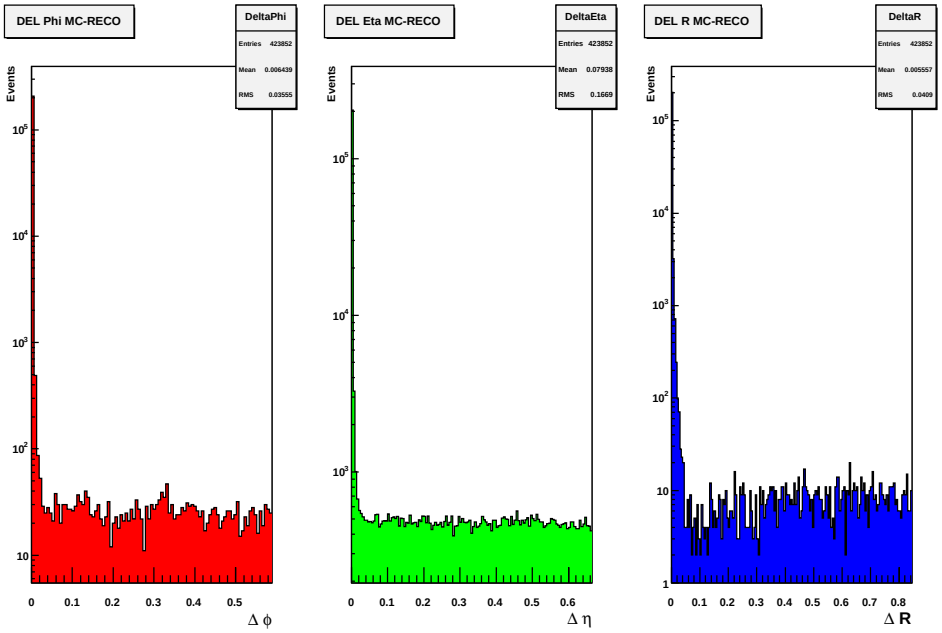

Figure 4.10. Plots of $\Delta\phi$, $\Delta\eta$, and ΔR between reconstructed and generated muons from the full p14 Drell-Yan MC sample. The horizontal axis for these plots is zoomed in near zero to accentuate the peak there.

The acceptance map text file containing the information from the full MC is used as a lookup table for the fast MC for this analysis. In the process of checking the agreement between Standard Model MC and the data, it is apparent that the acceptances in the $|\eta_d| > 1.6$ region do not describe the data well. To address this, corrections to the acceptance map are calculated. Corrections are found by first taking the two-dimensional η, ϕ distributions generated from the fast MC and area normalizing it to the two-dimensional η, ϕ histogram from data. The correction

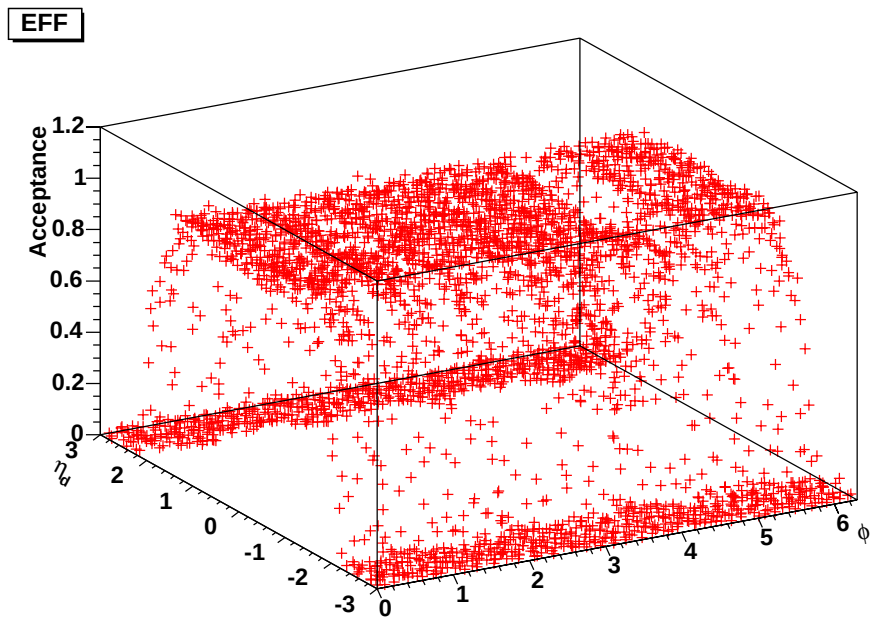

Figure 4.11. The two-dimensional acceptance plot used to create the acceptance map file.

factors are then defined as:

$$Correction = \frac{N_{MC}}{N_{Data}} \tag{4.1}$$

for each η, ϕ bin. Then the correction factor is multiplied by the original efficiency from the acceptance map file and a new corrected acceptance map file is created. It is this corrected acceptance map file that is used for all the final MC generation in this analysis. Only data with invariant mass less than 120 GeV was used to find the acceptance map corrections. This was done to ensure there is no signal contamination in the corrections to the Standard Model MC maps. Figure 4.12 shows a comparison between the η, ϕ distributions using the original acceptance map, the corrected map, and data. Both the MC plots are separately normalized to the Z data so the shapes can be easily compared.

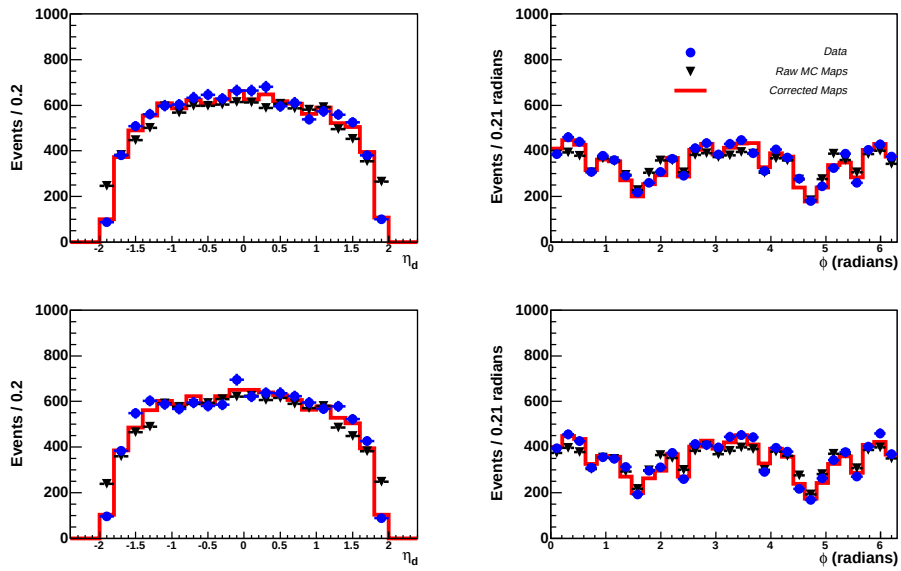

Figure 4.12. Comparisons of the muon's η, ϕ using the original acceptance map, the corrected map, and data. The top plots are for the muon with the highest p_T and the bottom plots are for the other muon.

4.2.2 Momentum Smearing

In this MC momentum smearing at the generator level uses a resolution function of the form:

$$\sigma\left(1/p\right) = \frac{\sqrt{\left(S\sqrt{cosh(\eta)}\right)^2 + (Cp)^2}}{p},$$

where S accounts for multiple scattering and C accounts for the physical position resolutions of the detectors. The hyperbolic cosine term accounts for more material the muons must pass through at higher η. For an ideal DØ detector the term S should have a value of 0.0136, but in reality this needs to be scaled by a factor of 1.072 to account for changes in materials used to construct the tracking system [25]. The term C in the smearing is also scaled up, from an ideal value (C_0) of 0.00162, by a factor of 1.1 [25]. This is due to misalignments that exist in the real detector as opposed to the ideal simulation. Furthermore, due to variations in the tracking

systems magnetic field an overall momentum scale factor ($Scale$) is also needed to get the best description of the real detector.

The parameterization for the proper momentum smearing is found by generating several MC samples with different smearing and scaling correction factors, SF and $Scale$ respectively. The parameters in the MC momentum smearing which are tuned in this analysis are illustrated in the following equations:

$$C = C_0 \times SF$$

$$\text{p(final)} = Scale \times \text{ p(smeared)}.$$

For this analysis it is assumed the multiple scattering term S in the momentum resolution is negligible for high p_T muons such as the ones under study. Therefore, only the C term in the momentum resolution is tuned in this study.

With the generation of several different MC samples a comparison to data around the Z mass peak (70 GeV $< M_{\mu\mu} <$ 120 GeV) is performed. Data and MC agreement is tested by using the $KolmogorovTest$ routine found in the ROOT analysis package [41]. The $KolmogorovTest$ routine is a statistical test of compatibility in shape between two histograms. Therefore, a $KolmogorovTest$ (KS) result near one indicates that the two histograms are very similar, while results near zero indicate incompatible shapes.

Figures 4.13-4.14 show the comparison around the Z-peak mass for various values of the SF and $Scale$ factors. As seen from Figure 4.15 the best agreement between the data and MC is when the term C_0 is scaled by a factor of $SF = 1.1$ and the smeared momentum is scaled by $Scale = 0.985$. A summary of the final smearing and scaling parameters used is:

$$S = 0.01458$$

$$C = 0.00178$$

$$Scale = 0.985.$$

Since the tracker momentum resolution is Gaussian in 1/p, not p, the dimuon momentum has a tendency to be too large. Thus, the dimuon system often appears more boosted than it actually is. This can even result in boosts and energies that are non-physical (i.e. $p_z > 980$ GeV and $E_{\mu 1} + E_{\mu 2} > 1.96$ TeV). This boost is important in the calculation of the scattering angles of the dimuons in their center of mass frame. Therefore, if boost values are very large the corresponding values of $|cos(\theta^*)|$ will tend to be at the upper physical boundary of one. In this analysis the problem is corrected by cutting out events that have unphysical energies. Unphysical events are defined here as, $p_T > 1000$ GeV, $E > 980$ GeV or $E_{\mu 1} + E_{\mu 2} > 1.96$ TeV. This selection is done for both MC and data. In the data sample this results in eliminating eight events out of 10,532, a 0.08% effect. In the MC sample the unphysical energy cut results in cutting 0.04% of SM events.

4.2.3 Dimuon p_T

The MC also includes the transverse momentum of the dimuon system. This is included to help model next-to-leading order (NLO) effects. The parameter $\cos(\theta^*)$ is particularly sensitive to the transverse momentum of the dimuon system [10]. An illustration of this is given in Figure 4.16, which shows how the angle θ^* is effected by transverse boosts of the dimuon system. Typically θ^* is defined as the angle of one of the final state particles with respect to the direction of the parton from the proton beam, as seen in part A of Figure 4.16. But because of NLO effects we define θ^* relative to the final state particle emitted along the direction of the boost. Part B of Figure 4.16 helps to illustrate this point. This definition of θ^* is used in both the MC and data.

The parameterization for the transverse momentum of the dimuon system is also

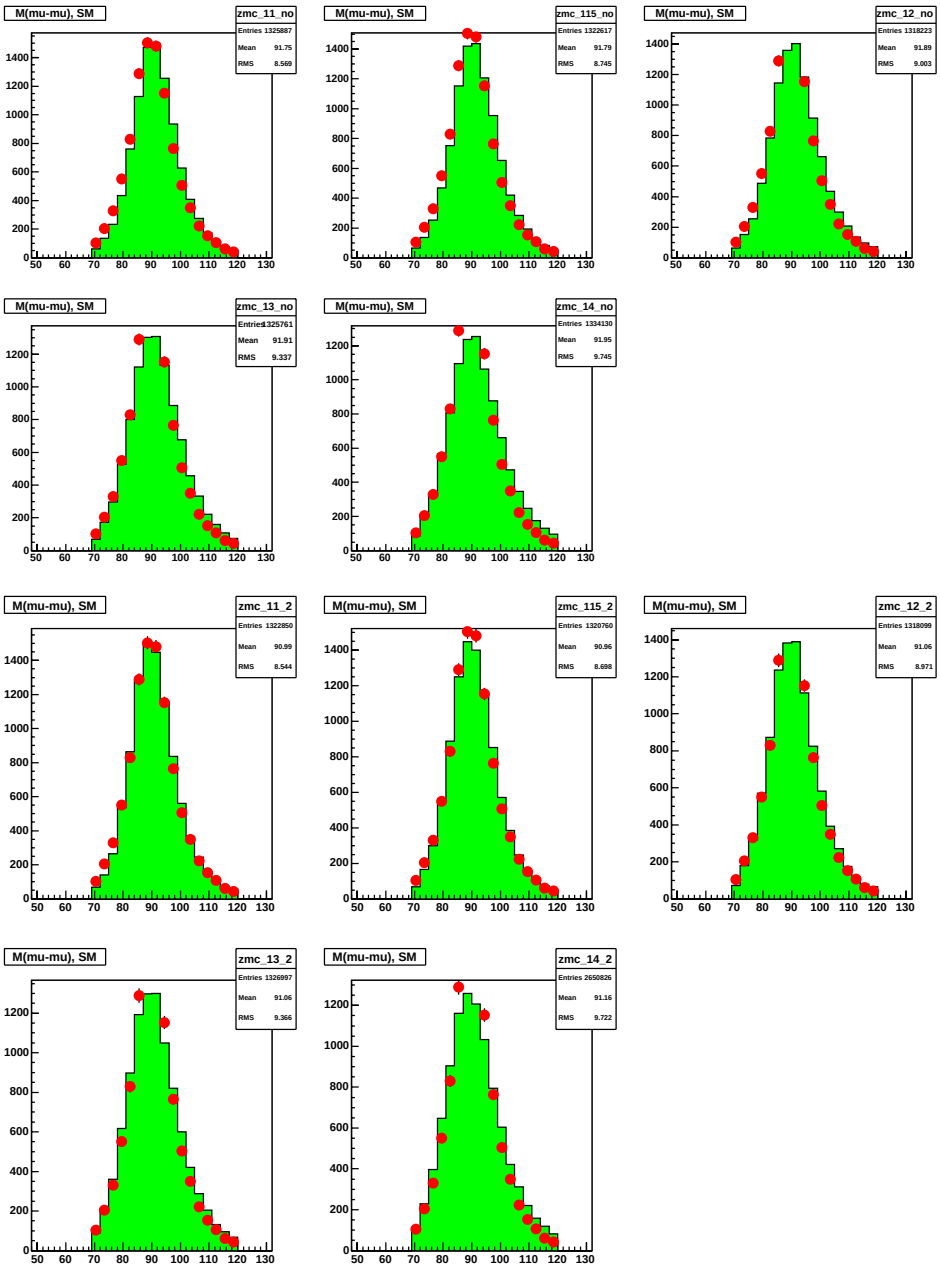

Figure 4.13. Plots of the comparisons between SM MC (histogram) and data (points) around the Z-peak for the different smearing parameters and scaling factors. Each MC distribution is area normalized to the data for this comparison. The top five plots show the mass comparisons for SF factors of 1.1 to 1.4 with $Scale = 1.0$. The bottom five plots show similar comparisons with the same ranges of SF, but with $Scale = 0.99$.

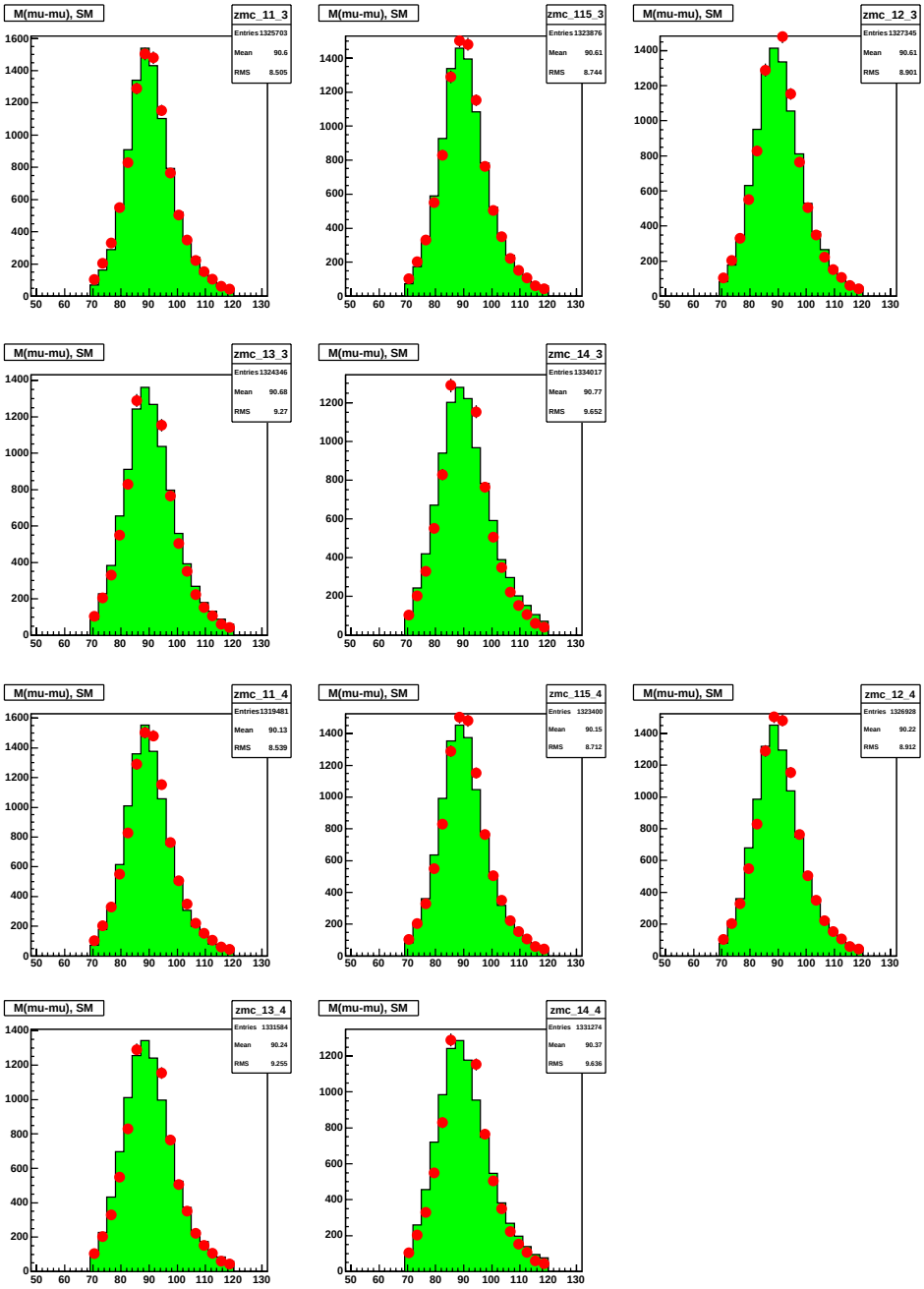

Figure 4.14. Plots of the comparisons between SM MC (histogram) and data (points) around the Z-peak for the different smearing parameters and scaling factors. Each MC distribution is area normalized to the data for this comparison. The top five plots show the mass comparisons for SF factors of 1.1 to 1.4 with $Scale = 0.985$. The bottom five plots show similar comparisons with the same ranges of SF, but with $Scale = 0.98$

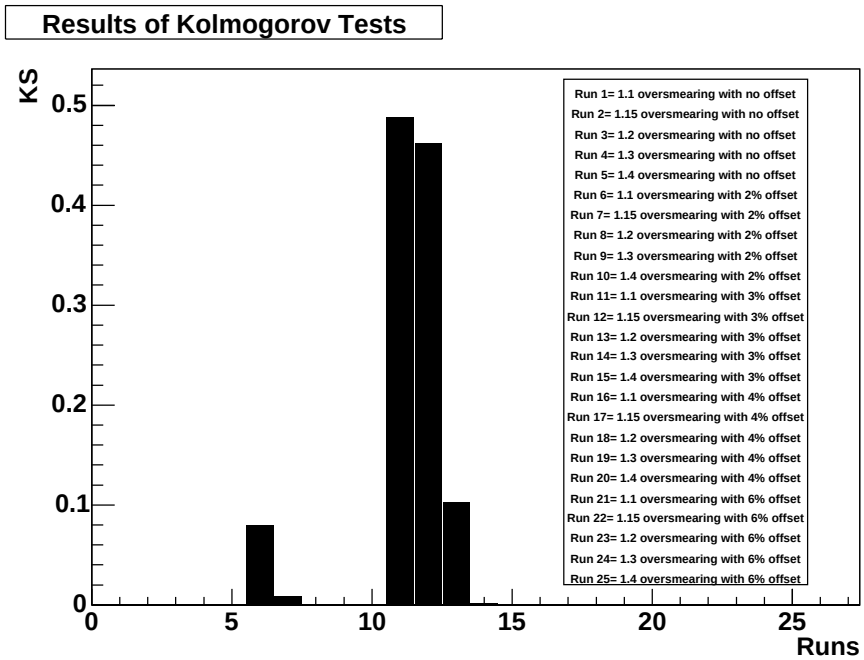

Figure 4.15. Summary of the Kolmogorov tests done to find the best smearing parameters around the Z-peak. The plot shows the Kolmogorov test results (KS) versus the different test runs. All the different runs are in this plot, but some results are too small to be seen in the figure. For instance Run 1 has a KS value of 1.5×10^{-15}.

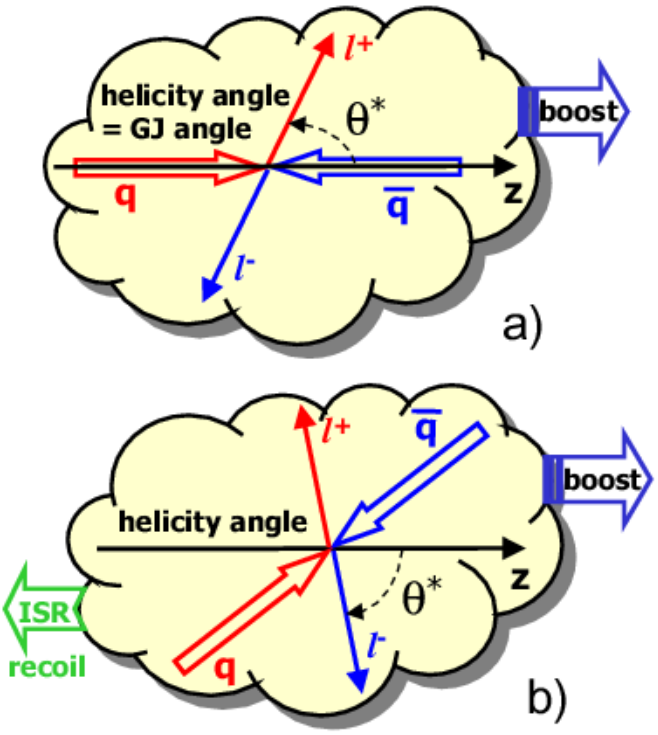

Figure 4.16. A) Shows the definition of θ^* at the parton level. B) Shows the definition of θ^* in the presence of NLO effects. Here GJ refers to the Gottfied-Jackson frame which is equivalent to the helicity frame at LO, but not with NLO effects. In this figure ISR stands for initial state radiation. Adapted from [10].

tuned to Z data. An earlier parameterization was taken from Run I and was found to be inadequate when compared to data taken with the upgraded detector. After many trials the parameterization for the generator level cross section as a function of dimuon transverse momentum is the following:

$$\begin{aligned} F(p_T(Z)) &= 3.0 + \left(-1.0 + 30.0p_T - 0.5p_T^2 + 0.001p_T^3 - 0.001p_T^4 + 0.001p_T^5\right) \\ &\quad \times \left[exp(-0.34(p_T - 15.0)) + exp(-0.14(p_T + 10.0))\right]. \end{aligned} \tag{4.2}$$

As with the momentum smearing tuning, the $KolmogorovTest$ routines are used to test the agreement between data and MC. The parameterization found gives a $KolmogorovTest$ probability of around 0.3 for the data and MC comparison. The tuning is done only with events that have invariant masses less than 120 GeV. This is to help ensure that there is not any contamination due to any possible signal. Figure 4.17 shows the dimuon p_T distributions for the old Run I parameterization, new parameterization, and data.

4.2.4 K-Factor

Since the parton-level cross section is calculated at LO, NLO effects are accounted for in the SM background by scaling the cross sections by a constant K-factor. In this context the NLO effects stem from loops in the Feynman diagrams of the exchanged Z or γ^*. The value of the K-factor for Drell-Yan processes can be obtained from theoretical calculations [10]:

$$K = 1 + \frac{\alpha_s}{2\pi}\frac{4}{3}\left(1 + \frac{4}{3}\pi^2\right) \approx 1 + 3\alpha_s \approx 1.37. \tag{4.3}$$

In this analysis the K-factor used to account for NLO effects in the SM background is 1.3 [42]. A 10% systematic uncertainty on the value of the K-factor is used to account for expected growth of the factor at high mass [42]. Because NLO corrections to the

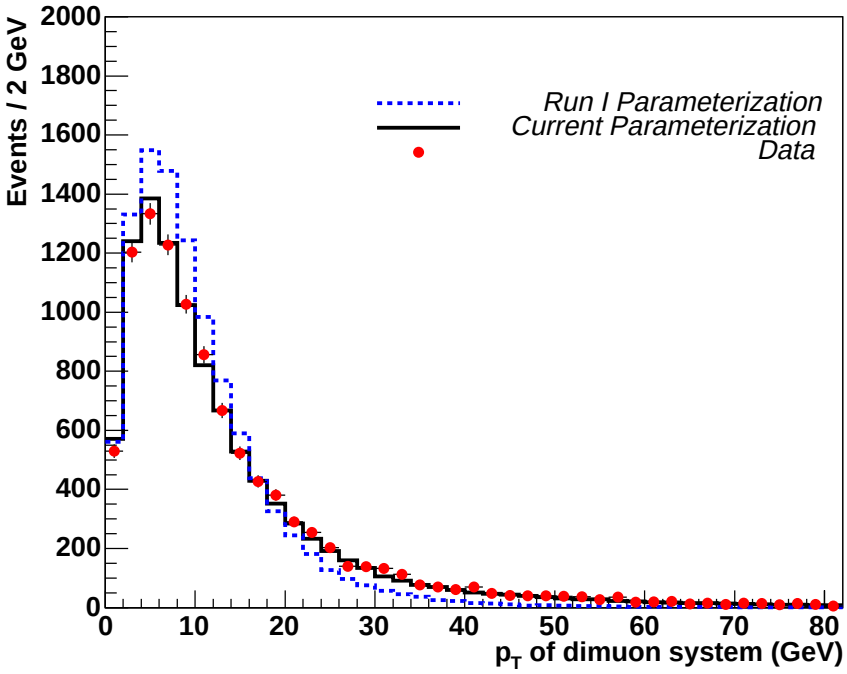

Figure 4.17. The SM dimuon p_T distributions based on the Run I parameterization, the new parameterizations, and for data.

Kaluza-Klein diagrams have not yet been calculated, the same constant K-factor is used for the signal. The K-factor for graviton exchange is expected to grow with invariant mass, similar to that for Z/γ^* exchange; consequently, this assumption tends to underestimate the LED contribution at high invariant mass.

4.3 Other Backgrounds

For completeness, backgrounds other than Drell-Yan are briefly discussed in this section. Other possible backgrounds contributing to the dimuon data set are listed below:

- $WW \rightarrow \mu\mu + X$
- $t\bar{t} \rightarrow b\bar{b} \rightarrow \mu\mu + X$
- $Z \rightarrow \tau\tau \rightarrow \mu\mu + X$
- $b\bar{b} \rightarrow \mu\mu + X$.

Due to the high p_T and invariant mass selections done for this analysis the WW, $t\bar{t}$, and $Z \rightarrow \tau\tau$ backgrounds are expected to be very small and are therefore ignored [10]. The $b\bar{b}$ backgrounds are also reduced by the kinematic selections, but this background has a much higher production cross section than the others mentioned. This is precisely why isolation requirements are applied in the data selection.

A study on the amount of $b\bar{b}$ background that pass isolation cuts was done for the $Z \rightarrow \mu\mu$ cross section measurement at DØ [43]. That study used the same CSG data set as used in this analysis and concluded the $b\bar{b}$ background constitutes a $0.6 \pm 0.3\%$ effect after isolation cuts. In the $Z \rightarrow \mu\mu$ cross section study an invariant mass cut of > 30 GeV was used as compared to the > 50 GeV cut used in this analysis. Also the isolation cuts utilized in the $Z \rightarrow \mu\mu$ cross section study are less restrictive than the > 2.5 GeV cuts used within this analysis. Therefore, the amount of $b\bar{b}$ background expected in this analysis is less than 0.6% and is ignored.

4.4 Data and Simulation Comparisons

In this section comparisons between the SM backgrounds and the final data set are examined. Also, several comparisons are shown of the expected signal with respect to background and data. First, the effective luminosity which is used to normalize the MC distributions to the data is described.

4.4.1 Normalizing MC to Data: The Effective Luminosity

The integrated luminosity of the resulting sample is 170 ± 11 pb^{-1}. Since this analysis depends only on the product of the luminosity, NLO cross section, acceptance and data selection efficiencies, the luminosity given from the luminosity system is not used in this analysis. Instead an effective luminosity is found by a fit using the MC NLO Z-peak cross section (equal to the product of the K-factor and LO cross section) to the data. This technique gives a smaller systematic error for the normalization factor than would be attained by adding in quadrature the errors from the luminosity system and all the efficiencies separately. The fit is done only in the invariant mass region less than 120 GeV. The contribution from extra dimension signal in this mass range would be negligible. The fit uses the effective luminosity as the free parameter that scales the Standard Model MC to best describe the data. Fitting is done using the data and Standard Model MC $M_{\mu\mu}$ vs. $|cos(\theta^*)|$ distributions. As a result from this fit the effective luminosity is 160.4 ± 1.6 pb^{-1}, with a $\chi^2/dof = 0.75$. The uncertainty found from the fit for the effective luminosity is 1% and is used in the calculation of limits. This uncertainty does not include the uncertainty in the K-factor for the Z cross section.

4.4.2 Data and Background Comparisons

Using the effective luminosity several different Standard Model MC distributions are normalized to the data for comparison. The first distribution examined is seen in Figure 4.18 which shows the agreement between SM background and data around the Z-peak. Figure 4.19 shows the agreement between SM background and the data for several kinematic variables. Figure 4.20 shows comparisons for the dimuon p_T distributions.

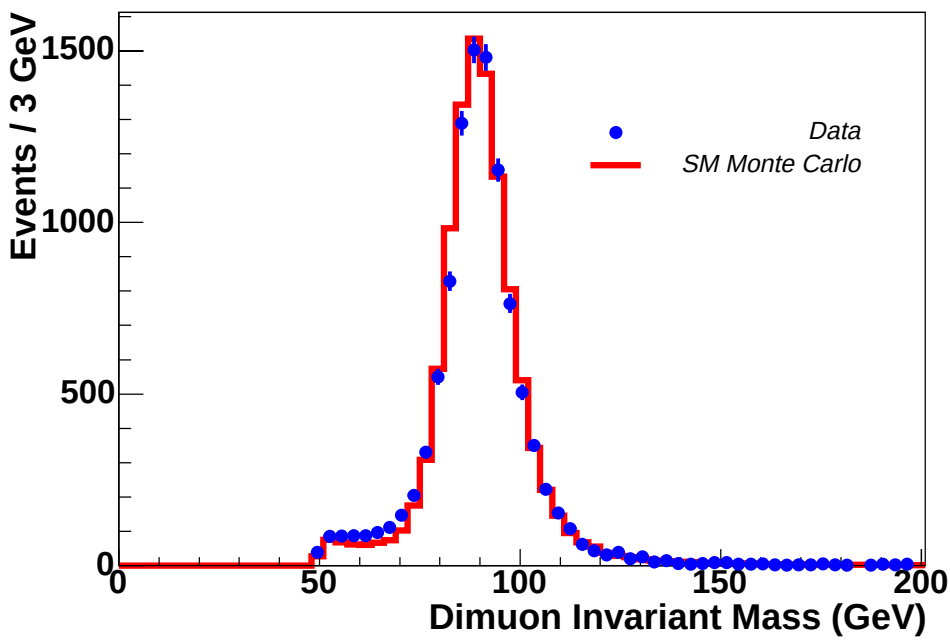

Figure 4.18. Comparison of dimuon invariant mass distributions near the Z-peak for the data (points) and background (histogram).

As discussed in Chapter 2 of this thesis, the variables used in this analysis to search for the existence of LED are $\cos(\theta^*)$ and dimuon invariant mass ($M_{\mu\mu}$). Figure 4.21 shows the comparisons between Standard Model MC and data for $\cos(\theta^*)$ and $M_{\mu\mu}$ separately. Recall that it is the two-dimensional $\cos(\theta^*)$ vs. $M_{\mu\mu}$ distributions that are used to actual perform the search for LED. The one-dimensional

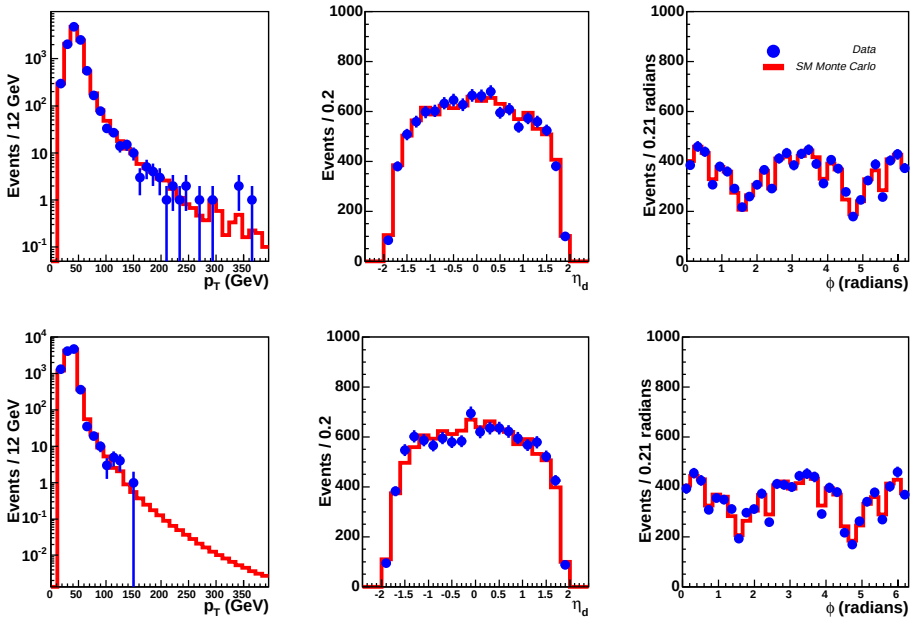

Figure 4.19. Comparison of several kinematic variable distributions for the data (points) and background (histogram). The top plots are for the highest p_T muon, while the bottom plots are for the other muon in the event.

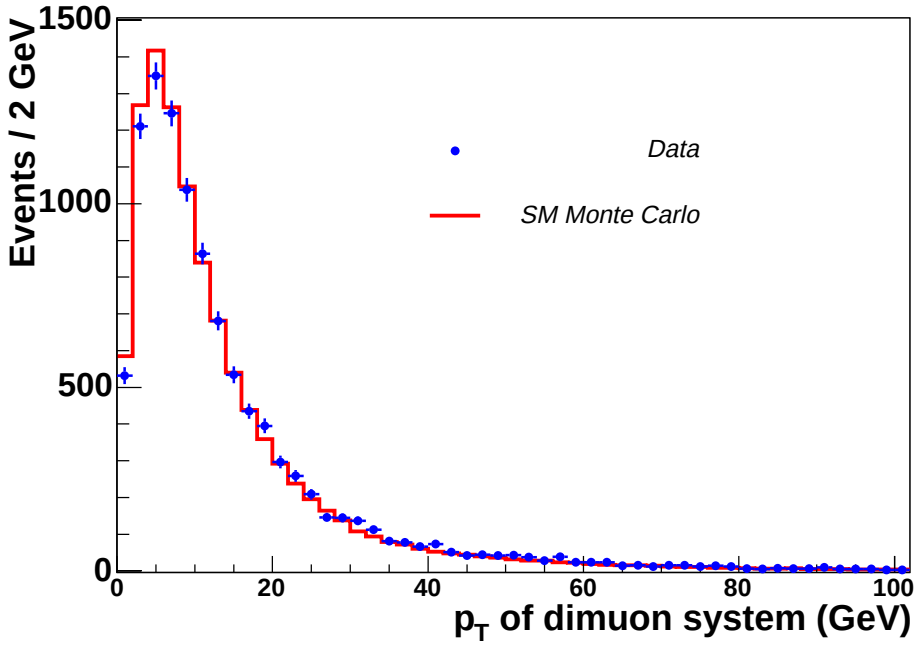

Figure 4.20. Comparison of the p_T distribution of the dimuon system for the data (points) and background (histogram).

plots are included for illustration purposes only.

Table 4.6 is included to help quantify the agreement between data and background. Above a certain lower mass cut Table 4.6 shows the expected number of SM background events along with the number of events seen in data. The last column in the table shows the Poisson probability that the expected background fluctuates up to or above the observed number of events. Overall the agreement between expected SM background and the observed data is quite good.

4.4.3 Comparisons in the Presence of a LED Signal

The cross section used to generate a LED signal is parameterized in the following bilinear form in η_G:

$$\sigma = \sigma_{SM} + \sigma_4 \eta_G + \sigma_8 \eta_G^2 \tag{4.4}$$

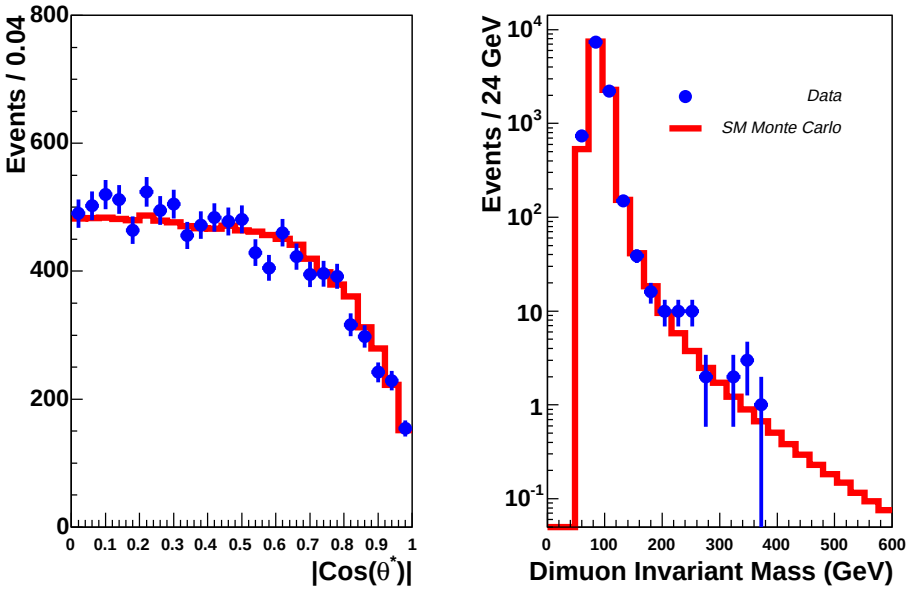

Figure 4.21. Comparison between data (points) and background (histogram) for $|\cos(\theta^*)|$ and $M_{\mu\mu}$ distributions.

Table 4.6

COMPARISON OF DATA AND EXPECTED BACKGROUND

$M_{\mu\mu}$	Expected background	Number of candidates	Poisson Probability
120 GeV	241.7	243	0.48
150 GeV	75.1	79	0.34
180 GeV	36.6	43	0.17
210 GeV	21.3	31	0.03
240 GeV	13.3	18	0.12
270 GeV	8.8	7	0.77
300 GeV	6.1	6	0.56
330 GeV	4.3	6	0.26
360 GeV	3.1	1	0.96
390 GeV	2.3	0	1.00

where σ_{SM} is the Z/γ^* contribution, σ_4 is due to the interference term between SM and the graviton (G_{KK}), and σ_8 is from the direct G_{KK} term. As discussed in Chapter 2 the term η_G represents the magnitude of the effect on the cross section due to the presence of LED. In the following figures the effects due to the presence of a LED signal are displayed for various η_G.

Figure 4.22 shows the invariant mass distributions for data, background and signal contributions with the presence of large extra dimensions. Likewise Figure 4.23 shows the $M_{\mu\mu}$ vs. $|\cos(\theta^*)|$ distributions for data, SM backgrounds, and a plot of SM with the presence of a $\eta_G = 3.0$ TeV^{-4} LED signal. Figure 4.24 illustrates the dependence of the LED signal on the parameter η_G. Note that the abundance of high $|\cos(\theta^*)|$ events are due to momentum smearing effects mentioned in the MC section of this thesis.

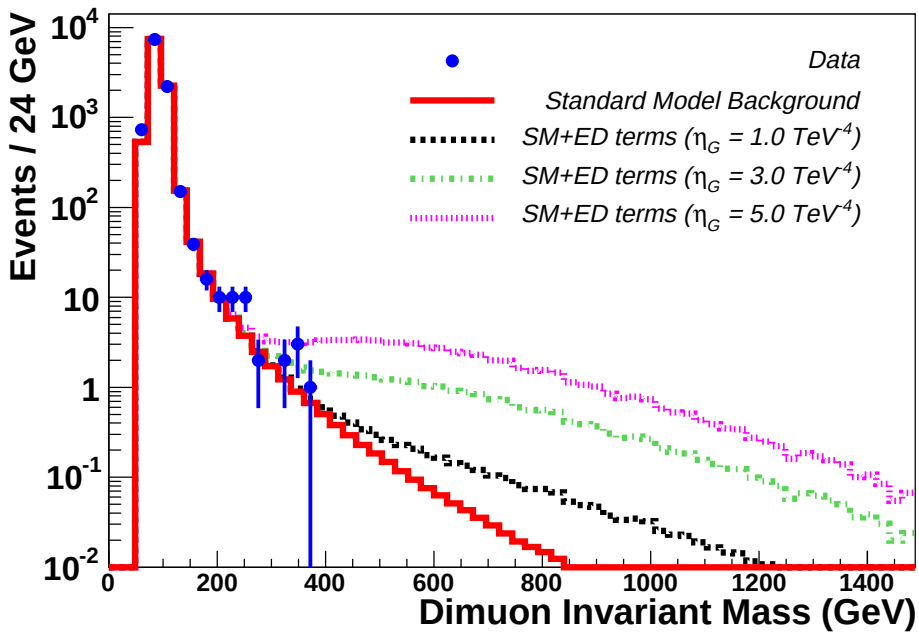

Figure 4.22. Comparison between data (points) and backgrounds (histogram) for $M_{\mu\mu}$ distributions. This plot also shows the contributions that would be expected at high $M_{\mu\mu}$ with the presence of large extra dimensions.

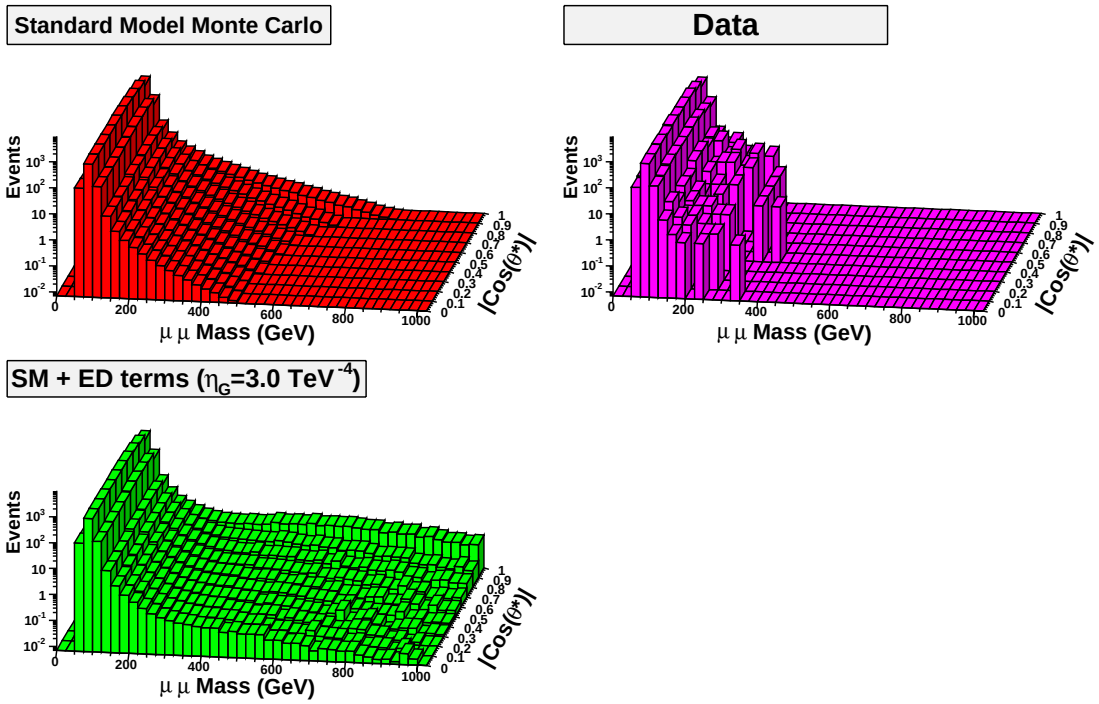

Figure 4.23. Distributions in $M_{\mu\mu}$ vs. $|\cos(\theta^*)|$ space for MC and Data. MC is scaled by the effective luminosity. The lower left plot shows SM plus contributions from the G_{KK} terms with η_G=3 TeV^{-4}.

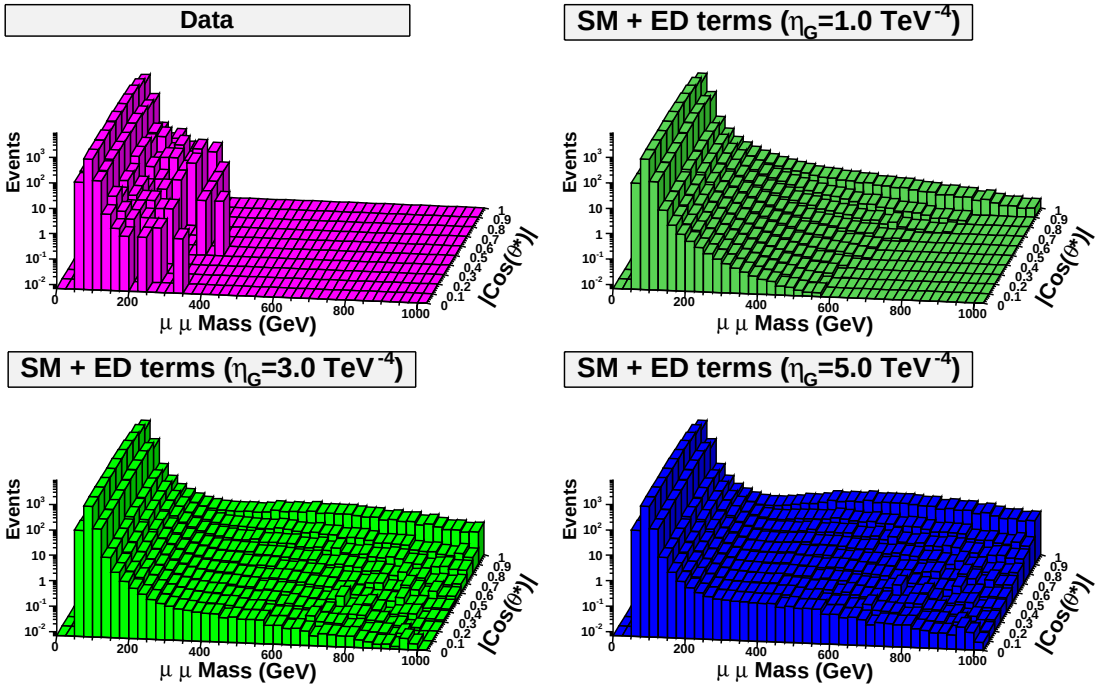

Figure 4.24. Distributions in $M_{\mu\mu}$ vs. $|\cos(\theta^*)|$ space for MC and data. MC is scaled by the effective luminosity. The top left plot shows the data sample. While the rest of the plots show MC SM plus contributions from the G_{KK} terms with η_G=1 TeV^{-4}, 3 TeV^{-4} and 5 TeV^{-4}.

4.5 Extracting the Parameter η_G from Data

The two-dimensional $M_{\mu\mu}$ vs. $|\cos(\theta^*)|$ distributions are used to determine the best fit value of η_G. This determines if the data is consistent with background alone or with a LED signal. If the data is consistent with SM backgrounds, limits on the parameter η_G are calculated at 95% confidence level.

The nominal grid size for the $M_{\mu\mu} \times |\cos(\theta^*)|$ distributions used in the fitting procedures is 20×10, where $M_{\mu\mu}$ ranges from 0 to 1500.0 GeV and $|\cos(\theta^*)|$ goes from 0 to 1.0. Different grid sizes were considered, but the nominal 20×10 grid was found to be sufficient for this analysis. As will be discussed later in this chapter a grid size of 20×1 is also used to test the effects of doing this analysis with only the invariant mass distribution.

4.5.1 Finding the Best η_G from Data

To find the best value of η_G the two-dimensional distributions of the SM, interference, and direct graviton exchange are fitted to the data. The variable η_G is a free parameter of this part of the fitting procedure. The fit includes systematic uncertainties on the inputs for the calculation of the cross sections. This 12% error is due to the energy dependence of the K-factor (10%), choice of parton distribution functions (5%) and fit to effective luminosity (1%) [10]. In addition, although no p_T dependence on the efficiency is seen in full MC, an uncertainty of 5% is used to account for any residual p_T dependence. This 5% comes from full p14 MC and data differences seen in studies done by the Muon ID group [32]. A breakdown of the systematic errors included on the cross section is given in Table 4.7.

The best value for the parameter η_G found from the fit is:

$$\eta_G = 0.00 \begin{array}{c} +0.51 \\ -0.00 \end{array} \text{ TeV}^{-4}.$$

Table 4.7

UNCERTAINTY ON THE CALCULATED CROSS SECTION

Source of systematic uncertainty	Uncertainty
K-factor	10%
Choice of p.d.f.	5%
Effective Luminosity	1%
Residual p_T dependence	5%
Total	12%

This is fully consistent with the expected SM value for η_G of zero. The conclusion is that no LED graviton signal is seen in this analysis. Even though no evidence of a LED signal has been seen in this study, it is still possible to proceed and set a upper limit on the paramter η_G and thus a lower limit on M_S.

4.5.2 Overview of the Bayesian Technique Used and 95% Confidence Level Limits for η_G

In this analysis the Bayesian approach adopted by DØ is used to find nominal limit values. This approach has the following features:

1. Probabilities are interpreted as numbers whose relative values represent the degree of confidence.
2. Previous knowledge or lack thereof is incorporated into the analysis of experimental data. This is not done for the classical Frequentist approach.
3. Bayes' theorem:

$$P(A|B) = \frac{P(B|A) \times P(A)}{P(B)} \tag{4.5}$$

In Equation 4.5, $P(A|B)$ is the probability of A given that B is true. This is also called the conditional probability. Bayes' theorem is useful in this context because it provides a way to turn the conditional probabilities around. In data analysis this property is used to relate the model that is being tested in the experiment with the

observed data:

$$P(model|data) \propto P(data|model) \times P(model). \tag{4.6}$$

The term $P(model)$ in Equation 4.6 is called the prior and it reflects the state of knowledge before the experiment. The outcome of the analysis or the posterior probability density, $P(model|data)$, is what is used to conclude the plausibility of the tested model. Often the posterior probability density is referred to as the likelihood. It should be noted that the denominator factor that should be in Equation 4.6 was intentionally omitted. This factor only contributes to the overall normalization but not to the shape of the probability density. While leaving out this factor is acceptable in the case of parameter estimation problems, it is much more important for model selection studies [3].

4.5.3 Application in the LED analysis

The MC described above generates the production cross sections used to find the limits on η_G. The production cross section is parameterized in each (i, j) bin of the $M_{\mu\mu}$ and $\cos(\theta^*)$ grid in terms of the bilinear form in η_G:

$$\sigma = \sigma_{SM} + \sigma_4 \eta_G + \sigma_8 \eta_G^2. \tag{4.7}$$

To start with it is assumed the probability to observe a certain set of events $N = \{n_{ij}\}$ as a function of η_G is given by Poisson statistics:

$$P(N|S_{ij}) = \sum_{ij} \frac{S_{ij}^{n_{ij}} e^{-S_{ij}}}{n_{ij}!}, \tag{4.8}$$

where $S_{ij} \equiv L\sigma_{ij}$, L is the effective luminosity, and σ_{ij} is the cross section given in Equation 4.7, integrated over the bin (i, j) in $M_{\mu\mu}$ and $\cos(\theta^*)$ space. Using Bayes' theorem yields:

$$P(S_{ij}|N) = P(N|S_{ij}) \times P(S_{ij}). \tag{4.9}$$

and thus,

$$P(L, \sigma_{ij}|N) = P(N|L, \sigma_{ij}) \times P(\sigma_{ij}). \tag{4.10}$$

Note the factor of L in this probability distribution. Factors such as L are referred to as nuisance parameters and can be integrated over to remove them from the probability distributions [3]. Furthermore, since it is η_G that governs the signal behavior for σ_{ij}, η_G is substituted for σ_{ij} for the remainder of this discussion.

$$P(\eta_G|N) = \int_0^\infty dL\ P(L, \eta_G|N) = \int_0^\infty dL\ P(N|L, \eta_G) \times P(L, \eta_G). \tag{4.11}$$

Assuming there are only very small correlations between η_G and L, the term $P(L, \eta_G)$ can be decomposed in the following way:

$$P(L, \eta_G) = P(L)P(\eta_G). \tag{4.12}$$

The term $P(\eta_G)$ contains any prior knowledge that we have of the LED signal. A flat prior probability is chosen here,

$$P(\eta_G) = \begin{cases} 1/\eta_G^{max}, & \text{if } 0 \leq \eta_G \leq \eta_G^{max} \\ 0, & \text{otherwise} \end{cases} \tag{4.13}$$

where η_G^{max} is chosen sufficiently large such that the likelihood that the true η_G is greater than η_G^{max} is negligible [44]. The prior for L, $P(L)$, is assumed to have a Gaussian distribution, thus:

$$P(L) = \frac{1}{\sqrt{2\pi}\sigma_L} e^{-(L-L_0)^2/2\sigma_L^2} \tag{4.14}$$

where L_0 is the nominal value for L and σ_L is its standard deviation error.

Combining the various equations yields the probability distribution for η_G given the data observed:

$$P(\eta_G|N) = \frac{1}{A} \int dL\ P(N|\eta_G) e^{-(L-L_0)^2/2\sigma_L^2}. \tag{4.15}$$

The term A in Equation 4.15 is the normalization constant and is found from the unitarity requirement:

$$\int_0^\infty d\eta_G \; P(\eta_G|N) = 1. \tag{4.16}$$

A confidence level (CL) limit is typically sought for these types of experiments. In this analysis a 95% CL limit on the parameter η_G is desired. Therefore, the 95% CL limit for η_G ($\eta_G^{95\%}$) is found from the numerical solution to the equation:

$$\int_0^{\eta_G^{95\%}} d\eta_G \; P(\eta_G|N) = 0.95. \tag{4.17}$$

Using the results from the previous sections the 95% CL upper limit on η_G is found to be:

$$\eta_G^{95\%} = \begin{cases} 0.99 \text{ TeV}^{-4} & \text{Likelihood} \\ 0.99 \text{ TeV}^{-4} & \text{Bayesian} \end{cases}$$

Both the Bayesian technique discussed and a pure Likelihood limit are calculated. The two methods give very consistent results. By changing the number of bins used in the limit calculation for $|\cos(\theta^*)|$ from 20 to 1, a result using only the one-dimensional invariant mass distribution is found. This yields a 1-D 95% CL limit on η_G of:

$$\eta_{1-D}^{95\%} = 1.0 \text{ TeV}^{-4}.$$

This is about 1% worse than the limit obtained using the two-dimensional fits.

4.5.4 Tests of Sensitivity

Several tests and cross checks are run to verify the sensibility and reliability of the result. First, 100 simulated trial experiments are run, using randomly filled $M_{\mu\mu}$ vs $|\cos(\theta^*)|$ histograms according to SM backgrounds and the effective luminosity. Then the η_G^{95} is found for each trial using both Bayesian and Likelihood methods. For each new trial experiment the two-dimensional SM histograms are fluctuated

according to Poisson statistics and refilled. This is done to see how close the found limit is to the expected sensitivity. The distribution of 95% CL limits on η_G for the 100 trials is shown in Figure 4.25 along with the results from the data. In a similar fashion Figure 4.26 shows the distribution of the best fit values of η_G for the 100 trials as well as the value found from data.

To test that the limit setting procedure is correct, 100 MC trials of background with LED signal are evaluated. The simulated LED signal is set to η_G=0.99 TeV^{-4}. Once again for each new trial experiment the two dimensional background plus signal histograms are fluctuated according to Poisson statistics and refilled. The results of the MC trials can be seen in Figure 4.27. Figure 4.27 shows that the limits found are higher than those found when there is no signal, as expected. Also, because the η_G is picked equal to the 95% limit found from data, it is expected about 5% of the trials should fall below this value. Figure 4.27 shows 8 trials (8%) from the Bayesian approach and 6 trials (6%) from the Likelihood method fall below η_G = 0.99 TeV^{-4}. This result is consistent with the expected 5%, within the statistical error associated with only 100 trials.

4.6 Results

As presented above this analysis finds no evidence of a LED graviton signal. While no signal is seen, a 95% CL upper limit on the parameter η_G is calculated. Although the parameter η_G is interesting, the real physical parameter being probed in this analysis is the fundamental Planck scale M_S. In the next section, limits on M_S are calculated from the limits on η_G.

4.6.1 From η_G to M_S

The exact dependence between η_G and M_S varies with different theoretical formalisms. Recall from Chapter 2, $\eta_G = \mathcal{F}/M_S^4$, where $\mathcal{F}$ is a dimensionless parameter

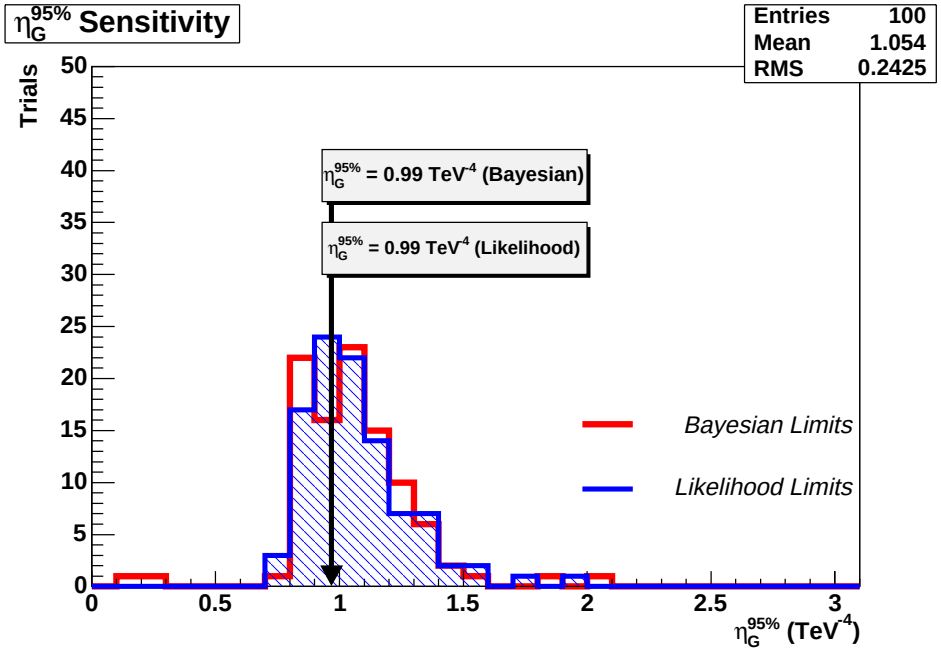

Figure 4.25. The distribution of 95% CL limits for 100 MC trials on η_G are shown here. The shaded histogram represents the Likelihood distribution, while the outlined histogram is the Bayesian distribution. Arrows with labels indicate Bayesian and Likelihood limits, found from the data.

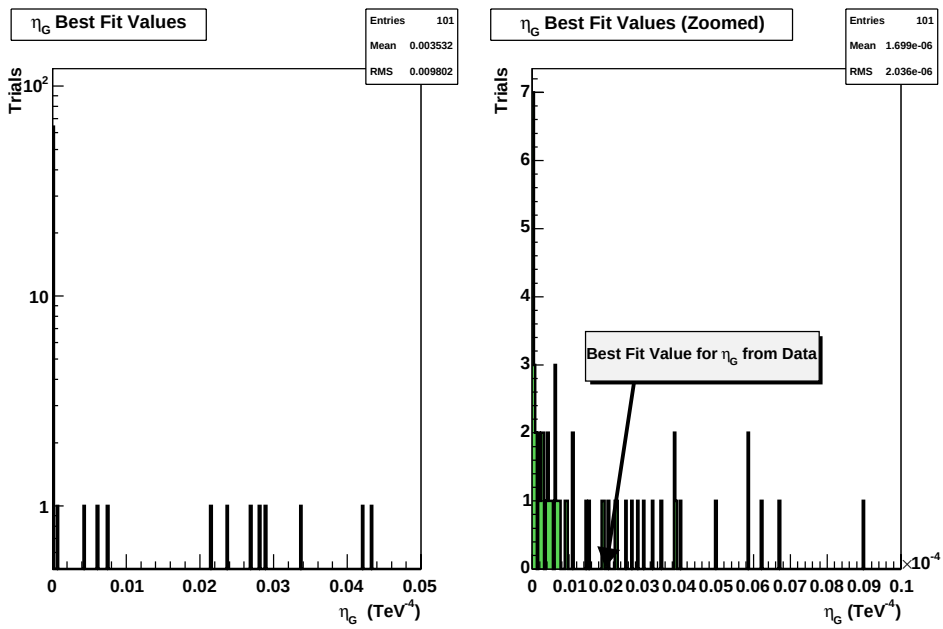

Figure 4.26. The distribution of the best fit values on η_G for 100 MC trials are shown as well as the value found from the data. The plot on the right is the same as the plot on the left but the x-axis is zoomed in to better show the values near zero. An arrow with a label indicates the best fit value found from the data.

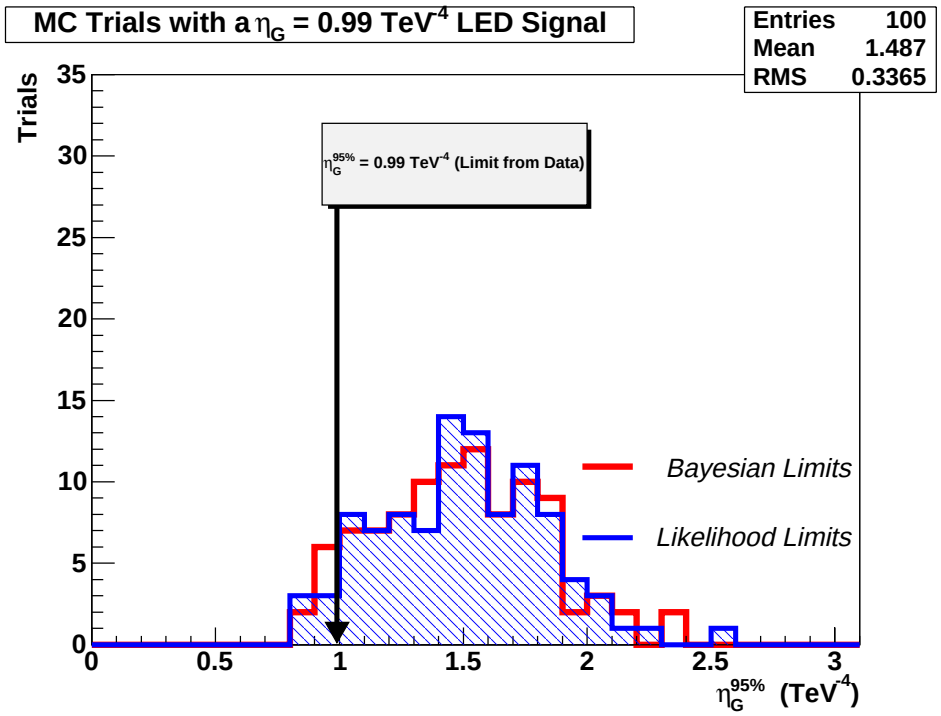

Figure 4.27. The distribution of 95% CL limits for 100 MC trials on η_G are shown here. These distributions are for background plus a LED signal of η_G=0.99 TeV^{-4}. The shaded histogram represents the Likelihood distribution, while the outlined histogram is the Bayesian distribution. The arrow with the label indicates the limit found from the data.

of order unity and reflects the dependence of virtual G_{KK} exchange on the number of extra dimensions. Different formalisms use different definitions for $\mathcal{F}$:

$$\mathcal{F} = 1, \text{ (GRW [14])}; \tag{4.18}$$

$$\mathcal{F} = \begin{cases} \log\left(\frac{M_S^2}{M^2}\right), & n = 2 \\ \frac{2}{n-2}, & n > 2 \end{cases}, \text{ (HLZ [15])}; \tag{4.19}$$

$$\mathcal{F} = \frac{2\lambda}{\pi} = \pm\frac{2}{\pi}, \text{ (Hewett [16])}. \tag{4.20}$$

For any given formalism, it is straightforward to translate the limit on η_G into a limit on M_S. Note in the HLZ formalism, for n=2, an average value of M^2 at the Tevatron of (0.64 TeV)^2 is used [37]. A summary of the 95% CL lower limits on M_S are found in Table 4.8.

Table 4.8

LIMITS FOUND FOR THE FUNDAMENTAL PLANCK SCALE M_S

Formalism for $\mathcal{F}$	GRW	HLZ						Hewett
$\mathcal{F}$ Details		n=2	n=3	n=4	n=5	n=6	n=7	$\lambda = +1$
M_S Limits (TeV)	1.00	0.94	1.19	1.00	0.91	0.84	0.80	0.90

While this limit is not the most restrictive overall for LED via virtual graviton exchange, the limit $M_S > 0.90$ TeV (Hewett $\lambda = +1$) found from this analysis does represent the best limit to date for the dimuon channel. This can be seen in Table 4.9, which summarizes various limits from other experiments as well as the $ee + \gamma\gamma$ result from DØ [10].

Table 4.9

LIMITS ON M_S FOR SEVERAL DIFFERENT EXPERIMENTS INCLUDING THE RESULT FROM THIS ANALYSIS

M_S Limits (TeV)	Channel	Experiment	Formalism for $\mathcal{F}$
0.99	e^+e^-	L3	$\lambda = +1$
0.64	$\gamma\gamma$	OPAL	$\lambda = +1$
1.1	$e^+e^- + \gamma\gamma$	DØ	$\lambda = +1$
0.60	$\mu^+\mu^-$	OPAL	$\lambda = +1$
0.69	$\mu^+\mu^-$	L3	$\lambda = +1$
0.73	$\mu^+\mu^-$	DELPHI	$\lambda = +1$
0.90	$\mu\mu$	This Result (DØ)	$\lambda = +1$

CHAPTER 5

THE Z' ANALYSIS

This chapter discusses the analysis on the search for extra neutral gauge bosons (Z') in the dimuon channel. An overview of the data selections used for this analysis is given. The Monte Carlo used to generate Z' signal as well as the dominate Drell-Yan background is discussed. By using the width of a possible Z' an optimum counting window is found and used in this study. No strong evidence of a Z' decaying into two muons is found in this analysis. Although no signal is found, limits on $\sigma \times BR(Z' \rightarrow \mu\mu)$ as well as a lower limit on the Z' mass are calculated.

Although many different theoretical models are available to explore this topic, this analysis only assumes the Sequential Standard Model (SSM) in the modeling of the Z' signal. Chapter 2 of this thesis points out that the SSM is not a gauge invariant theory. However, it still represents a good reference model to work from.

5.1 Data Sets and Selections

This analysis uses the same data and selections as the Large Extra Dimensions (LED) analysis discussed in Chapter 4 of this thesis. This is because the final state for a Z' decaying into two muons would have a similar signature to a Kaluza-Klein graviton decaying into two muons. In both cases the final state contains two isolated high p_T muons. Table 5.1 summarizes the event selections and flow. Figure 5.1 shows

the invariant mass distribution for the final data set corresponding to an integrated luminosity of 170±11 pb^{-1}.

Table 5.1

EVENT SELECTION

Selection	Number of events passing cut
Starting $TMBTree$ sample	70,450
Bad run removal	64,288
Duplicate events removed	61,577
Dimuon or single muon triggers fired	61,577
SMT hits > 0 and CFT hits > 8 per track	38,246
Dimuon invariant mass > 50 GeV	23,503
Standard timing cosmic veto	15,885
Tight cosmic cut	15,383
Calorimeter Halo < 2.5 GeV	12,023
Track Halo < 2.5 GeV	10,532
Unphysical energy cut	10,524

5.2 Backgrounds

Just as Z boson and Drell-Yan production and decay ($q\bar{q} \rightarrow Z/\gamma^* \rightarrow \mu\mu$) are the dominant backgrounds for the LED search, the same is true for the Z' search. The fast Monte Carlo (MC) used to model backgrounds in the LED analysis also models backgrounds in the Z' analysis. The muon system timing cuts and the sum eta cuts used in data selections eliminate the cosmic ray backgrounds.

5.2.1 Background Uncertainties

Systematic uncertainty on the Z/γ^* backgrounds is found from a combination of effective luminosity error used in the LED analysis and the error from the K-factor. Both of these uncertainties are described in more detail in Chapter 4. The error

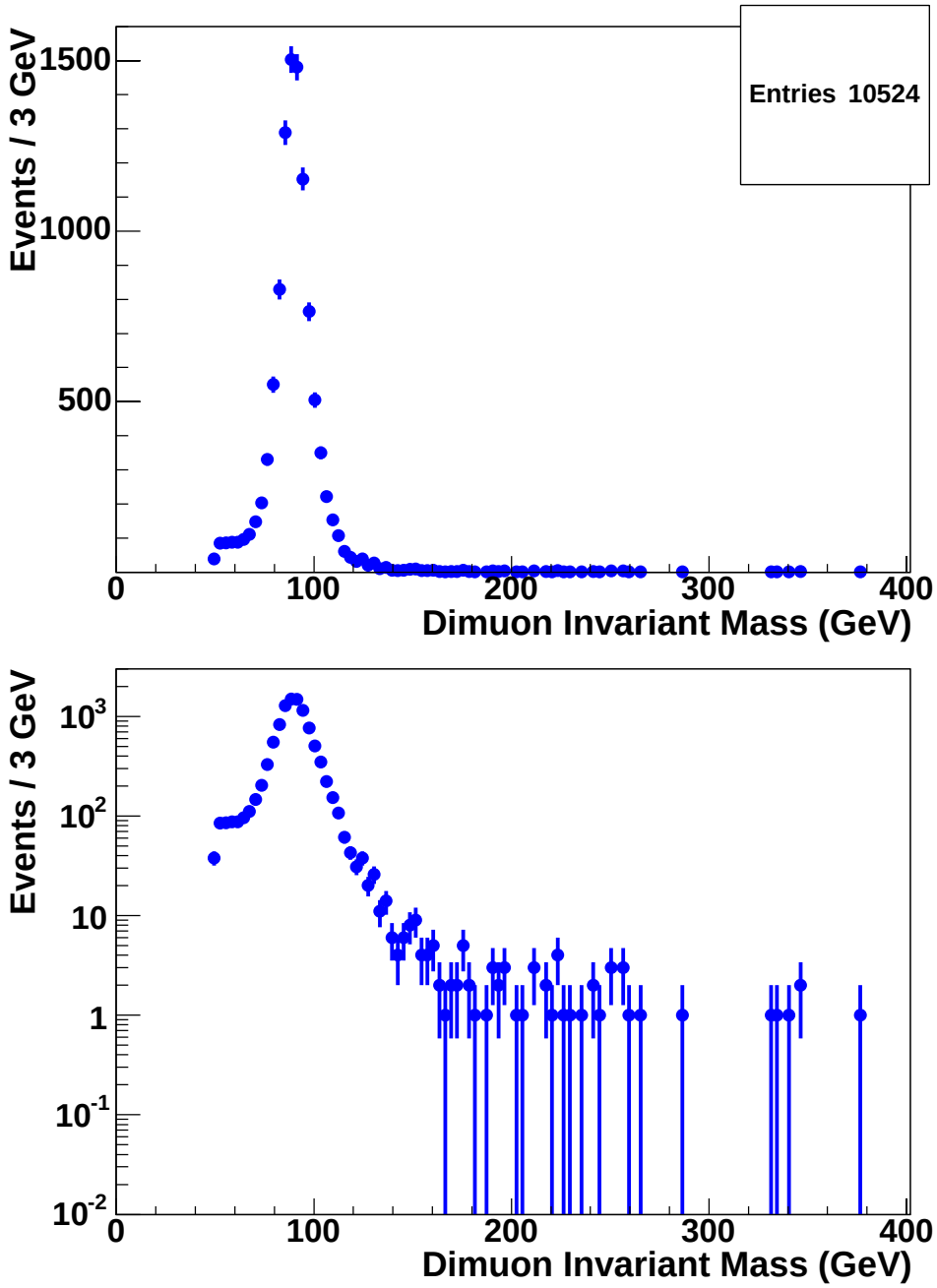

Figure 5.1. Invariant mass distribution for the final data set. Shown in both linear and semi-log scales.

from the effective luminosity is 1% and the energy dependence error on the K-factor is 10%. This yields a background error of 10% which is used in this analysis.

5.3 Monte Carlo

The MC generating the dominate Z/γ^* backgrounds is the same as for the LED analysis. It should be noted this background includes a K-factor of 1.3. To generate Z' signal events the same MC was used, but with some minor changes. The Z' analysis assumes that the detector resolutions dominate the measured width of the Z' resonance. The internal width of the Z' is thought to vary with mass in the following way,

$$\Gamma_{Z'} = (\frac{m_{Z'}}{m_Z})\Gamma_Z \tag{5.1}$$

Using the standard values for the Z boson ($\Gamma_Z = 2.49$ GeV, $m_Z = 91.19$ GeV) and a Z' mass of 600 GeV, yields an internal width for the Z' of 16 GeV. Variations to the internal width are very small relative to detector resolutions, which are on the order of 200 GeV for a Z' with invariant mass of 600 GeV. Therefore, any changes of the Z' internal width as a function of mass are ignored for this analysis.

The MC allows a user to quickly set the mass at which the Z boson is generated. Therefore, modeling a SSM Z' signal at any desired mass is straightforward. This is done for several different masses, specifically 200 GeV, 250 GeV, 300 GeV, 350 GeV, 400 GeV, 450 GeV, 500 GeV, 600 GeV and 700 GeV. Figures 5.2 show the generated signal resonances for the different Z' masses explored. Each resonance is fit with a Gaussian plus Landau fit function. The Gaussian fit alone does not accurately describe the high mass tail, and the addition of the Landau function results in a better overall fit χ^2. All fits use the standard routines found in the ROOT software package [41].

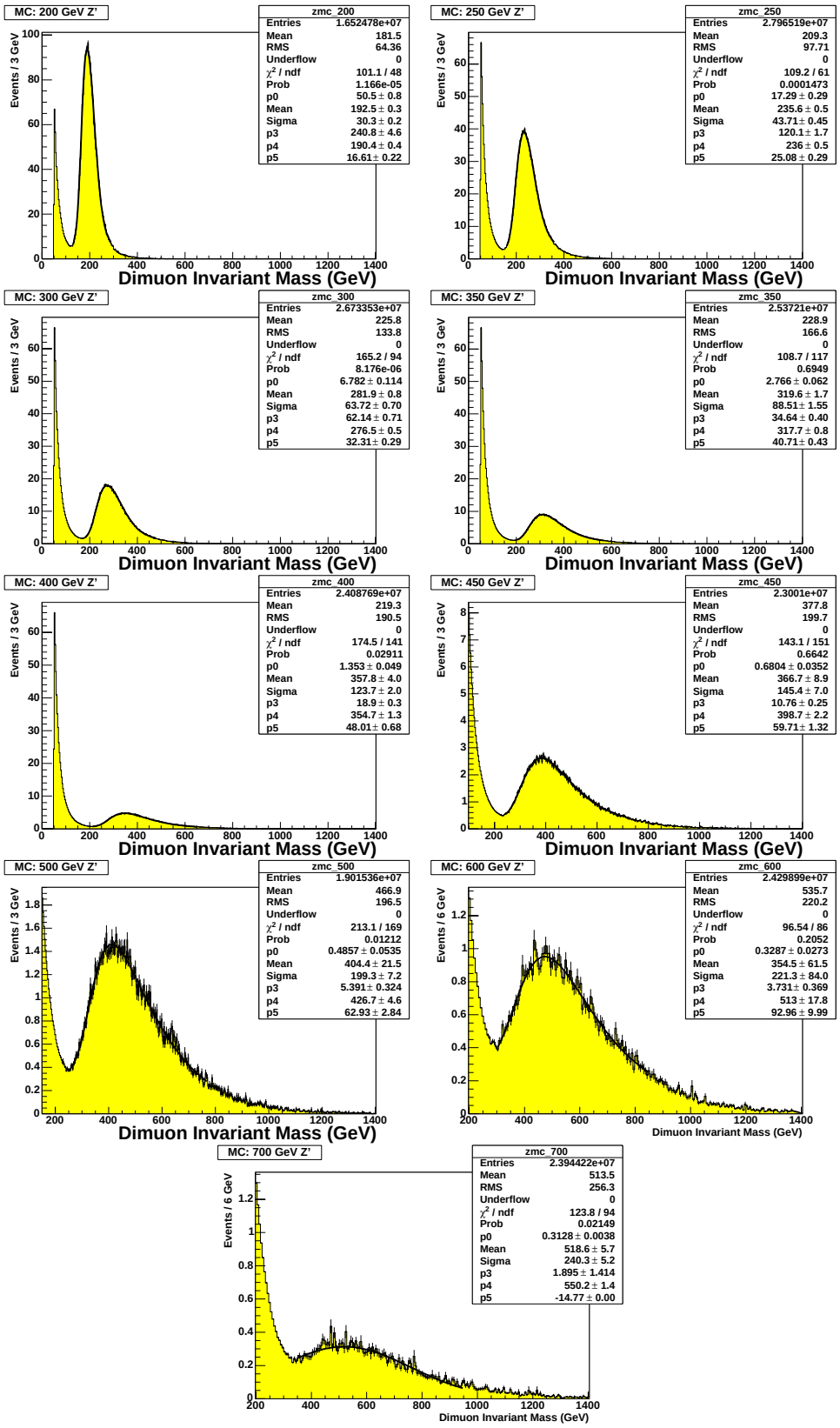

Figure 5.2. Invariant mass distributions for different mass Z' decaying into two muons.

5.4 Optimum Cut Window

For each generated Z' mass, the mass window in which the counting experiment is done is optimized. Background and signal samples generated by the MC described in the previous sections are used for this optimization. The optimization procedure attempts to maximize the ratio of signal over square root background ($S/\sqrt{B}$). The assumption used here for the fit to the signal is that the signal is a Gaussian distribution on the falling Drell-Yan background. In the previous section it was stated that the fit to the signal actually used was a Gaussian with a Landau fit function. While this is true, in the construction of $S/\sqrt{B}$ a Gaussian functional form alone is used for the signal. This is done for simplicity as well as the fact that the background is a sharply falling distribution and thus $S/\sqrt{B}$ is not very sensitive to where the high invariant mass cut is placed. This is why one sided integrals are used in this analysis. As seen in Figure 5.2 the lower mass spectrum part of the signal is described well by a Gaussian. Furthermore, this is where $S/\sqrt{B}$ is most sensitive to a cut, therefore only the Gaussian functional form is used in the construction of $S/\sqrt{B}$. For the signal the functional form in Equation 5.2 is used.

$$S \sim \frac{1}{\sigma\sqrt{2\pi}} \int_{M_0-W}^{\infty} \exp\left(-\frac{(\sqrt{s}-M_0)^2}{2\sigma^2}\right) d\sqrt{s} \tag{5.2}$$

M_0 is the mean mass found from the Gaussian plus Landau fit to the MC signal and W is the displacement from M_0 where the integration starts. The variable s is the center-of-mass energy and σ is from the Gaussian part of the fit to the MC signal. For the background, we fit a function to the falling tail of the Drell-Yan distribution generated from the MC. The form used is seen in Equation 5.3.

$$B \sim \int_{M_0-W}^{\infty} \left(C_0 + e^{(-\alpha_1\sqrt{s}+C_1)} + e^{(-\alpha_2\sqrt{s}+C_2)}\right) d\sqrt{s} \tag{5.3}$$

The parameters $C_0, C_1, C_2, \alpha_1, \alpha_2$ are all found from the fit to the falling distribution. A plot of the fit function, its parameters and the falling Drell-Yan MC distribution is shown in Figure 5.3.

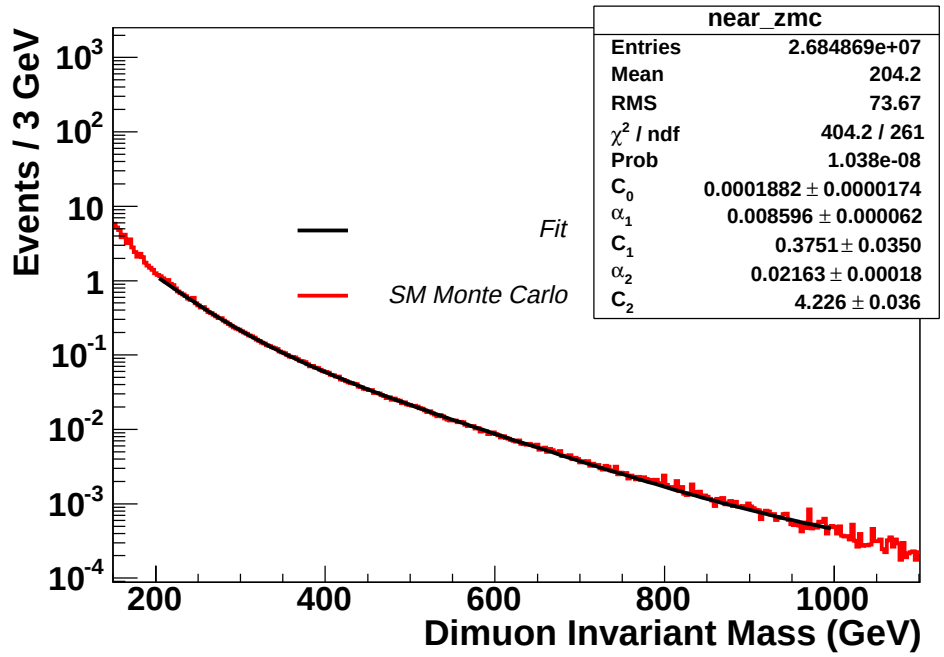

Figure 5.3. Fit to the falling Drell-Yan MC distribution.

Combining Equations 5.2 and 5.3, the ratio $S/\sqrt{B}$ is formed and is shown in Equation 5.4. To approximate infinity in the actual counting the upper cut window is set to be at 1500 GeV for all resonances.

$$\frac{S}{\sqrt{B}} \sim \sigma\sqrt{2} \times erfc\left(-\frac{W}{\sigma\sqrt{2}}\right)\left(1500C_0 + \frac{C_0 W}{\sigma\sqrt{2}} + \frac{e^{-\alpha_1(M_0+C_1-W)}}{\alpha_1\sigma\sqrt{2}} + \frac{e^{-\alpha_2(M_0+C_2-W)}}{\alpha_2\sigma\sqrt{2}}\right)^{-\frac{1}{2}} \tag{5.4}$$

In Equation 5.4 $erfc(x)$ is the error function, defined in Equation 5.5 as:

$$erfc(x) = \frac{2}{\sqrt{\pi}} \int_x^\infty e^{-t^2} dt. \tag{5.5}$$

Figure 5.4 shows the Equation 5.4 plotted for the different mass points explored. Where $S/\sqrt{B}$ is a maximum defines the optimum lower mass cut used in this analysis.

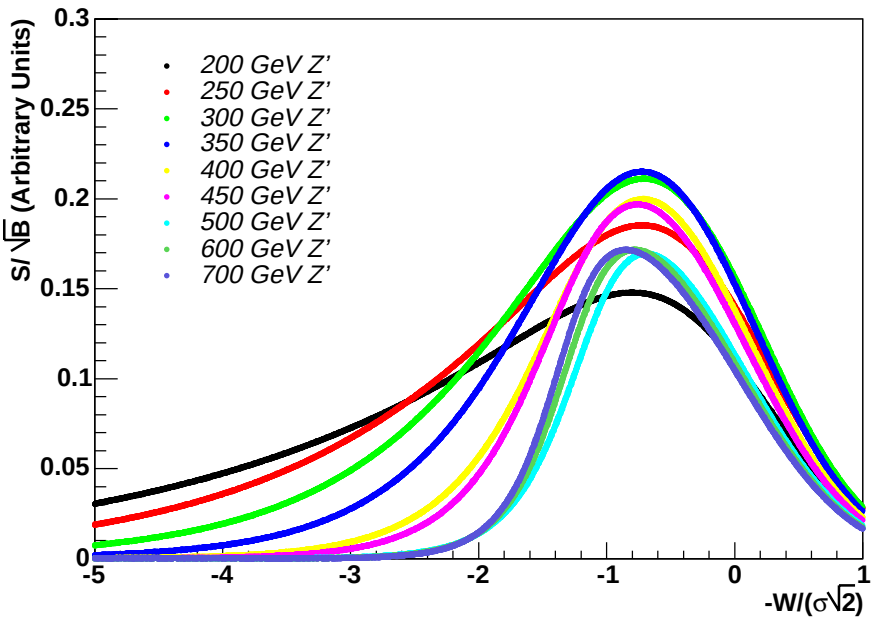

Figure 5.4. Signal over square root background for a Gaussian signal on the falling background. The different traces show the $S/\sqrt{B}$ for different resonance masses.

5.5 Acceptance

The acceptance for this analysis is found by using the MC with the acceptance maps from the LED analysis. Comparing generator level outputs with acceptance only outputs creates an acceptance versus invariant mass distribution. A second order polynomial is then fit to the acceptance distribution. The end-points for the fit are defined as a $\pm 1\sigma$ window centered on M_0. We then evaluate the fit function

and thus the acceptance at M_0. Figure 5.5 shows the fit to the acceptances for the different Z' masses explored.

5.5.1 Systematic Errors on the Acceptance

To estimate the systematic errors associated with the acceptance calculation a fit to the data Z-peak is formed. This fit uses a Gaussian plus Landau to fit the Z-peak, plus a exponential function to fit the underlying Drell-Yan events. From this fit to the data it is assumed that the error associated with the Z-peak width gives an estimate on the error of the MC momentum smearing parameter C. The meaning of parameter C is defined in the MC section of Chapter 4. Figure 5.6 shows the fit to the data Z-peak as well as σ_Z and its error. The one standard deviation errors on σ_Z from the fit provide an estimate for the error on the parameter C and thus the width of the Z' signal resonances. The width of the signal resonances depends very strongly on the smearing parameter C used in the MC. It is this width, specifically σ, that is used to define the window end points for the fits to the acceptance distributions.

Adjusting the smearing parameters by ± 1 standard deviation and redoing the acceptance calculation resulted in a systematic error of about (0.1-0.5)%. While this is small, to be conservative, a 1% error is assigned to all the acceptances found.

5.6 Results and Limits

Figure 5.7 shows the invariant mass distribution comparison between data and background predictions. Table 5.2 summarizes the acceptances calculated and the comparisons between background and data for the seven different Z' masses examined. The figures and tables show that the agreement between data and background predictions are very good. Therefore, this analysis finds no evidence of a $Z' \rightarrow \mu\mu$ signal.

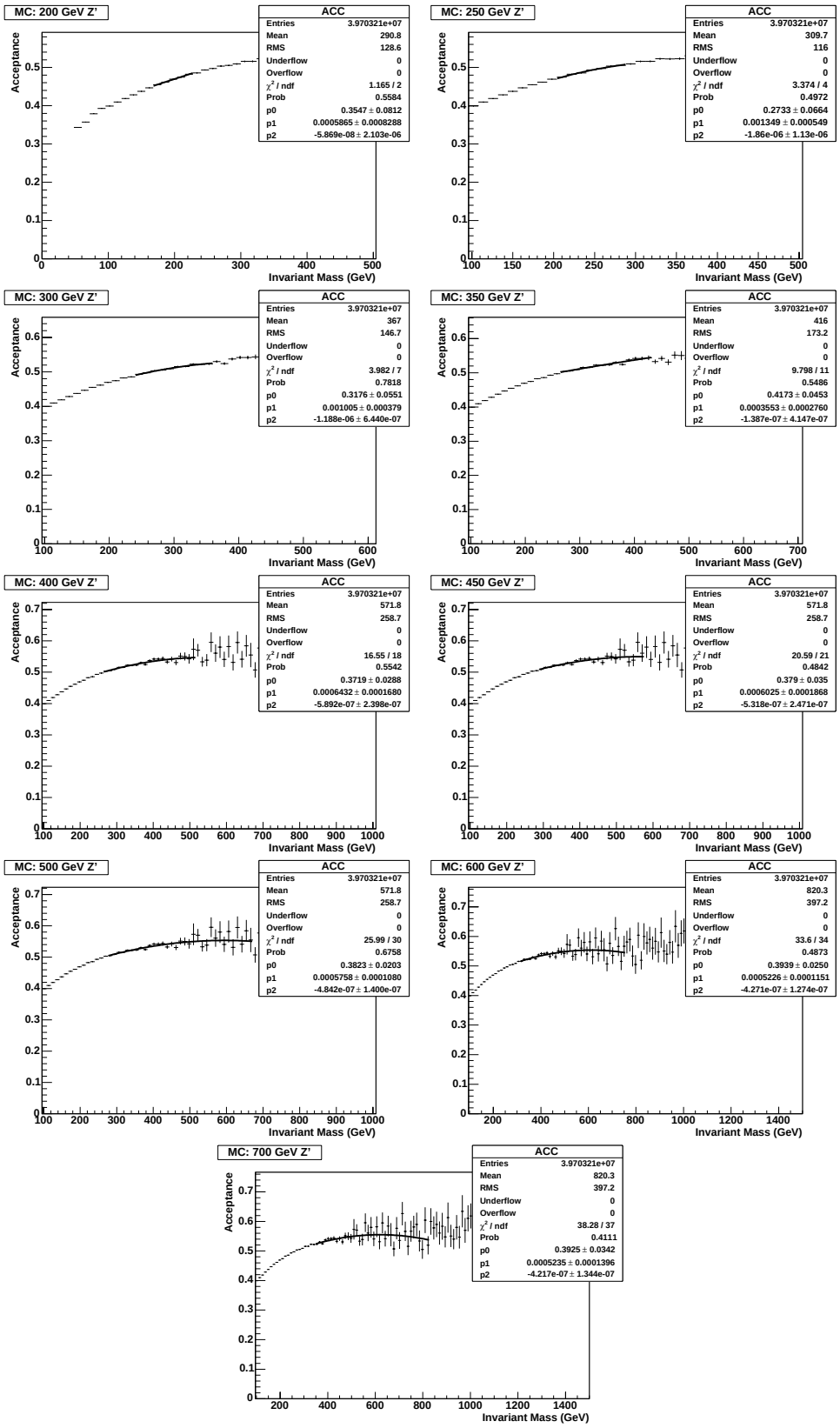

Figure 5.5. Acceptance fits using a 2nd order polynomial.

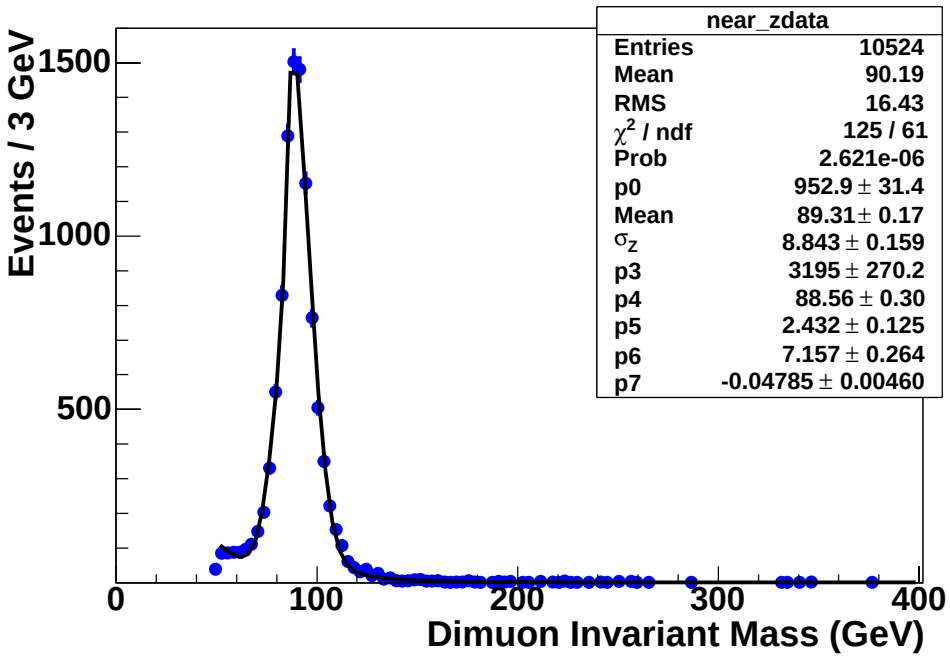

Figure 5.6. This plot shows the Gaussian plus Landau with a exponential background fit to the data Z-peak. Parameter 2 in this plot is σ_Z, along with its error which is used in the acceptance section of this analysis.

Table 5.2

SUMMARY OF ACCEPTANCE, DATA, AND BACKGROUNDS IN THIS ANALYSIS

Z' Mass	200 GeV	250 GeV	300 GeV
Acceptance	0.470	0.494	0.513
Cut Window	166-1500 GeV	204-1500 GeV	239-1500 GeV
Background	54.6±5.5	24.8±2.5	14.0±1.4
Data	57	33	18
Z' Mass	350 GeV	400 GeV	450 GeV
Acceptance	0.525	0.535	0.541
Cut Window	262-1500 GeV	273-1500 GeV	285-1500 GeV
Background	10.2±1.0	8.7±0.9	7.5±0.8
Data	9	7	7
Z' Mass	500 GeV	600 GeV	700 GeV
Acceptance	0.547	0.552	0.555
Cut Window	282-1500	296-1500 GeV	308-1500 GeV
Background	7.7±0.8	6.4±0.6	5.6±0.6
Data	7	6	6

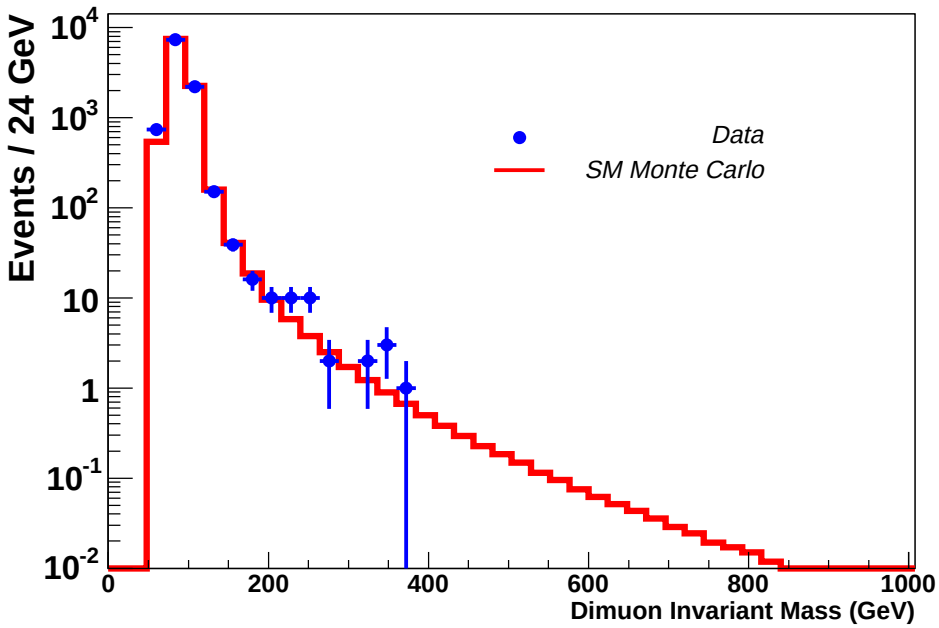

Figure 5.7. Invariant mass distributions for data (points) and background (histogram).

5.6.1 Z' Mass Limit

Even though no evidence of a $Z' \rightarrow \mu\mu$ signal has been seen in this study, it is still possible to proceed and set a lower limit on the mass of a SSM Z'. This analysis utilizes the Bayesian confidence limit setting recipe suggested by the Run I "Search Limits Committee" [44]. The Bayesian technique used for this analysis is very similar as that used in the LED analysis. For further details please refer to Chapter 4 of this thesis. This fitting procedure has been programmed into a easy to use ROOT macro. The macro program can be found at [45]. Table 5.3 summarizes the inputs and errors used in the limit setting procedure.

This analysis finds 95% CL experimental limits on $\sigma \times BR(Z' \rightarrow \mu\mu)$ which are summarized in Table 5.4 and in Figure 5.8. The theoretical cross sections used are scaled by the same K-factor of 1.3 used for the background [5]. Figure 5.8 also

Table 5.3

SUMMARY OF THE LIMIT SETTING INPUTS AND ERRORS

	Value	Error
Luminosity	170pb^{-1}	6.5%
Acceptance	0.470-0.555	1.0%
Background	See Table 5.2	10%
Total		12%

shows the theoretical $\sigma \times BR(Z' \rightarrow \mu\mu)$ versus invariant mass. The theoretical curve crosses the experimental limit at 690 GeV, which defines the experimental lower mass limit on a SSM Z' decaying into two muons.

Table 5.4

THEORETICAL AND MEASURED $\sigma \times BR(Z' \rightarrow \mu\mu)$

Z' Mass (GeV)	$\sigma \times BR(Z' \rightarrow \mu\mu)$ (pb) theoretical (LO×1.3)	$\sigma \times BR(Z' \rightarrow \mu\mu)$ (pb) 95% CL Experimental Limit
200	18.76	0.271
250	–	0.246
300	4.475	0.156
350	–	0.084
400	1.379	0.072
450	–	0.077
500	0.472	0.075
600	0.176	0.071
700	0.067	0.076

In Chapter 2 of this thesis the world's various Z' mass limits were discussed. Table 5.5 reviews the Z' mass limits found from collider experiments for a SSM Z' [5]. As can be seen from Table 5.5 the Run I CDF combined ($ee + \mu\mu$) limit is

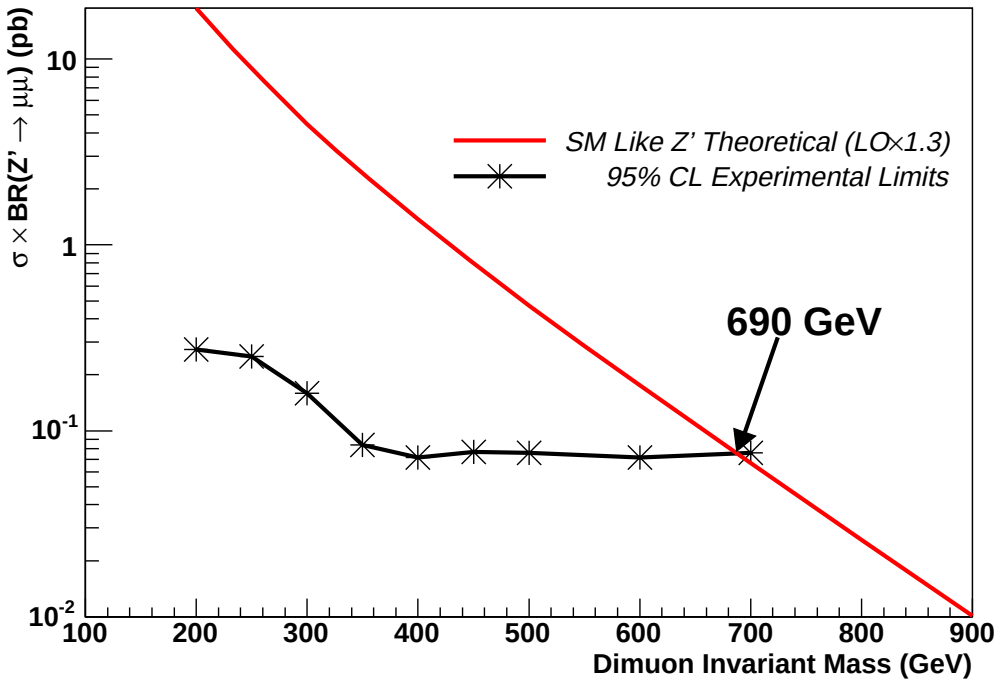

Figure 5.8. The 95% CL limits on $\sigma \times BR(Z' \to \mu\mu)$.

the most restrictive to date. While the result from this analysis ($M_{Z'} > 690$ GeV) does not supersede the CDF result, it is comparable using only the $\mu\mu$ channel.

Table 5.5

SUMMARY OF CURRENT HADRON COLLIDER Z' MASS LIMITS AND THE LIMIT OBTAINED FROM THIS ANALYSIS

Z' Models	Mass (95% CL)	Experiment	Comments
Z_{SSM} Sequential SM	> 670 GeV	DØ	ee channel
	> 690 GeV	CDF	ee, $\mu\mu$ combined
	> 690 GeV	This Result (DØ)	$\mu\mu$ channel

CHAPTER 6

CONCLUSIONS

A search for large extra spatial dimensions and Z' was performed in the dimuon channel using 170± pb^{-1} of DØ Run II data. No evidence is seen for signal beyond the expected backgrounds in either search.

In the search for large extra spatial dimensions, agreement with the expected Standard Model background is shown in the dimuon invariant mass versus $\cos(\theta^*)$ distribution. Based on this consistency of the data with the Standard Model, 95% confidence level limits are placed on the fundamental Planck scale, M_S. Obtained is a lower 95% confidence limit of $M_S > 1.0$ TeV in the GRW convention. This represents the best limit to date for such a search in the dimuon channel.

The Z' search shows good agreement between the measured high p_T dimuon mass spectrums with the Standard Model background. Due to this agreement between data and background a lower 95% confidence level mass limit of $M_{Z'} > 690$ GeV for a Sequential Standard Model Z' is found. The limit found in this study is comparable with the combined $(ee + \mu\mu)$ CDF Run I Z' limit [5].

APPENDIX A

INTERESTING CANDIDATE EVENTS

For this analysis I define a interesting candidate event by those events which have high dimuon invariant mass. In the final sample there are six events with mass above 300 GeV, but I pick the event with the highest mass as one candidate event to examine. The other candidate event examined is the event with the highest mass while simultaneously the lowest $\cos(\theta^*)$.

Parameters for the candidate events are listed in Tables A.1-A.2. Table A.1 contains the information for the event with the highest invariant mass, while Table A.2 illustrates the same information for the candidate event that has the highest mass and lowest $\cos(\theta^*)$. Event displays for these events are shown in Figures A.1-A.2.

Table A.1

PARAMETERS OF THE HIGHEST MASS DIMUON CANDIDATE EVENT

Run	Event	M (GeV)	$\cos(\theta^*)$	N_{jet}	$\not{E}_T$ (GeV)
179115	50856846	376.1	0.49	0	3.4

	μ_1	μ_2
p_T (GeV)	169.8	127.8
ϕ (radians)	1.1	4.3
η	-0.6	0.9
A-Layer Scintillator Time (ns)	-1.4	-2.3
BC-Layer Scintillator Time (ns)	2.3	0.9
Calorimeter Halo (GeV)	0.7	0.5
Track Halo (GeV)	0.8	1.3

Table A.2

PARAMETERS OF THE HIGHEST MASS WITH LOWEST COS(Θ^*) DIMUON CANDIDATE EVENT

Run	Event	M (GeV)	$\cos(\theta^*)$	N_{jet}	$\not{E}_T$ (GeV)
178761	20213786	340.0	0.05	1	18.4

	μ_1	μ_2
p_T (GeV)	203.9	125.1
ϕ (radians)	2.2	5.6
η	0.6	1.4
A-Layer Scintillator Time (ns)	3.1	2.1
BC-Layer Scintillator Time (ns)	-0.9	1.0
Calorimeter Halo (GeV)	0.2	0.2
Track Halo (GeV)	0.0	0.7

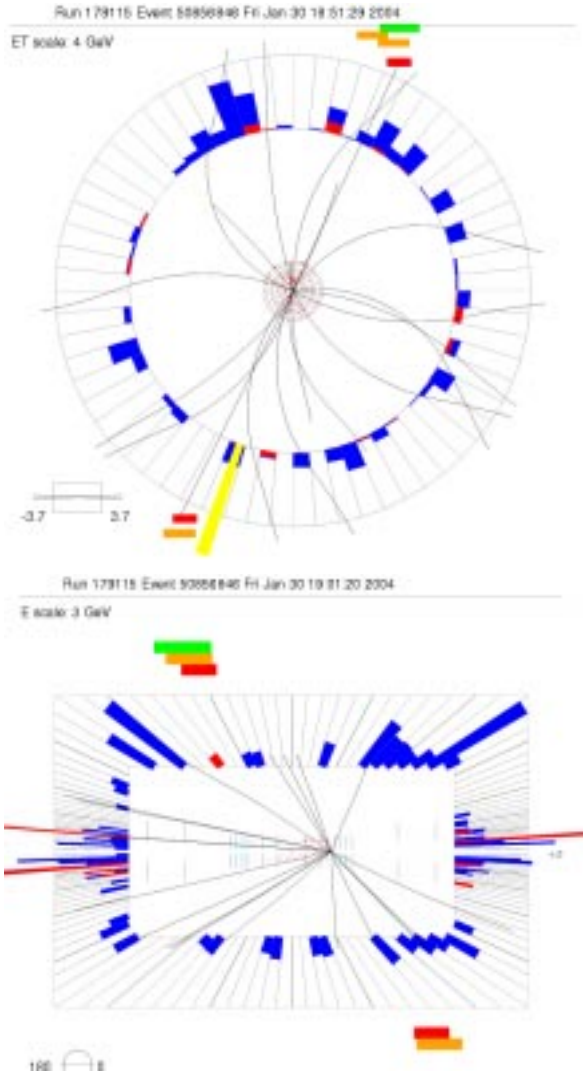

Figure A.1. The top figure shows the central tracking system XY view for our highest mass candidate. Reconstructed tracks are shown as well as muon system hits displayed as polygons. The bottom figure shows the $r - z$ view for our highest mass candidate. Reconstructed tracks are shown as well as muon system hits displayed as rectangles.

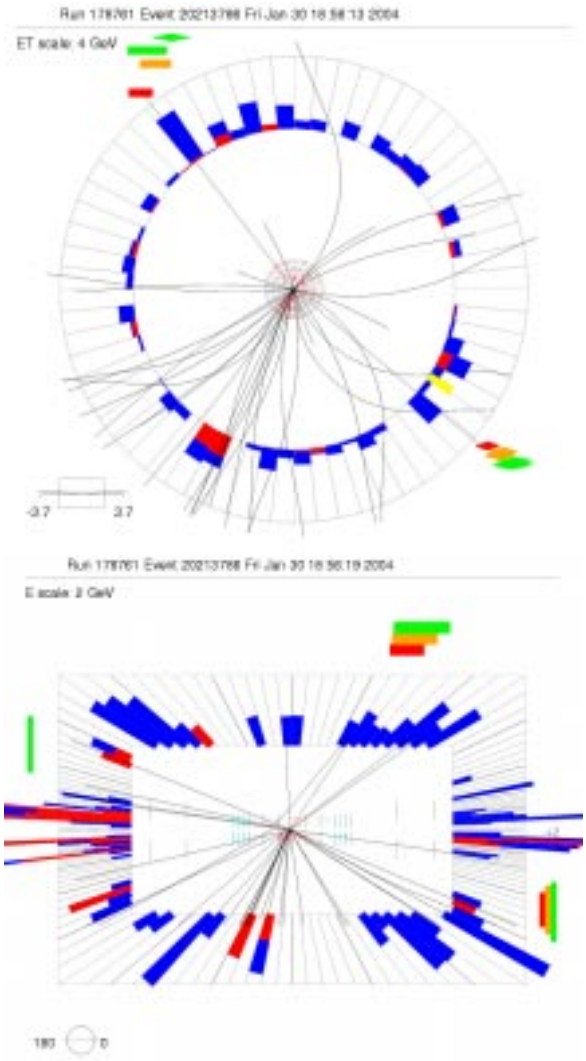

Figure A.2. The top figure shows the central tracking system XY view for our highest mass with the lowest $\cos(\theta^*)$ event. Reconstructed tracks are shown as well as muon system hits displayed as polygons. The bottom figure shows the $r - z$ view for our highest mass with the lowest $\cos(\theta^*)$ candidate. Reconstructed tracks are shown as well as muon system hits displayed as rectangles.

BIBLIOGRAPHY

[1] M. Kaku, "Quantum Field Theory a Modern Introduction", Oxford University Press, New York (1993).

[2] B. Roe, "Particle Physics at the New Millennium", Springer, New York (1996).

[3] A. Melnitchouk, *Search for non-SM Light Higgs Boson in the $h \to \gamma\gamma$ Channel*, Ph.D. Thesis, Brown University, 2003 (unpublished).

[4] M. Peskin and D. Schroeder, "An Introduction to Quantum Field Theory", Addison-Wesley Publishing Company, New York, (1995).

[5] M. Gao, *A Search for Extra Neutral Gauge Boson in the Dielectron Channel with the DØ Detector in $p\overline{p}$ Collisions at $\sqrt{s}$=1.96 TeV*, Ph.D. Thesis, Columbia University, 2003 (unpublished). And private communications.

[6] N. Arkani-Hamed, S. Dimopoulos, G. Dvali, Phys. Lett. **B429**, 263 (1998).
I. Antoniadis, N. Arkani-Hamed, S. Dimopoulos, and G. Dvali, Phys. Lett. **B436**, 257 (1998).
N. Arkani-Hamed, S. Dimopoulos, G. Dvali, Phys. Rev. D **59**, 086004 (1999).
N. Arkani-Hamed, S. Dimopoulos, J. March-Russell, SLAC-PUB-7949, e-Print Archive: hep-th/9809124.

[7] The CDF Collaboration, Phys. Rev. Lett. **79** 2191 (1997).

[8] P. Horava and E. Witten, Nucl. Phys. **B460**, 506 (1996); *ibid.*, **B475**, 94 (1996).
E. Witten, *ibid.* **B471**, 135 (1996).
I. Antoniadis, Phys. Lett. **B246**, 377 (1990).
J. Lykken, Phys. Rev. D **54**, 3693 (1996).
G. Shiu and S. Tye, Phys. Rev. D **58**, 106007 (1998).
I. Antoniadis and C. Bachas, Phys. Lett. **B450**, 83 (1999).

[9] H. Zheng, *A Search for Large Extra Dimensions in the Jet + $\not\!\!E_T$ Final State in $\sqrt{s}$=1.8 TeV $p\overline{p}$ Collisions at DØ*, Ph.D. Thesis, University of Notre Dame, 2002 (unpublished).

[10] G. Landsberg, DØ Internal Note #3729, v4.0. `http://www-d0.fnal.gov/~gll/d0_private/ed1.htm`

[11] B. Abbott *et al.*, Phys. Rev. Lett. **86**, 1156 (2001).

[12] V.M. Abozov *et al.*, Phys. Rev. Lett. **90**, 251802 (2003).

[13] A. Gupta, N. Mondal, and S. Raychaudhuri, TIFR-HECR-99-02, hep-ph/9904234.

[14] G. Giudice, R. Rattazzi, and J. Wells, Nucl. Phys. **B544**, 3 (1999), and revised version hep-ph/9811291.

[15] T. Han, J. Lykken, and R. Zhang, Phys. Rev. D **59**, 105006 (1999), and revised version hep-ph/9811350.

[16] J. Hewett, Phys. Rev. Lett. **82**, 4765 (1999).

[17] Fermi National Accelertor Laboratory, Batavia, Illinois (USA), Tevatron Run II Handbook, Internal FNAL Note. `http://www-bd.fnal.gov/runII/index.html`

[18] A. Patwa, Ph.D. Thesis, Stony Brook University, 2002 (unpublished).

[19] Elvin Harms and Jim Morgan, "The Antiproton Source Rookie Book". `http://www-bdnew.fnal.gov/pbar/documents/PBAR_Rookie_Book.PDF`

[20] A.R.Baden "Jets and Kinematics in Hadronic Collisions", January 1997.

[21] B. Abachi *et al.* (DØ Collaboration), Phys. Rev. Lett. **74** 2632 (1995).

[22] F. Abe *et al.* (CDF Collaboration), Phys. Rev. **74** 2626 (1995).

[23] `http://www-d0.fnal.gov/Run2Physics/displays/presentations/#gallery`

[24] DØ Collaboration, "DØ Silicon Tracker Technical Design Report", DØ Internal Note #2169, 1997 (unpublished). `http://d0server1.fnal.gov/projects/silicon/www/tdr_final.ps`

[25] DØ Collaboration, "The DØ Upgrade Central Fiber Tracker: Technical Design Report", DØ Internal Note #4164, 1997 (unpublished). `http://d0server1.fnal.gov/users/stefan/www/CFT_TDR/CFT_TDR.ps` Plus discussions and notes from Gaston Gutierrez.

[26] G. Gutierrez, "Central Fiber Tracker Mechanics: Ribbon Data", Internal DØ Document, 2001. `http://d0server1.fnal.gov/projects/sciFi/mechanical/documentation.html`

[27] A. Bross *et al.*, "SCIFI 97: Conference on Scintillating Fiber Detectors", AIP Conference Proceedings 450, 1998.

[28] M. Adams *et al.*, "Design Report of the Central Preshower Detector for the DØ Upgrade", DØ Internal Note #3014.

[29] A. Gordeev *et al.*, "Technical Design Report of the Forward Preshower Detector for the DØ Upgrade", DØ Internal Note #3445, 1998 (unpublished).

[30] DØ Collaboration, S. Abachi *et al.*, Nucl. Instr. and Meth. **A338**, 185 (1994).

[31] P. Demine, *Study of the tri-lepton events in the Run II data of the DØ experiment at the Tevatron. Interpretation in the R-parity violating supersymmetry framework (λ coupling)*, Ph.D. Thesis, ISN Grenoble, 2002 (unpublished).

[32] C. Clement *et al.*, MuonID Certification for p14, DØ Internal Note #4350.

[33] The DØ Common Sample Group, `http://www-d0.fnal.gov/Run2Physics/cs/index.html`.

[34] `http:/www-d0.fnal.gov/Run2Physics/WWW/documents/temp/lum_calc1.pdf`

[35] R. Hooper, Talk given to the Muon ID Group, July 1st 2003, `http://www-d0.hef.kun.nl///displayLevel.php?fid=26`.

[36] D. Whiteson and M. Kado, DØ Internal Note #4070.

[37] K. Cheung and G. Landsberg, Phys. Rev. D **62**, 076003 (2000).

[38] CTEQ Collaboration (Coordinated Theoretical/Experimental Project on QCD Phenomenology and Tests of the Standard Model) consists of the authors of [39] and [40], and S. Kuhlmann(ANL), S. Mishra(Harvard), R. Brock, J. Pumplin, C.P. Yuan (MSU), D. Soper(Oregon),J. Collins, J. Whitmore(PSU), F. Olness (SMU), and J. Smith, G. Sterman(Stony Brook).

[39] H.L. Lai et al.(CTEQ Collaboration), Phys. Rev.**D51**, 4763 (1995).

[40] H.L. Lai et al.(CTEQ Collaboration), Phys. Rev.**D55**, 1280 (1997).

[41] ROOT: An Object-Oriented Data Analysis Framework. `http://root.cern.ch/`

[42] R. Harnberg, W.L. Van Neerven, and T. Matsura, Nucl. Phys. **B359**, 343 (1991); S. Mrenna, private communication.

[43] E. Nurse and P. Telford, "Measurement of $\sigma \times Br$ for $Z \to \mu^+\mu^-$ in $p\overline{p}$ collisions at $\sqrt{s} = 1.96$ TeV.", DØ Internal Note #4xxx.

[44] I. Bertram, G. Landsberg, J. Linneman, R. Partridge, M. Paterno, H.B. Prosper, DØ Internal Note #3476.

[45] J. Hobbs, G. Landsberg, `http://d0server1.fnal.gov/users/hooper/CL95g++.C`